EXPERIMENTAL AND THEORETICAL FATIGUE ANALYSIS OF AVIONIC UNIT MOUNTING BRACKETS INTEGRATED ON AN UNMANNED AERIAL VEHICLE UNDER RANDOM VIBRATION ENVIRONMENT

İNSANSIZ HAVA ARACINA ENTEGRE EDİLMİŞ AVİYONİK BİRİMİN MONTAJ BRAKETLERİNİN RASTSAL TİTREŞİM ORTAMINDA DENEYSEL VE TEORİK YORULMA ANALİZLERİ

ÖNER MURAT AKBABA

PROF. DR BORA YILDIRIM

Supervisor

Submitted to

Graduate School of Science and Engineering of Hacettepe University

As a Partial Fulfillment to the Requirements for the Award of the Degree of Master of Science in Mechanical Engineering.

2021

To My Dear Family

ABSTRACT

EXPERIMENTAL AND THEORETICAL FATIGUE ANALYSIS OF AVIONIC UNIT MOUNTING BRACKETS INTEGRATED ON AN UNMANNED AERIAL VEHICLE UNDER RANDOM VIBRATION ENVIRONMENT

Öner Murat AKBABA

Master of Science Degree, Department of Mechanical Engineering

Supervisor: Prof. Dr. Bora YILDIRIM

June 2021, 105 pages

In air platforms, structures encountered many types of loadings. During the design stage, all these loadings have to be considered very carefully in order to avoid catastrophic failures. One of the major concerns for engineers is the loadings that alter the structures' life and cause fatigue failure. Random vibration can be considered the main source of fatigue type of failures in air platforms.

In this thesis, the fatigue life of aluminum brackets, which are used to integrate an avionic unit to an unmanned aerial vehicle, is investigated in the frequency domain. The finite element model of the structure is constructed and the model is verified with experiments. In order to analyze the real environmental conditions, flight data is obtained by operational flight tests. Time domain signals are converted to the frequency domain and acceleration Power Spectral Density functions are obtained. Verified finite element model and collected flight data are used to obtain the stress history, which is necessary for the fatigue calculations.

Fatigue analysis of brackets is performed in three different ways. First of all, according to the frequency domain fatigue theory, a Matlab code is developed and the life of the structure is obtained. In order to test the reliability of the developed Matlab code, the same analysis is performed by using Ncode Design Life, which is a commercial fatigue analysis software. It is founded that the results of both solvers are very close to each other. Finally, accelerated life testing is performed to obtain the fatigue life in experimental conditions with accelerated flight data. In conclusion, it has been determined that the results obtained from theoretical calculations are close enough to the experimental results.

Keywords: Finite Element Model, Vibration Based Fatigue, Accelerated Life Testing

ÖZET

İNSANSIZ HAVA ARACINA ENTEGRE EDİLMİŞ AVİYONİK BİRİMİN MONTAJ BRAKETLERİNİN RASTSAL TİTREŞİM ORTAMINDA DENEYSEL VE TEORİK YORULMA ANALİZLERİ

Öner Murat AKBABA

Yüksek Lisans, Makina Mühendisliği Bölümü
Tez Danışmanı: Prof. Dr. Bora YILDIRIM
Haziran 2021, 105 sayfa

Hava platformlarında yapılar birçok yükleme türüne maruz kalırlar. Yıkıcı hasarların oluşmaması için tasarım aşamasında bu yüklemelerin çok dikkatli bir şekilde ele alınması gerekir. Bu anlamda mühendislerin en büyük endişelerinden birisi yapının ömrünü azaltan ve yorulma hasarlarına sebep olan yüklemelerdir. Rastsal titreşimler hava platformlarında yorulma kaynaklı hasarların ana kaynaklarından birisidir.

Bu tezde, aviyonik bir birimi insansız hava aracına entegre etmek için kullanılan alüminyum braketlerin yorulma ömür analizleri frekans düzleminde incelenmiştir. Yapının sonlu elemanlar modeli oluşturulmuş ve model deneylerle doğrulanmıştır. Gerçek çevresel koşulları analiz etmek için uçuş verileri operasyonel uçuş testi ile elde edilmiştir. Zaman düzlemindeki sinyaller frekans düzlemine çevrilmiş ve ivme Spektral Güç Yoğunluk fonksiyonları elde edilmiştir. Yorulma analizlerinde gerekli olan gerilme tarihçesi, doğrulanmış sonlu elemanlar modeli ve toplanan uçuş verileri kullanılarak elde edilmiştir.

Braketlerin yorulma analizleri üç farklı şekilde ele alınmıştır. İlk olarak frekans alanı yorulma teorisini kullanılarak yorulma ömrünü hesaplayan bir Matlab kodu geliştirilmiş

ve yapının ömrü elde edilmiştir. Geliştirilen Matlab kodunun güvenilirliğini test etmek için aynı analiz, ticari bir yorulma analizi yazılımı olan Ncode Design Life kullanılarak gerçekleştirilmiştir. Her iki çözücünün de sonuçlarının birbirine çok yakın çıktığı tespit edilmiştir. Son olarak, hızlandırılmış uçuş verileri kullanılarak deneysel ortamda yorulma ömrünü test etmek için hızlandırılmış ömür testi gerçekleştirilmiştir. Sonuç olarak, teorik hesaplamalar ile elde edilen sonuçların deneysel sonuçlara yeterince yakın olduğu tespit edilmiştir.

Anahtar Kelimeler: Sonlu Elemanlar Modeli, Titreşime Dayalı Yorulma, Hızlandırılmış Ömür Testi

ACKNOWLEDGEMENTS

I would like to express my gratitude to my thesis supervisor Prof. Dr. Bora Yıldırım for his guidance, support, contributions and trust in me throughout this thesis.

I also would like to express my deepest gratitude to my mentor Dr. Güvenç Canbaloğlu for his leading guidance, helpful critics and technical supports at every step of this study.

I want to thank my colleagues Ahmet Özdemir and Onur Okcu for their helpful advice and support.

I want to thank my managers and ASELSAN Inc. for giving me the opportunity to use the testing laboratories during my thesis.

I would like to express my eternal appreciation towards my dear mother, father, brother and sister, who helped me to come to these days and always put trust in me.

Finally, huge thanks to my beloved wife Esra Akbaba for her endless love, unconditional moral support and patience during the thesis.

TABLE OF CONTENTS

LIST OF FIGURES

LIST OF TABLES

LIST OF SYMBOLS & ABBREVIATIONS

List of Symbols

σ_{min}	Minimum Stress
σ_{max}	Maximum Stress
σ_r	Stress Range
σ_m	Mean Stress
σ_a	Alternating Stress
R	Stress Ratio
A	Amplitude Ratio
N	Number of Cycle According to S-N Curve
C	Material Constant
b	Basquin Exponent
S_e	Modified Endurance Limit
S_e'	Endurance Limit
$k_a, k_b, k_c, k_d, k_e, k_f$	Endurance Limit Modification Factors
K_t, K_{ts}	Stress Concentration Factors of Normal and Shear Stresses
K_f, K_{fs}	Fatigue Stress Concentration Factors of Normal and Shear Stresses
q	Notch Sensitivity
σ_{UTS}	Ultimate Tensile Strength
σ_Y	Yield Strength
σ_0	Fatigue Strength
$[ED]$	Total Accumulated Damage
$\sigma_1, \sigma_2, \sigma_3$	Maximum, Intermediate and Minimum Principal Stress
$\sigma_{xx}, \sigma_{yy}, \sigma_{zz}$	Normal Stresses in x, y and z direction
$\sigma_{xy}, \sigma_{xz}, \sigma_{yz}$	Shear Stresses
a_e	Biaxiality Ratio
ϕ_p	Principal Stress Angle
σ_{AMP}	Absolute Maximum Principal Stress
σ_{SVM}	Signed Von Mises Stress
σ_ϕ	Critical Plane Stress

$y(f_n)$	Frequency Domain Transferred Signal
$y(t_k)$	Time Domain Transferred Signal
m_n	Spectral Moments of Stress PSD
Δf	Frequency Increment
$G(f)$	Response PSD function
$E[0]$	Expected Number of Zero Crossings per Second
$E[P]$	Expected Number of Peaks per Second
γ	Irregularity Factor
x_m	Mean Frequency of PSD Response
S	Stress
$p(S)$	Probability Density Function
$n(S)$	Number of Cycle
T	Random Load Exposure Duration
$D(f_n)$	Fatigue Damage Spectrum
k	Constant of Proportionality
ζ	Damping Ratio
Γ	Gamma Function
$DP(f_n)$	Damage Potential Spectrum
m	Accelerated Life Testing Formula Exponent

List of Abbreviations

PSD	Power Spectral Density
FFT	Fast Fourier Transform
FRF	Frequency Response Function
TF	Transfer Function
RMS	Root Mean Square
FDS	Fatigue Damage Spectrum
FEA	Finite Element Analysis
CAD	Computer Aided Design
gRMS	Root Mean Square Acceleration

1. INTRODUCTION

1.1. Metal Fatigue

Metallic materials have been used to meet the need of people in many different fields from past to present. As the use of metal materials increased, the behavior of these materials in different loading conditions began to be understood. Since the response of metallic materials under static and dynamic conditions are different, it is very important to handle the engineering problem correctly. If the dynamic loading has a repetitive characteristic, the problem must be handled in a unique way, which is described as fatigue of materials.

The reactions of metals to cyclic loads have been a very important area of research since the last century. With the developing technology, the field of metal fatigue maintains its importance in aviation, space, automotive and many other fields.

Fatigue type of failures are very dangerous because even stresses well below the yield strength can cause fatigue failure without any warning. 90 percent of metal failures are thought to be caused by fatigue. That is why it is unique and must be analyzed very carefully.

1.2. History of Fatigue Research

From the beginning of the 1800s, studies have been carried out to understand the reason for the failure of metals under repetitive loading even the failure is not expected.

First known fatigue study was published in 1837 by German engineer Wilhelm Albert. He constructed a test machine for the conveyor chains which had failed in service [1].

In 1839, French engineer and mathematician Jean-Victor Poncelet mentioned in the Metz Military School that the metals are being tired [2].

Scottish mechanical engineer William John Macquorn Rankine discussed the fatigue strength of railway axles in 1842 [3].

In 1854, the first term “fatigue” is pronounced by Englishman Braitwaite [4].

Beginning in 1860, German engineer Wöhler published researches about fatigue tests of railway axles. In a final report he published in 1870, he stated that “Material can be induced to fail by many repetitions of stresses, all of which are lower than the static strength ” [5]. The well-known S-N curve has also referred to as Wöhler’s S-N curve since 1936.

Goodman published his study which is about the effect of the interaction of mean and alternating stresses on fatigue life of materials in 1899 [6].

Ewing and Humfrey observed slip bands on the surface of materials under rotating and bending loading in 1903. This was probably the first definition of fatigue in a metallurgical sense [7].

In 1910, Basquin constructed an S-N curve with a simple formula, $\sigma_k = CR^n$, in the form of a log-log axis by using Wöhler’s test data. He obtained numerical values of formulas constants C and n [8].

Due to the development of technology and the increase in the use and importance of aircraft in wars and civil applications, fatigue research has gained momentum. The first full-scale fatigue test for large aircraft parts was carried out by Royal Aircraft Establishment in the UK in 1918 [9].

The first fatigue book was written by Englishman Gough in 1924 [10].

In 1924, Swedish scientist Palmgren published his article on damage accumulation hypotheses for fatigue life [11]. Later in 1945, American Miner worked on Palmgren’s work to obtain today’s famous Palmgren-Miner cumulative damage accumulation equation, $\sum_{N_i}^{n_i} = 1.0$ [12].

In 1954, L. F. Coffin and S. S. Manson conducted research on the effect of plastic strains on the fatigue life of the component. Research leads the development of a concept called "low cycle fatigue" with the well-accepted formula, $\frac{\Delta\varepsilon}{2} = \varepsilon_f'(2N)^c$ [13, 14].

In 1958, Irwin of the US Navy defined the stress intensity factor with the formula $K = S\sqrt{\pi.a}$, which describes that the stress state at the crack tip is related to the rate of crack growth [15].

At Lehigh University, Paris proposed his PhD thesis about the growth of cracks due to variations in load in 1962, which is described by the equation known as Paris-Erdogan Law, $\frac{da}{dn} = C.\Delta K^n$ [16].

First edition of MIL-STD-810, whose current edition is widely used today, published in 1962. This standard describes what kind of conditions a material will be subjected to during its lifetime and how these conditions will be simulated in a laboratory environment.

Japanese scientists M. Matsuishi and T. Endo developed the rainflow cycle counting algorithm in 1968. Rainflow cycle counting makes it possible to use Miner's cumulative damage theory for complex random loadings by converting complex random loadings into simple stress reversals [17].

In 1971, German scientist Elber explains the mechanisms and importance of crack closure on fatigue crack growth [18].

M. W. Brown and K. J. Miller published their work in 1973 and in their work they stated that the fatigue failure in the case of the multiaxial type of loading depends on the critical plane, where the most damage occurred so that the loads on the critical plane must be considered [19].

1.3. Significant Fatigue Crashes

In the early 1800s, many railroad accidents occurred and research mainly focused on this area to understand the reason behind the accidents. One of the most catastrophic accident happened in Versailles in 1842 due to a broken axle of the locomotive. At least 55 passengers died due to accident [20].

Figure 1.1 Versailles rail accident

The first commercial aircraft Comet, developed by de Havilland in the United Kingdom, suffered two major crashes in 1954, a few years after their first flight in 1949. After the crashes, the Cohen committee established to examine the causes of the crashes. It is founded that the pressure changes in the fuselage cause fatigue at the window cutout, which has sharp corners and create stress concentration. After the Comet crashes, applying much more complex tests of complete aircraft structures, so-called full-scale fatigue tests became vital. It was painfully understood that the design of the sharp-edged window design was flawed.

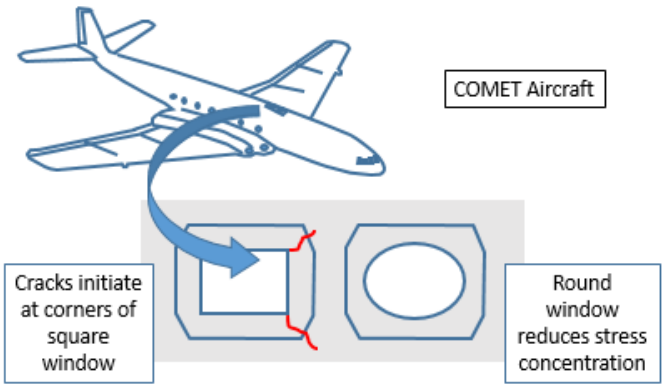

Figure 1.2 Fatigue failure due to sharp corners of the window cutout [21]

Norwegian semi-submarine drilling rig Alexander L. Kielland had a catastrophic crash in 1981. Due to fatigue crack, five of the six carrier columns collapsed and 123 people died on the platform.

In 1988, a Boeing 737 type aircraft belonging to Aloha Airlines had a serious accident where a piece of the fuselage blown off during flight but managed to land safely. After the investigations, it is concluded that the accident was caused by metal fatigue and corrosion was the major cause of the crack.

In the year 1998, one of the biggest train accidents in history occurred and 101 people died due to the accident. A high-speed train in Eschede-Germany derailed and crashed into a road bridge. After the crash investigations, it is stated that as a result of a fatigue-induced crack in one of the wheels of the train, the wheel was broken and consequently train derailed.

A Boeing 747 type aircraft belonging to China Airlines suffered a terrible accident in 2002 and 225 passengers died. Investigations after the crash show that the accident was caused by a fatigue crack due to insufficient maintenance as a result of the previous tail strike accident.

Alexander L. Kielland

Aloha Airlines Accident

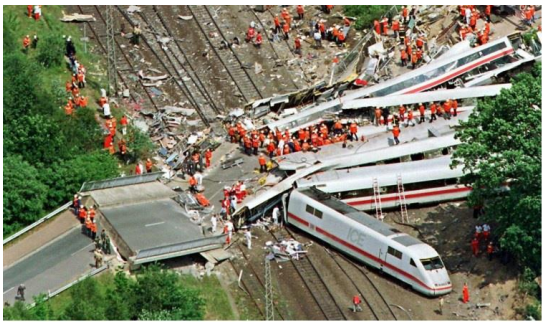

Eschede Train Disaster

China Aircraft Disaster

Figure 1.3 Significant fatigue disasters in recent past

1.4. Thesis Outline

This thesis contains nine chapters. In the first chapter, general information about metal fatigue is given. Afterwards, the history of fatigue research and very important studies from the very past to present is mentioned. In addition, significant examples of fatigue disasters are given in this chapter.

In the next chapter, the literature survey is given based on the vibration fatigue phenomenon. It starts with important scientists' studies about vibration fatigue that forms the cornerstones of this thesis. In addition, similar studies to this thesis that are used as the main source of information in the preparation of this study are given in this chapter.

In the third chapter, more detailed information about fatigue theory is given. Mechanism of fatigue and fatigue life prediction methods are explained. Since this study is based on the stress-life method, it is discussed in more detail. However, strain life and crack propagation methods are mentioned briefly. The vibration-based fatigue method, which forms the main foundation of this study is explained in detail. The classical rainflow cycle counting method is mentioned in time domain analysis and the probability density functions of rainflow ranges obtaining methodologies are explained in the frequency domain approach. Finally, accelerated life testing and vibration PSD synthesis concepts are explained.

The fourth chapter is dedicated to the finite element model construction of the structure. Contact modelling and meshing strategy are explained in detail. Element quality and the number of elements and nodes for different meshing methods are discussed. Singularity point handling procedures and mesh convergence analysis are also given in this chapter. Finally, the most critical nodes of the structure are identified.

In the fifth chapter, tests and analyses performed to verify the finite element model are explained. First of all, experiments are carried out to measure the natural frequencies and the frequency responses of the structure. Afterwards, natural frequencies are found from Ansys Modal Analysis and the frequency responses are obtained from Ansys Harmonic Analysis and Ansys Random Vibration Analysis. Consequently, experimental results are compared with FEA results and the model is verified.

In the sixth chapter, it is explained how the flight test data are collected and synthesized in order to obtain real environment conditions that will constitute loading input for fatigue analysis. The data obtained from each maneuver of air platform during flight test is combined and a single input PSD loading, which expresses the loading that the air vehicle will be subjected to its whole life is obtained. Lastly, in order to perform a fatigue test with reasonable durations, obtained input PSD is accelerated to shorter durations so that the damage potential of the loading remained the same.

In the seventh chapter, by using the verified finite element model and the obtained flight data, the fatigue life of the mounting brackets is found from the commercial software Ncode and the developed Matlab code by using different PSD cycle counting methods. Results are compared and numerical code is verified with commercial software. After that, flight data is scaled and accelerated in order to have reasonable failure durations and accelerated life testing is performed. Failure durations are compared with the results obtained from verified numerical code.

In chapter eight, case studies have been performed to understand the effect of different design parameters on fatigue life. In the first case study, the decision of coefficient m, the accelerated life testing formula exponent and the dependencies of this coefficient are investigated. In case two, the effect of the shaker's PSD data application range during accelerated life testing on the fatigue life is analyzed. In the third case study, according to applied flight data, the damage contribution of different frequency intervals is examined. Lastly, the difference in life between two points that are 0.42 mm close to each other is investigated in the fourth case study.

Finally, in the last chapter, studies conducted in this thesis are briefly summarized and the obtained results are evaluated.

2. LITERATURE SURVEY

One of the major fatigue damage estimation from the Power Spectral Density function is proposed by S.O. Rice in 1954 [22]. Rice found the relationship between spectral moments with the number of peaks and the number of upward zero crossings of the random stress history of the frequency content.

Bendat in 1964 [23], proposed the Probability Density Function of rainflow ranges in the frequency domain for narrowband signals by using the first four spectral moments of the stress PSD function. The drawback of Bendat's PDF estimates is that when the signal has wideband characteristics, this method gives very conservative results.

After Bendat's PDF estimation method, some other methods have been developed. Tunna [24], Wirsching [25] and Chaudhury & Dover [26] are proposed methods to correct Bendat's narrowband conservatism. Also, Steinberg proposed a simplified fatigue estimation method for electronic components based on the three-band technique [27].

One of the best rainflow cycle counting method in the frequency domain proposed by Dirlik in his PhD thesis [28]. In this study, Dirlik used digital simulations and the Monte Carlo approach and he presents empirical solutions to define the Probability Density Function of rainflow ranges for any Power Spectral Density function. Dirlik's method gives accurate results both in wideband and narrowband signals and widely used in many fatigue researches.

Bishop et al [29] handled the calculations of fatigue with finite elements in a very broad perspective in his work. Sub-elements of fatigue, which are stress-life, strain life, crack propagation, multiaxial fatigue, vibration fatigue in the time and frequency domain examined comprehensively. In this study, Bishop explained in detail how fatigue analysis should be done in the finite element environment. Bishop states that in order to examine the dynamic behavior of the system correctly, frequency domain approaches are much more suitable since in the time domain approach, transient fatigue analyses are very time-consuming. In this study, it is mentioned that the difference in the stress history by factor 2 may change the expected life with factor 1000. That is why obtaining true stress history

is essential. In addition, it is stated that the life of a test specimen may change 2-3 factor even an identical test specimen is tested in the same condition and environment.

Bishop and Woodward [30] investigated the fatigue analysis of missile shaker table mounting bracket in the frequency domain approach. At the first fatigue tests, it is observed that the calculated fatigue life is much greater than the tests. Eventually, it is concluded that due to tolerance mismatch between two bodies, a possible mean stress field is introduced and it misleads the calculated results with real tests.

Aykan [31] studied fatigue analysis of a chaff dispenser bracket of a helicopter on frequency domain. The finite element model is built and it is verified with experiments. An operational flight test is performed to obtain the real environments loadings and multi-input loadings are applied to commercial software to get the fatigue life. Lastly, fatigue test of the bracket is performed with electrodynamic shaker in three-axis separately and the sum of the total life found on experiments are compared with the results found from commercial fatigue software. It is concluded that since the cross-correlations of input PSDs could not be considered in uniaxial separate fatigue tests, the life of the structure in test conditions observed to be less than the calculated three-axis simultaneous fatigue life. Also in this study, it is stated that approximately 7 percent of stress increase may result in a 50 percent of life decrease.

Eldogan [32] developed a numerical code that is capable of analyzing the fatigue life of structures both in the time domain and frequency domain. Real flight data is obtained from the platform and both analysis types are carried on according to flight data. In time domain analysis, stress history is obtained with strain gauges at the critical location of the structure. On the other hand, in the frequency domain analysis, stress PSDs are obtained in finite element model of structure hereby before obtaining stress PSDs, FEM model is verified with experiments. Found life on commercial software and developed code are compared and verified with experimental fatigue tests. When comparing the time domain and frequency domain results, Dirlik's approach gives the closest results with the rainflow cycle counted time domain analysis.

Demirel [33] studied fatigue analysis of a notched cantilever beam manufactured from steel and aluminum. The finite element model of the beam is verified with experimental

modal analysis. The fatigue life of the beams is found from commercial software and results are compared with the life obtained from accelerated life testing.

Teixeira et al [34] investigated the fatigue life of a go-kart frame in time and frequency domains with multi-axial loading conditions. It is founded that time domain and frequency domain results did not differ from each other more than 15 percent for any of the simulated cases. However, one of the important outcomes of this study is that the time domain transient analysis is 881 times slower than the frequency domain harmonic analysis. In addition, in this study, the Critical Plane approach is founded to be the best in multiaxial loading conditions but it is 100 times slower than used Von Mises PSD method.

Halfpenny et al [35] investigated the fatigue life of different case studies which are obtained from different cycle counting methods from PSD of stresses and classic time domain rainflow cycle counting. Also, the effect of S-N curves with different slopes are examined. For the time domain analysis, the duration of the time signal found to be very important. Using a single slope S-N curve with at least 1 million data is required in order to have statistically consistent results. According to this study, the Steinberg method is only suitable for single slope S-N curves since it only contains the three multiples of RMS stress. For shallow S-N curves when the slope is greater than 18, PSD cycle counting methods became conservative compared to time domain analysis. Below that limit, even for different S-N curve slopes, Dirlik and Lalanne methods are very effective and give almost the same damages as it is obtained from classic time domain cycle counting methods. According to Halfpenny, since it is not practical to have the required duration of the time signal, PSD based cycle counting methods are much more effective.

3. THEORY OF FATIGUE

3.1. Fatigue Mechanism

Failure of metals in cyclic loading conditions has always been a big problem for engineering design history. Even the loading is under yield strength, failure may occur without any warning. Fatigue failure resembles brittle failure since the fracture surface is perpendicular to the stress axis and no necking occurs. However, failure mechanisms are quite different from static brittle fracture. After many studies mainly in experiments, it is found that fatigue type of failure occurs in the presence of a certain fatigue mechanism. This mechanism can be described as the initiation of crack, propagation of crack and failure of the material.

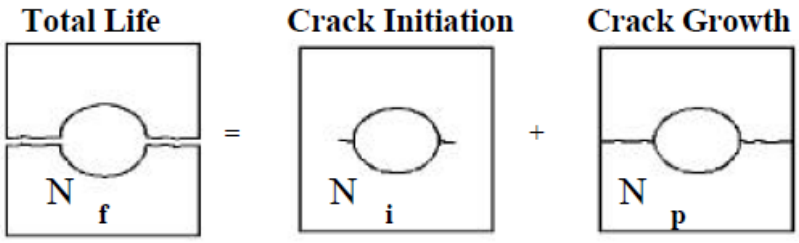

Figure 3.1 The ideal total life of a fatigue design [29]

In the crack initiation phase, one or more micro cracks initiation occurs due to cyclic loading. This phase is not visible to the naked eye. Once the crack initiates, in each cycle, it propagates and micro cracks are becoming macro cracks. After a certain number of cycles, due to macro crack propagation, the area of material shrinks and the remaining material cannot support the load and eventually sudden fracture without any warning occurs.

From Figure 3.1, it can be seen that the total life of the material is the sum of the crack initiation phase and crack growth of the propagation phase. The duration of crack initiation and crack growth phases varies according to geometry, loading and material type. For example, the crack growth phase takes longer time for ductile materials while this phase lasts very short for brittle materials.

Figure 3.2 A typical fatigue failure surface [36]

3.2. Fatigue Life Prediction Methods

Fatigue life prediction methods attempt to estimate the number of cycles of the material when the material fails under a given loading. These methods are divided into three approaches; stress-life method, strain-life method and crack propagation method.

In this study, vibration fatigue theory is used. Since this theory is based on the stress-life method and in the case study, stress levels are under the yield strength and there is no plastic deformation, the stress-life method will be covered in details whereas strain-life and crack propagation methods will be discussed briefly.

3.2.1. Stress Life Method

In the stress-life approach, the material is assumed to be fully elastic even in localized regions and stress levels are well below the yield strength and generally, the number of cycles required to failure is greater than 10^4-10^5 cycles. Therefore, the stress-life approach is considered in case of high cycle fatigue.

In Figure 3.3, typical fluctuating stress cycles for a stress life method are given. In part-a, a completely reversed sinusoidal form stress cycle can be seen, which can be used to simulate the loading environment of a rotating shaft operating at a constant speed without overloads. In such case, maximum and minimum stress magnitudes are equal but they have opposite signs. In part-b, an example for repeated stress with a positive mean is illustrated. For this type of loading, maximum and minimum stress magnitudes are not equal anymore. In the given example, both maximum and minimum stress levels are

tension but they may be both compression or tension/compression. In part-c, a much-complicated stress cycle is illustrated where mostly in the operating environments many mechanical parts encountered.

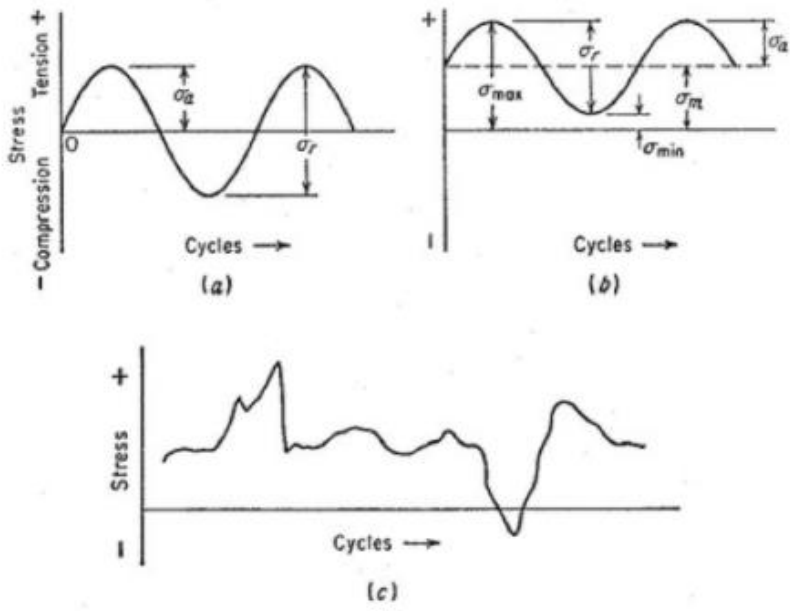

Figure 3.3 Typical fatigue stress cycles. (a) reversed stress with zero mean, (b) repeated stress with positive mean and (c) irregular or random [37]

For fluctuating stress cycles, it has been found that in periodic patterns exhibiting a single maximum and single minimum of loading, the shape of the wave is not important, but the peaks on both sides are important [38]. So, in Figure 3.3, some useful parameters are defined to characterize the stress cycles,

- Minimum Stress : σ_{min}
- Maximum Stress : σ_{max}
- Range of Stress : $\sigma_r = \sigma_{max} - \sigma_{min}$
- Mean Stress : $\sigma_m = \frac{\sigma_{max}+\sigma_{min}}{2}$
- Alternating Stress : $\sigma_a = \frac{\sigma_{max}-\sigma_{min}}{2}$
- Stress Ratio : $R = \frac{\sigma_{min}}{\sigma_{max}}$
- Amplitude Ratio : $A = \frac{\sigma_a}{\sigma_m} = \frac{1-R}{1+R}$

3.2.1.1. S-N Curve

The life behavior of metals under cyclic loading data is presented in S-N curves. S indicates the cyclic stress amplitude and N is the number of cycles to failure. It is important to remark that in some resources cyclic stress amplitude can be expressed with stress range or alternating stress. In S-N testing, the specimen is carefully machined and polished and these diagrams generally obtained for the completely reversed cycle ($\sigma_m = 0$), where stress levels alternate equal magnitudes of tension/compression. N is plotted on the x-axis in logarithmic scale, S is plotted in y-axis logarithmic or linear scale, and the relation between cyclic stress and life can be described as follows,

$$N = C \cdot S^{-b} \tag{3.1}$$

Where b is the inverse of the slope, which also called the Basquin exponent, and C is related intercept on the y-axis.

In the case of ferrous metals such as steel, the graph becomes horizontal after a certain number of cycles (N < 10^6 cycles) and it is defined as fatigue limit or endurance limit. Infinite life can be obtained for cyclic stress levels below the endurance limit. However, for non-ferrous metals like aluminum, such a limit does not exist and slope gradually downwards with an increasing number of cycles. So that, for non-ferrous metals at around 10^8 cycles, it is accepted as fatigue strength of material and tests are terminated after that number of cycles.

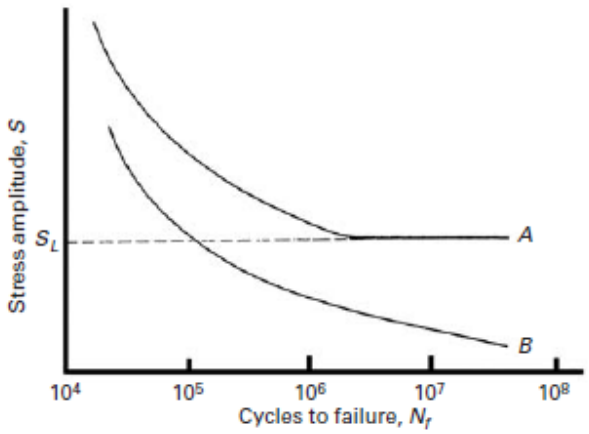

Figure 3.4 S-N curves of ferrous (A) and non-ferrous (B) metals [39]

3.2.1.2. Endurance Limit Modifying Factors

To determine the endurance limit of material under a certain type of loading, the specimen is produced as perfect as possible and tested very carefully in that particular testing environment. However, since the environmental conditions are not similar to laboratory conditions and not every material can be produced perfectly, the endurance limit of material should be considered according to endurance limit modifying factors when endurance tests of parts are not available for desired testing and material conditions.

$$S_e = k_a . k_b . k_c . k_d . k_e . k_f . S'_e \tag{3.2}$$

Where,

k_a = surface modification factor

k_b = size modification factor

k_c = load modification factor

k_d = temperature modification factor

k_e = reliability factor

k_f = miscellaneous- effects modification factor

S'_e = test specimen endurance limit

S_e = endurance limit at the critical location of a machine part in the geometry and condition to use

3.2.1.3. Stress Concentration and Notch Sensitivity

As it is stated before, during determining S-N properties, the specimen is produced as perfect as possible without any irregularities or discontinuities such as holes, notches, grooves etc. However, most of the time components in real life can have holes, notches or grooves. The existence of such irregularities in the material increases theoretical stresses significantly. Such a situation is handled with stress concentration factors K_t for normal stresses and K_{ts} for shear stresses.

When the consideration is the fatigue of material, experiments have shown that the effect of notches is less than estimated from the stress concentration factor K_t. Accordingly, another factor is defined as fatigue stress concentration factor K_f. So the maximum stress in fatigue can be calculated by using K_f as follow [38],

$$\sigma_{max} = K_f . \sigma_0 \qquad \text{or} \qquad \tau_{max} = K_{fs} . \tau_0 \tag{3.3}$$

Fatigue stress concentration factor K_f is just a reduced value of K_t and it is a function of stress concentration factor K_t and notch sensitivity q.

$$K_f = 1 + q(K_t - 1) \qquad \text{or} \qquad K_{fs} = 1 + q(K_{ts} - 1) \tag{3.4}$$

For a design, first K_t is found from the geometry of component and then material dependent q is defined and eventually K_f can be obtained.

3.2.1.4. Effect of Mean Stress

Most of the time, S-N data is obtained for completely reversed cycles where the mean stress is zero. However, in real applications, most loadings create non-zero profiles like in Figure 3.3 (b). If the mean stress getting more tensile, allowable alternating stress that the material can withstand gets smaller. To account for the mean stress effect in fatigue analysis, various empirical expressions that tried to fit the experimental failure data have been proposed. In some methods such as Goodman or Soderberg, reduction in alternating stress due to mean stress assumed to be linear but it is parabolic for Gerber's approach.

- Goodman's relationship: $\sigma_a = \sigma_0[1 - \sigma_m/\sigma_{UTS}]$ (3.5)
- Soderberg's relationship: $\sigma_a = \sigma_0[1 - \sigma_m/\sigma_Y]$ (3.6)
- Gerber's relationship: $\sigma_a = \sigma_0\left[1 - (\sigma_m/\sigma_{UTS})^2\right]$ (3.7)

In the equations, σ_m is the mean stress, σ_a is the alternating stress, σ_0 is the fatigue strength in terms of stress amplitude, σ_Y is yield strength and σ_{UTS} is the ultimate tensile strength of the material.

In Figure 3.5, the relationship of mean stress and alternating stress with Goodman's, Soderberg's and Gerber's approaches are shown. Values to the right side of the line assumed to be failed. The most conservative method among these relations is Soderberg's approach. According to experiments it has been observed that most materials fall between Gerber's and Goodman's lines [39]. Thus, Goodman's linear relationship is mostly used in literature.

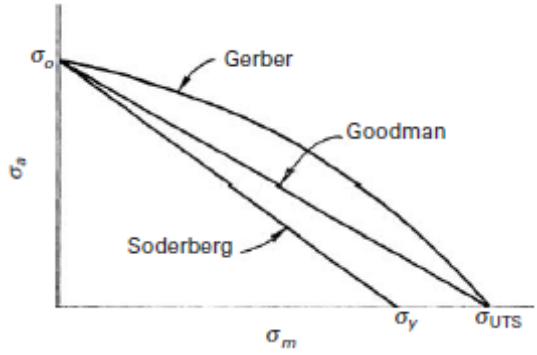

Figure 3.5 Effect of mean stress on fatigue according to Gerber, Goodman and Soderberg approaches [39]

3.2.1.5. Variable Amplitude Loading and Damage Accumulation

Up to this point, constant amplitude and constant frequency stress cycles with zero mean stress and non-zero mean stress cases are considered. However, in service conditions, many components encountered with varying amplitude and frequencies stress cycles. A simple representation of variable amplitude loading is shown in Figure 3.6.

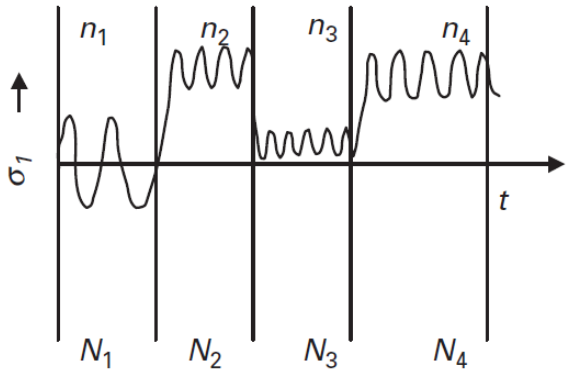

Figure 3.6 The sequence of block loadings at four different mean stress and amplitudes [39]

In such a loading case, Palmgren and Miner [12] suggested a simple approximation where each individual loading has a contribution to the total damage of the structure. Considering at the first block of loading, stress level σ_1 is repeated n_1 times and according to the S-N curve of material, σ_1 level of stress can be repeated N_1 times until failure.

Assume that this approach is applied for each block until the end of the loading time. So the total damage can be obtained by linearly summing up all.

$$[ED] = \sum_{i=1}^{k} \frac{n_i}{N_i} \tag{3.8}$$

Where $[ED]$ is the total accumulated damage due to variable amplitude blocks and when the $[ED] = 1$, the entire life is consumed and failure occurs. As it is clear from equation (3.8), Miner's theorem assumes that the order of cycling is not important.

3.2.1.6. Complex Loadings and Cycle Counting Techniques

In real-life engineering problems, variable amplitude loadings may be much more complex than the loading given in Figure 3.6. For complex loading history, without using some techniques it is not easy to apply Miner's theorem. So, in order to decompose the random data and extract the mean-range information of stress cycles, cycle counting methods are introduced. Some examples of cycle counting methods are rainflow cycle counting, level crossing counting, range counting and peak counting.

One of the most preferred and reasonable method rainflow cycle counting developed by Matsuishi and Endo in 1968 [17]. Rainflow Cycle Counting algorithm is summarized as follows:

- Load history is rotated 90° so that the time axis is vertically downward and load history resembles a pagoda roof.
- Considering peaks of the roof are on the right side and valleys are on the left side.
- If the fall starts from a peak [40]:
    a) The drop will stop if it meets an opposing peak larger than that of departure,
    b) It will also stop if it meets the path traversed by another drop, previously determined,
    c) The drop can fall on another roof and continue to slip according to rules a and b.

- If the fall begins from a valley: [40]
    d) The fall will stop if the drop meets the valley deeper than that of departure,
    e) The fall will stop if it crosses the path of a drop coming from the preceding valley,
    f) The drop can fall on another roof and continue according to rules d and e.

To explain the algorithm given above, an example is given in Figure 3.7.

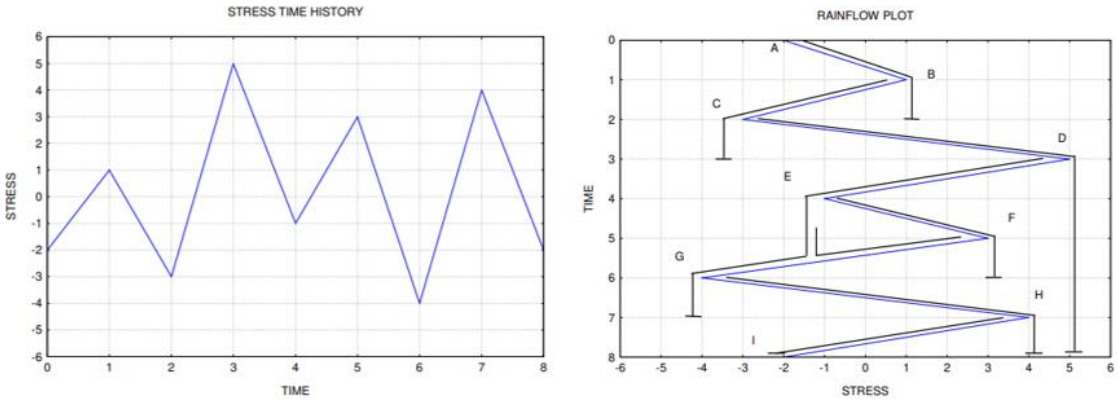

Figure 3.7 Rainflow cycle counting [41]

Table 3.1 The output of a rainflow cycle counted data [41]

Path	Cycles	Stress Range	Peak	Valley	Mean
A-B	0.5	3	1	-2	-0.5
B-C	0.5	4	1	-3	-1
C-D	0.5	8	5	-3	1
D-G	0.5	9	5	-4	0.5
E-F	1.0	4	3	-1	1
G-H	0.5	8	4	-4	0
H-I	0.5	6	4	-2	1

The output of a rainflow cycle counted stress-time data usually expressed as a range-mean histogram. After obtaining stress range, mean and cycle information of random loading by using rainflow cycle counting procedures, it is easy to implement Miner's damage theorem. An example for a range-mean histogram obtained from random stress-time data by using rainflow cycle counting method is given in Figure 3.8.

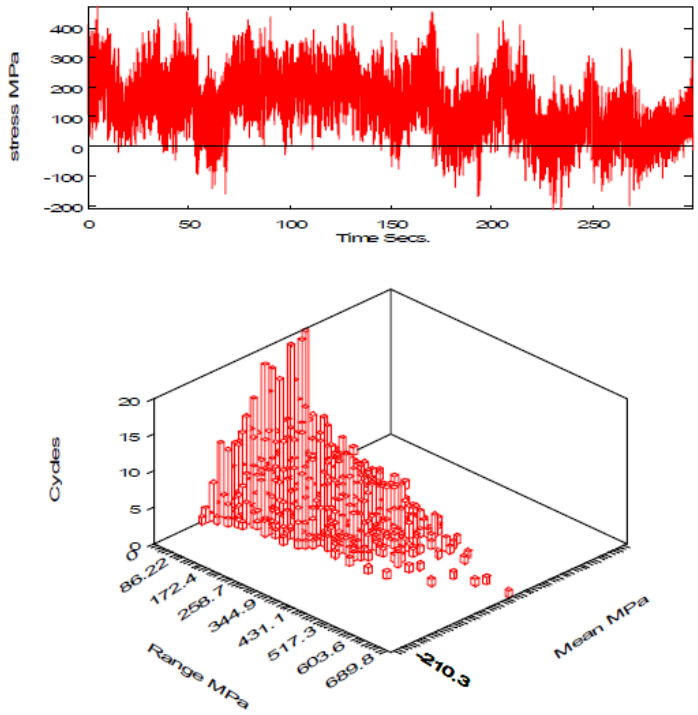

Figure 3.8 Range-Mean Histogram of rainflow cycle counted data [42]

3.2.1.7. Proportional and Non-Proportional Loadings and Stress Combination Methods

It is important to remark that the Stress Life method concentrates on single equivalent stress at the location of interest on the structure. However, that equivalent stress is actually a combination of stresses at that particular location. So that the true combination method has to be chosen to reduce the multiaxial stress state into an equivalent value in order to obtain reliable results.

For a time-varying load, three-dimensional stress tensor with nine components can be used to express the stress state of any point on the structure. Moreover, 3D stress tensor can be reduced to three principal stresses and their directions.

$$\begin{bmatrix} \sigma_{xx} & \sigma_{xy} & \sigma_{xz} \\ \sigma_{xy} & \sigma_{yy} & \sigma_{yz} \\ \sigma_{xz} & \sigma_{yz} & \sigma_{zz} \end{bmatrix} \Rightarrow \begin{bmatrix} \sigma_1 & 0 & 0 \\ 0 & \sigma_2 & 0 \\ 0 & 0 & \sigma_3 \end{bmatrix} \tag{3.9}$$

Most of the time, fatigue crack initiates at the free surfaces where the shear stresses and normal stress are always zero or the sheet is thin enough so the principal stress normal to the surface is designated with $\sigma_3 = 0$. The other two principal stresses are ordered in magnitude so that σ_1 is the maximum principal stress and σ_2 is the other in-plane principal stress.

The true combination method is mainly dependent on the loading of the data. If there are at least more than two inputs that excite the system, proportionality needs to be checked to decide the combination method.

Proportionality of loading can be described with the biaxiality ratio a_e, and the principal stresses angle ϕ_p as follows,

- Biaxiality ratio: $a_e = \frac{\sigma_2}{\sigma_1}$
- Maximum principal stress angle with local x-axis: ϕ_p

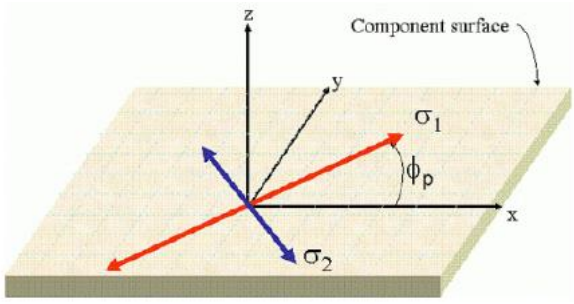

Figure 3.9 In-plane principal stresses [43]

When the biaxiality ratio and/or principal stress angle is fixed with varying loading, it is classified as proportional multiaxial loading. On the other hand, for non-proportional multiaxial loadings, the biaxiality ratio or the direction of principal stresses changes with varying loadings. In the figures Figure 3.10 and Figure 3.11 below, examples of proportional and non-proportional multiaxial cases are shown.

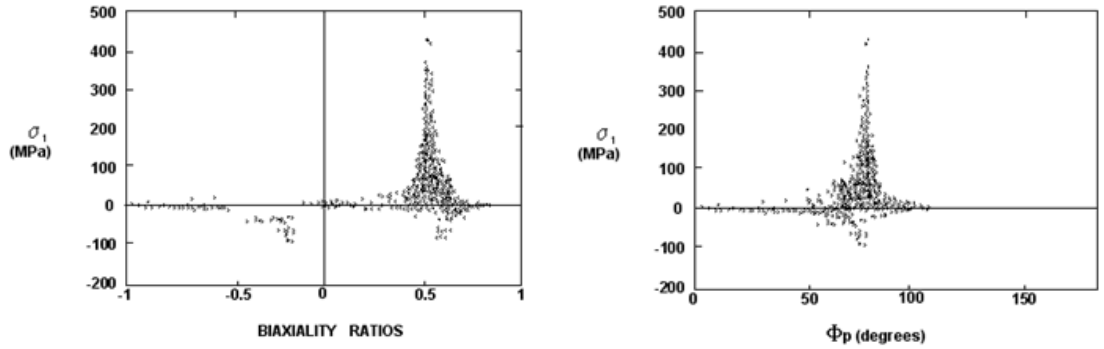

Figure 3.10 Principal Stress vs biaxiality ratio and principal stress angle for multiaxial proportional loadings [44]

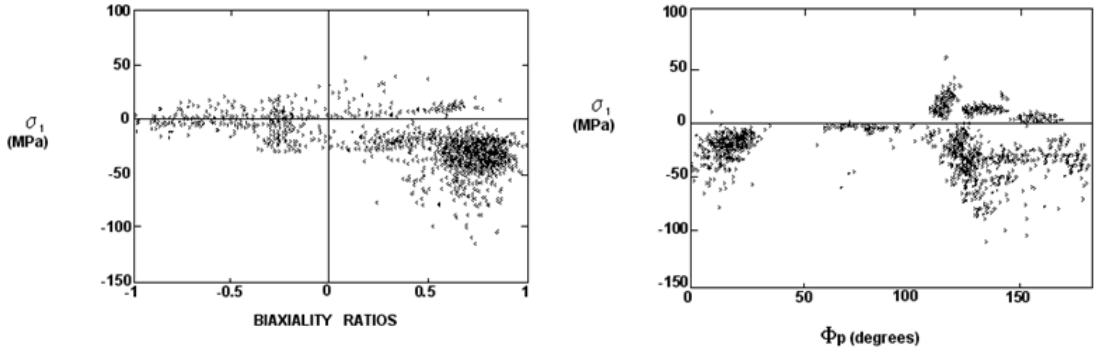

Figure 3.11 Principal Stress vs biaxiality ratio and principal stress angle for multiaxial non-proportional loadings [44]

In Table 3.2, the determination methodology of the combination method according to stress state proportionality by using principle stress angle and biaxiality ratio is summarized.

Table 3.2 Combination methods according to the proportionality [29]

Stress State	**Principle Stress Angle, ϕ_p**	**Biaxiality Ratio, a_e**	**Combination Method**
Uniaxial	Constant	$a_e = 0$	Uniaxial Theories
Proportional Multiaxial	Constant	$-1 < a_e < 1$ = Constant	Equivalent Stress-Strain Theories
Non-proportional Multiaxial	May vary	a_e , May vary	Critical Plane etc.

After the proportionality is defined for the multiaxial loading case, a proper stress combination method has to be chosen. If the loading is found to be proportional, equivalent stress-strain theories are suitable. However, these theories are not suitable for non-proportional loadings, since these theories only sum the damage regardless of whether the principals stress directions changing or not.

For non-proportional loadings, the critical plane method calculates the fatigue damage for all possible planes and the most damage potential case, which is the critical plane, is chosen. Details of this topic will not be covered in this study.

In Figure 3.12, it can be seen different equivalent stress theories for a cylindrical notched specimen with uniaxial sine loading. From the figure, the best approaches are the Absolute Maximum Principal Stress Theory and Signed von Mises Theory since the others are under estimate the stress state.

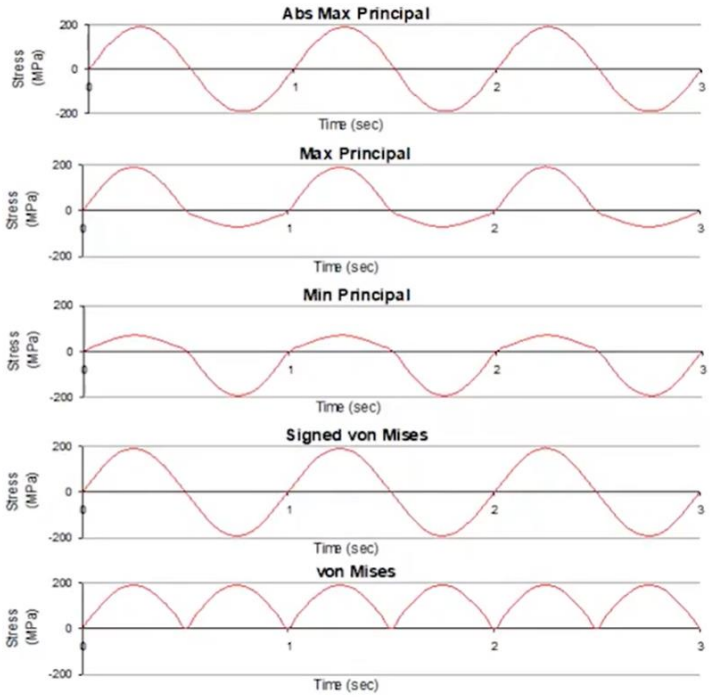

Figure 3.12 Equivalent stress theories for a cylindrical notched specimen with uniaxial sine loading [45]

- **Absolute Maximum Principal Stress Theory:**

It is defined as the principal stress with the largest magnitude and its sign.

$$\sigma_{AMP} = sign * \sigma_{AMP} \tag{3.10}$$

Where,

$$\sigma_{AMP} = \max(|\sigma_1|, |\sigma_2|, |\sigma_3|) \tag{3.11}$$

- **Signed Von Mises Criterion:**

It is the Von Mises stress but forced to take the sign of absolute maximum principal stress.

$$\sigma_{SVM} = \frac{\sigma_{AMP}}{|\sigma_{AMP}|} \cdot \sqrt{\frac{(\sigma_1 - \sigma_2)^2 + (\sigma_2 - \sigma_3)^2 + (\sigma_3 - \sigma_1)^2}{2}} \tag{3.12}$$

3.2.2. Strain Life Method

If the material subjected to stresses higher than the yield strength, a significant amount of plastic strains occurs in the structure. Since the load is high in the strain-life approach, consequently life is shortened. In such a case, failure happens less than 10^3 cycles, which can be considered in the low cycle fatigue category.

3.2.3. Crack Propagation Method

In the crack propagation method, ideas of fracture mechanics are applied. In such a case, crack is detected and crack size and shape are pre-known. Estimation of life of structure from the initial crack size becomes the critical size and eventually until failure is the main concern of this method.

3.3. Random Vibration Fatigue

In air platforms, structures encountered many types of loadings. During the design stage, all the loadings have to be considered very carefully in order to avoid catastrophic failures. One of the major concerns for engineers is the vibration-based loadings that alter the structures life and cause fatigue failure.

Mainly, vibration loadings classified into two categories: deterministic and random. If the value of the magnitude of excitation is known at a given time, this excitation is called deterministic. On the other hand, when the excitation cannot be predicted, it is called random or non-deterministic.

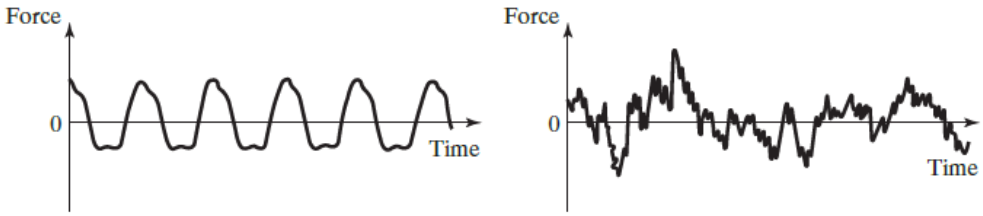

Figure 3.13 Deterministic and random excitation [46]

Most of the events in nature are non-deterministic. There can be given many examples for random events such as stresses on the axle of a car, pressure in a pipeline, load induced on an airplane wing or an earthquake motion. Even taking a second sample with the same process, the results would be different (Figure 3.14). Therefore, random vibrations can only be determined with statistical methods. As long as the data is long enough, some statistical parameters are quite similar for each sample such as the mean value of data points, number of peaks or number of zero crossings.

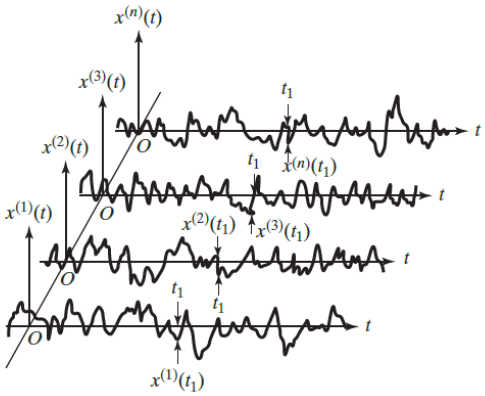

Figure 3.14 Example for a random data samples on same location [46]

In a random vibration analysis, since the input excitations are statistical in nature, output responses such as displacement or stress etc. are also determined statistical. These output parameters assumed to have a Gaussian distribution as shown in Figure 3.15 and the occurrence probability with respect to 1σ, 2σ and 3σ standard deviations of Gaussian Distribution are given in Table 3.3.

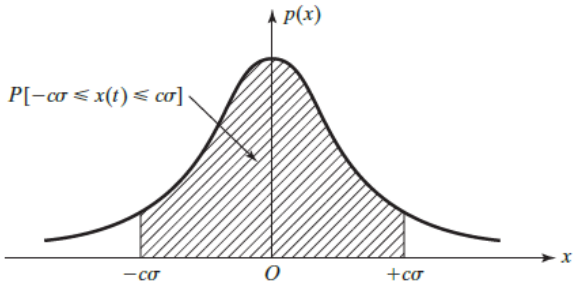

Figure 3.15 Gaussian Distribution [46]

Table 3.3 Occurrence probability according to Gaussian Distribution and zero mean

Standard Deviation	$\pm 1\sigma$	$\pm 2\sigma$	$\pm 3\sigma$
Probability	0.6827	0.9545	0.9973

When a structure encountered a random type of loading and the concern is fatigue failure, the problem can be handled either in the time domain or in the frequency domain. Before explaining the difference of each fatigue approach, a brief explanation of the time and frequency domain will be given.

Time based and frequency based signals can be converted to each other by using Fourier Transformation and Inverse Fourier Transformation as it is illustrated in Figure 3.16.

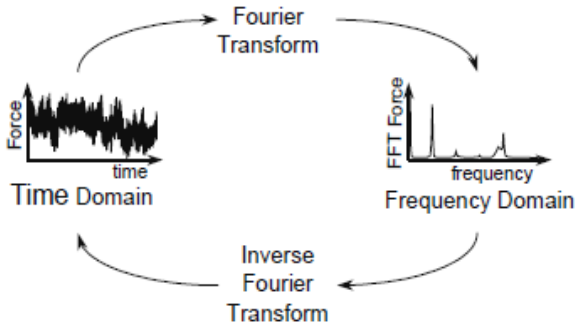

Figure 3.16 Fourier Transform [30]

Since the recorded data is in a discrete format, Fast Fourier Transform and Fast Inverse Fourier Transform are used to converting this discrete data in a very rapid and efficient way.

- Fast Fourier Transform

$$y(f_n) = \frac{2T}{N} \cdot \sum_k y(t_k) \cdot e^{-i\left(\frac{2\pi.n}{N}\right).k} \tag{3.13}$$

- Inverse Fourier Transform

$$y(t_k) = \frac{1}{T} \cdot \sum_n y(f_n) \cdot e^{i\left(\frac{2\pi.k}{N}\right).n} \tag{3.14}$$

Where T is the period of the function $y(t_k)$ and N is the number of data points for Fourier Transform.

Time domain signals are generally more complicated and difficult to understand especially for random data. On the other hand, frequency domain signals are much clear to understand which frequency have which amplitudes and phases. An example is given in Figure 3.17, where a signal consists of four sine waves at different amplitudes in the time domain and frequency domain.

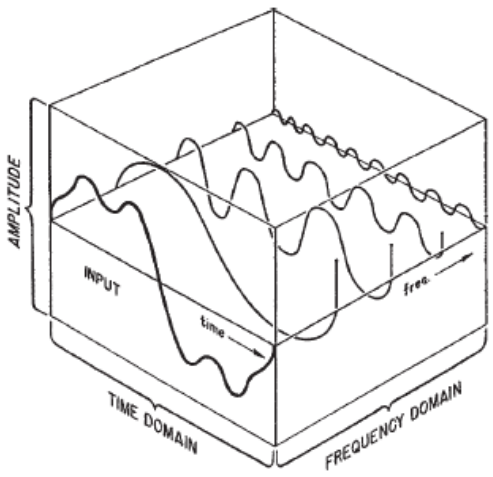

Figure 3.17 Time and frequency representations for a sinusoidal signal [47]

3.3.1. Time Domain Fatigue Analysis

In the time domain approach, fatigue analysis procedures are shown in Figure 3.18. For a loading condition, random stress history could be obtained via transient analysis or with experimental methods. In experimental case, random strain history is obtained via strain-gages located at the particular location of the structure and by using elastic modulus of the material, it could be converted to the stress history.

After obtaining the stress information, by using a cycle counting method such as rainflow cycle counting, irregular random data is decomposed and the stress range histogram is obtained. Palmgren-Miner's cumulative damage theory can be performed on this data and fatigue life of the structure can be found.

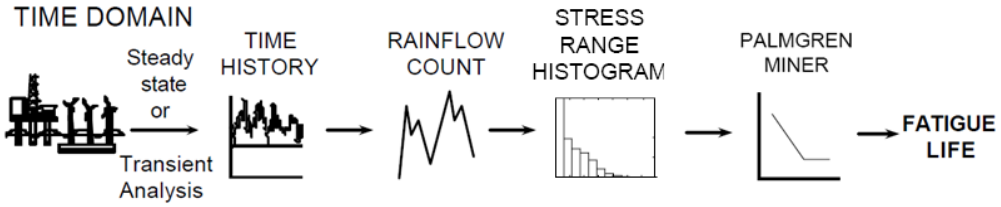

Figure 3.18 Time domain fatigue analysis procedure [30]

In the time domain transient simulations, the model is solved for each tiny time steps of input. Even this procedure gives accurate results, considering the number of data required to have statistically consistent results, this approach became computationally heavy and time-consuming.

If the stress history is obtained via experiments by using strain gauges, stress history is obtained only at the particular strain-gauge located position. That is why before the data acquisition procedure, the finite element model of the structure has to be created and the most critical location of the structure needs to be identified so that the location of the strain gauge can truly be determined. As a result, this analysis gives information about only a particular location rather than the entire life distribution. Moreover, if the geometry is changed for some reasons during the design stage, all the procedures need to be repeated for changed geometry.

3.3.2. Frequency Domain Fatigue Analysis

In the frequency domain approach, the procedures shown in Figure 3.19 is followed. First, time data acquired on the platform is converted to the frequency domain. Then the Power Spectral Density of the input data is obtained. By using the Transfer Function or in other words Frequency Response Function taken from the finite element model, response stress PSD at the critical position of the structure is achieved. By using the proper fatigue modeller such as Dirlik, Lalanne, and Narrow Band etc. Probability Density Function is obtained and it is used to calculate the fatigue damage and life of the structure.

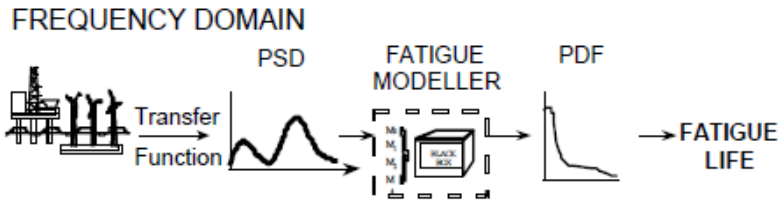

Figure 3.19 Frequency domain fatigue analysis procedure [29]

Random type of loadings are usually expressed in the frequency domain because the system behavior and characteristics can easily be recognized in the frequency domain while it cannot be said for time domain analysis. The response of a system can easily be obtained by using input loads and frequency response function, which is evaluated in the finite element environment. The frequency domain approach is much more computationally efficient way compared to time domain approach.

Since the study in this thesis carried on with the frequency domain approach, details of frequency domain approach will be given.

Since the mean value of a random signal remains relatively constant, Power Spectral Density functions are a very efficient way to handle this random data in a statistical way. Power Spectral Density of data can be obtained by taking the modulus squared of FFT and divide to the period time. So that the PSD function has no phase information anymore. However, the amplitude and frequency information are preserved.

$$PSD = \frac{1}{2T}|FFT|^2 \tag{3.15}$$

PSD basically describes the energy content of a signal over the frequency range. In Figure 3.20, the area under each bin represents the mean square value of each sine wave at that frequency and the total area under the curve gives the mean square value of the data.

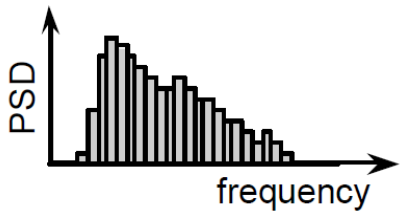

Figure 3.20 Power Spectral Density [29]

Some examples of time histories and corresponding PSDs are given below in Figure 3.21. In air platforms, encountered vibration level considered broadband due to their frequency content.

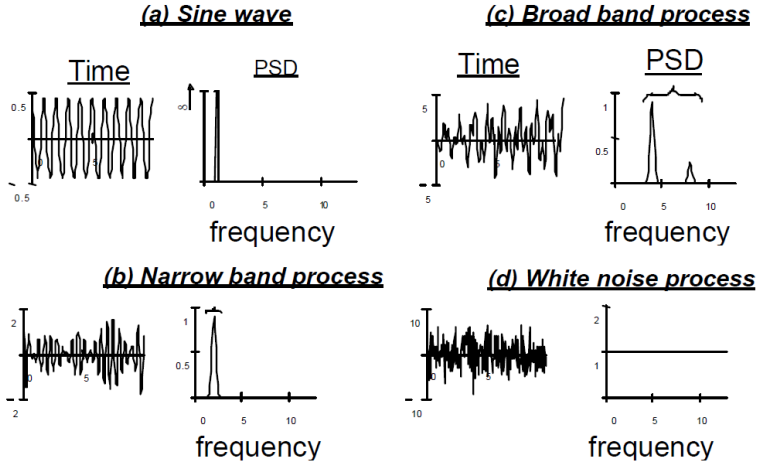

Figure 3.21 Different time histories and corresponding PSDs [29]

In the frequency domain fatigue calculations, if the system is linear, the response of the system can be found by multiplying the input with the linear transfer function.

$$FFT_{response} = TF \,.\, FFT_{input} \tag{3.16}$$

By using equation (3.15) and equation (3.16), response PSD can be written as,

$$PSD_{response} = \frac{1}{2T}\left(TF \,.\, FFT_{input} . TF^{*} \,.\, FFT_{input}{}^{*}\right) \tag{3.17}$$

$$PSD_{response} = TF.TF^{*}.PSD_{input} \tag{3.18}$$

$$PSD_{response} = |TF|^{2}.PSD_{input} \tag{3.19}$$

Where, TF^{*} and ${FFT_{input}}^{*}$ and are complex conjugate of the transfer function and complex conjugate of FFT input load, respectively. So, in order to find the response PSD of the system, which is the stress PSD in fatigue calculations, correct units are shown in the equation (3.20).

$$\frac{Mpa^{2}}{Hz} = \left(\frac{Mpa}{g}\right)^{2} \cdot \frac{g^{2}}{Hz} \tag{3.20}$$

In the case of n multiple loadings, the response PSD function could be obtained from equation(3.21).

$$PSD_{response} = \sum_{i=1}^{n}\sum_{j=1}^{n} TF_{i} \cdot {TF_{j}}^{*} \cdot PSD_{ij} \tag{3.21}$$

Input PSD matrix PSD_{ij} contains auto $(i = j)$ and cross terms $(i \neq j)$ where auto-PSD components have only real values but cross-PSD possess real and imaginary parts and they represent the correlation between inputs.

Stress PSD holds very important and useful properties for the statistical description of a random signal. The way to extract these useful statistical properties is the use of spectral moments of PSD. In theory, to be able to fully characterize the signal, all spectral moments are required. But in practice, only m_0, m_1, m_2 and m_4 are sufficient to characterize a signal [29].

$$m_n = \int_{0}^{\infty} f^{n} \cdot G(f) \cdot df = \sum_{k=1}^{N} f_k^{n} \cdot G_k(f) \cdot \Delta f \tag{3.22}$$

Where f is frequency, $G(f)$ is response PSD function, Δf is frequency increment and N is the number of sample points.

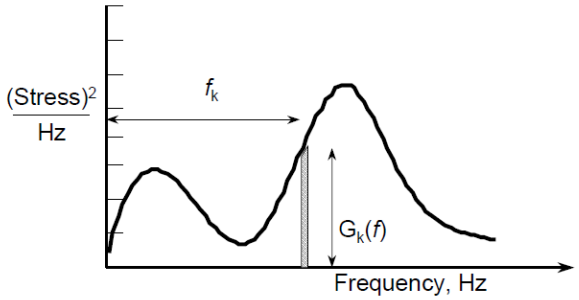

Figure 3.22 Definition of spectral moments of PSD function [30]

One of the major research on fatigue damage estimation from the PSDs is undertaken by S.O Rice in 1954 [22]. Rice found a relationship between spectral moments with the expected number of peaks E[P] and the expected number of upward zero crossing E[0].

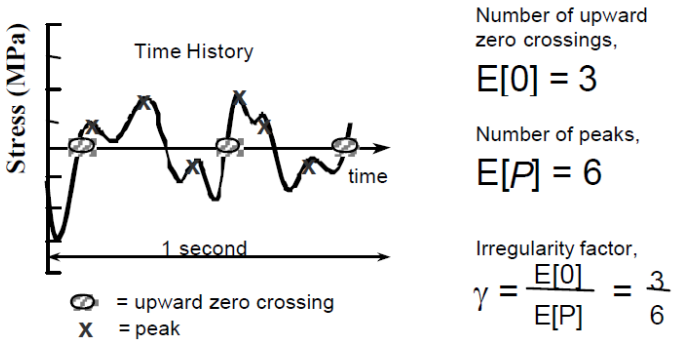

Figure 3.23 Zero crossings and peaks [29]

$$E[0] = \sqrt{\frac{m_2}{m_0}} \tag{3.23}$$

$$E[P] = \sqrt{\frac{m_4}{m_2}} \tag{3.24}$$

Also, by using $E[0]$ and $E[P]$, irregularity factor γ can be written as,

$$\gamma = \frac{E[0]}{E[P]} = \sqrt{\frac{m_2^2}{m_0 m_4}} \tag{3.25}$$

Irregularity factor γ is an important parameter for signals to distinguishing whether the signal is narrowband or broadband. If the irregularity factor is close to 1, the signal is considered narrowband and if it is close to 0, the signal is considered wide banded signal.

Also, RMS value and mean frequency x_m can be expressed by using spectral moments,

$$RMS = \sqrt{m_0} \tag{3.26}$$

$$x_m = \frac{m_1}{m_0}\sqrt{\frac{m_2}{m_4}} \tag{3.27}$$

In vibration fatigue calculations, in order to obtain fatigue damage $[ED]$, firstly Probability Density Function of rainflow stress ranges, $p(S)$ should be determined. A typical representation of the Probability Density Function is shown in Figure 3.24, where dS is the width of stress and the probability of stress range occurring between $S_i + \frac{dS}{2}$ and $S_i - \frac{dS}{2}$ is described as $p(S) \cdot dS$.

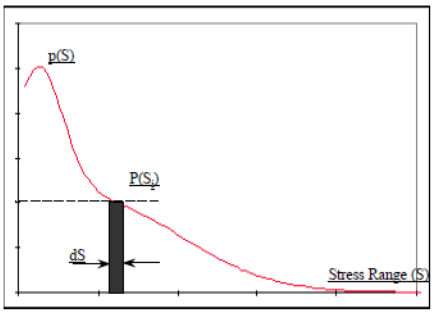

Figure 3.24 Probability Density Function [30]

There are many different empirical solutions to get the Probability Density Function $p(S)$, and these solutions are all related to the spectral moments of PSD. Some methodologies to get PDF is proposed by Bendat's Narrow Band, Tunna, Wirsching, Hancock, Chaudhury and Dover, Steinberg, Dirlik and Lalanne.

- Bendat's Narrow Band Approach

$$p(S) = \frac{S}{4 \cdot m_0} \cdot e^{\left(\frac{-S^2}{8 \cdot m_0}\right)} \tag{3.28}$$

Bendat's narrowband approach is extremely conservative when it is used for wideband time histories. Because in the Bendat's narrow band solution, all positive peaks are matched with a negative valley with the same magnitude so that as it is shown in Figure

3.25, a wideband red signal is transformed to the green signal and stress cycles become much greater compared to the normal signal. That is why some methods such as Tunna, Wirsching, Hancock and Chaudhury&Dover are proposed to correct the narrowband conservatism.

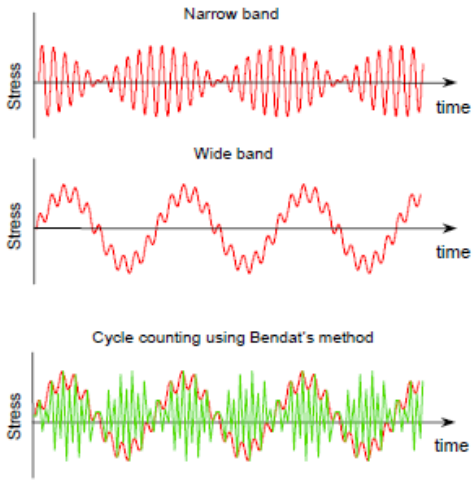

Figure 3.25 Representation of Narrow Band conservatism [43]

In the literature, one of the best and mostly used solution is Dirlik's approach [28]. It is suitable for both narrowband and wideband signals and in terms of accuracy, it is superior to narrowband and the methods based on correction to narrowband.

- Dirlik Approach:

$$p(S) = \frac{1}{2\sqrt{M_0}}\left[\frac{D_1}{Q}e^{\frac{-Z}{Q}} + \frac{D_2 Z}{R^2}e^{\frac{-Z^2}{2R^2}} + D_3 Z e^{\frac{-Z^2}{2}}\right] \tag{3.29}$$

Where, D_1, D_2, D_3, Q and R are all functions of m_0, m_1, m_2 and m_4.

$$D_1 = \frac{2(x_m - \gamma^2)}{1+\gamma^2} \qquad D_2 = \frac{1-\gamma-D_1+D_1^2}{1-R} \qquad D_3 = 1 - D_1 - D_2$$

$$Q = \frac{1.25(\gamma - D_3 - D_2 R)}{D_1} \qquad R = \frac{\gamma - x_m - D_1^2}{1-\gamma-D_1+D_1^2} \qquad Z = \frac{S}{2\sqrt{m_0}}$$

Another very efficient method is proposed by Lalanne and it is just like Dirlik's method, one of the best solutions to obtain the Probability Density Function.

- Lalanne Approach:

$$p(S) = \frac{1}{2.rms}\left\{\frac{\sqrt{1-\gamma^2}}{\sqrt{2\pi}} e^{\frac{-S^2}{8.rms^2(1-\gamma^2)}} + \frac{S\cdot\gamma}{4\cdot rms} e^{\frac{-S^2}{8.rms^2}}\left[1 + \text{erf}\left(\frac{S\cdot\gamma}{2rms\sqrt{2(1-\gamma^2)}}\right)\right]\right\} \tag{3.30}$$

Where $\text{erf}(x) = \frac{2}{\sqrt{\pi}}\int_0^x e^{-t^2} dt$.

After deciding the proper PDF obtaining method, the number of cycles at the particular stress level $n(S)$ can be found as,

$$n(S) = p(S) \cdot dS \cdot S_t \tag{3.31}$$

Where S_t is the total number of cycles in time and it can be expressed as $E[P] \cdot T$. Here $E[P]$ is the number of peaks per second and T is the random loading exposure duration in seconds. So that the equation becomes,

$$n(S) = E[P] \cdot T \cdot p(S) \cdot dS \tag{3.32}$$

According to Palmgren-Miner's Cumulative Damage Theory, as it is stated in the equation(3.8), total damage can be found by dividing the total cycle at that particular stress $n(S)$ by the maximum cycle that the material withstands $N(S)$ according to Wohler's S-N curve. By substituting equation(3.32) and equation(3.1) into equation(3.8), damage of a particular location can be calculated as follows,

$$[ED] = \sum \frac{n(S)}{N(S)} = \int_0^\infty \frac{E[P] \cdot T \cdot p(S) \cdot dS}{C \cdot S^{-b}} = \frac{E[P] \cdot T}{C} \int_0^\infty S^b \cdot p(S) \cdot dS \tag{3.33}$$

Here, it is very important to remark that in the S-N curve most of the time stress is defined with alternating stress but at the probability density function, stress is defined with the stress range. So, the stress definition in $n(S)$ and $N(S)$ must be made identical according to the relation between stress range and alternating stress. In addition, to be able to obtain a numerical result, the upper limit of the integral must be defined with a cut-off value. It is commonly limited to 6 times the RMS stress range [29].

Finally, when $[ED]$ is equal to 1, the material fails and the life of the structure can be found with the equation given below,

$$Life = T/[ED] \tag{3.34}$$

3.4. Vibration PSD Synthesis and Accelerated Life Testing

The fatigue process mainly occurs in long-term durations. To be able to validate the integrity of the structure under fatigue type of loadings, reliability and safety of structure has to be ensured for whole service life. One way to validate the safety and reliability of the structure under service loading is by simulating this environment in laboratory conditions. However, simulating the whole service life in test conditions is not possible due to time and cost constraints. In such a case, fatigue damage spectrum phenomena can be used to obtain test condition vibration loadings where damage capability remained same but duration and amplitudes are scaled.

Fatigue Damage Spectrum, which is first proposed by Lalanne [48] is the damage content of signal on an SDOF system as a function of natural frequency and it can be directly related to Power Spectral Density value. The method assumes that the signal is stationary, has a Gaussian distribution and has zero mean.

FDS can be written in the form of equation(3.35)

$$D(f_n) = \frac{f_n T}{C}\left[\frac{G(f_n)k^2}{8\pi f_n \zeta}\right]^{b/2} \Gamma[1 + b/2] \tag{3.35}$$

Where k is the spring stiffness of the SDOF system, Γ is the gamma function defined as $\Gamma(g) = \int_0^\infty x^{(g-1)}.e^{-x}dx$, b and C are fatigue parameters described in Wohler's S-N curve.

When the constant terms are gathered, equation(3.35) can be written as,

$$D(f_n) = const.\, f_n T\left[\frac{G(f_n)}{f_n \zeta}\right]^{b/2} \tag{3.36}$$

The last expression of the equation above is defined as “damage potential spectrum” [49]

$$DP(f_n) = f_n T \left[\frac{G(f_n)}{f_n \zeta}\right]^{b/2} \tag{3.37}$$

Since fatigue damage is based on the cumulative effect of various loadings, it can be represented with Palmgren Miner’s cumulative damage theory as given below [50],

$$DP_{test}(f_n) = DP_1(f_n) + DP_2(f_n) + \cdots + DP_N(f_n) \tag{3.38}$$

For test condition;

$$f_n T_{test} \left[\frac{G_{test}(f_n)}{f_n \zeta}\right]^{\frac{b}{2}} = f_n T_1 \left[\frac{G_1(f_n)}{f_n \zeta}\right]^{\frac{b}{2}} + f_n T_2 \left[\frac{G_2(f_n)}{f_n \zeta}\right]^{\frac{b}{2}} + \ldots + f_n T_N \left[\frac{G_N(f_n)}{f_n \zeta}\right]^{b/2} \tag{3.39}$$

After simplifying both sides of the equation with common terms,

$$T_{test}[G_{test}(f_n)]^{b/2} = T_1[G_1(f_n)]^{b/2} + T_2[G_2(f_n)]^{b/2} + \cdots + T_N[G_N(f_n)]^{b/2} \tag{3.40}$$

Eventually, test PSD can be obtained as below,

$$G_{test}(f_n) = \left(\frac{T_1[G_1(f_n)]^{b/2} + T_2[G_2(f_n)]^{b/2} + \cdots + T_N[G_N(f_n)]^{b/2}}{T_{test}}\right)^{2/b} \tag{3.41}$$

MIL-STD-810G Method 514.6 Annex A stated that exponent b is not directly equal to the slope of the S-N curve. Although it is strongly influenced by the slope of the S-N curve, it is also influenced by the surface finish, the treatment, the effect of mean stress correction, the contributions of elastic and plastic strain, the wave shape of the strain time history, etc. Therefore, in the MIL-STD-810G, b is replaced with m. It suggests taking "m" as 80 percent of "b" for random waveshapes. Historically $m = 7.5$ has been used for random environments but values between 5 and 8 are also commonly used [51].

For such a case where a single PSD data is accelerated to a shorter or longer duration, equation (3.42) is used,

$$\frac{T_2}{T_1} = \left[\frac{G_1(f_n)}{G_2(f_n)}\right]^{m/2} \tag{3.42}$$

$\frac{G_1(f_n)}{G_2(f_n)}$, commonly known as exaggeration factor and it is recommended to be kept to a minimum value and should not generally exceed 2.0 [51]. In addition, it is important to note that after accelerating the data, stress levels must be checked carefully. Sometimes accelerating data would increase stress levels more than or close to yield strength of the material and the number of cycles to failure could be in the range of low cycle fatigue and it is undesired for stress life approaches.

4. FINITE ELEMENT MODEL OF THE STRUCTURE

Since the fatigue calculations will be carried based on the finite element model of the structure, it is very important to construct the finite element model accurately. Therefore, first of all, the 3D model of the structure is modelled in PTC Creo. The avionic unit, which is held in between brackets, consists of many electronic cards and components inside. Since in the next levels of study whole assembly will be tested with experiments and it could be harmful to properly working electronic components, replicated dummy versions of these electronic components are designed with aluminum material. During this design stage, center of gravities, weights and moments of inertia values of each electronic cards are preserved to be able to represent the real behavior of electronic cards and components.

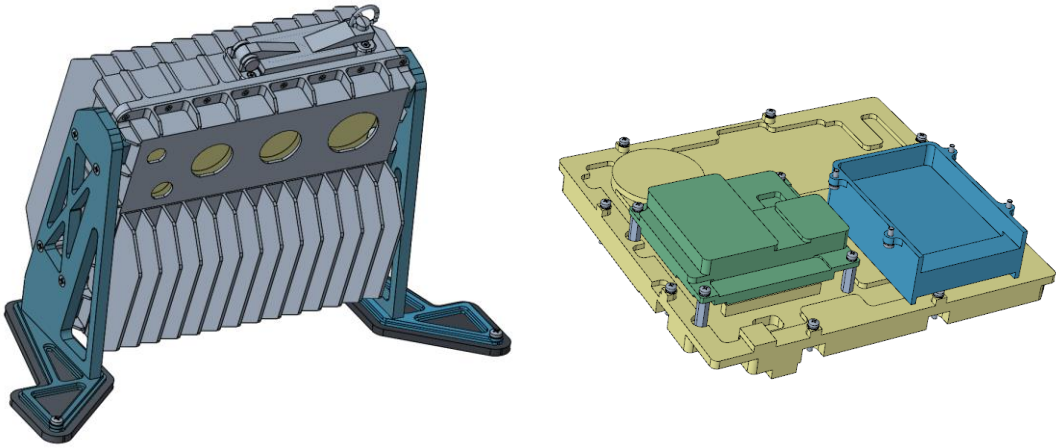

Figure 4.1 CAD models of brackets, avionic unit and internal dummy cards

After the 3D model of the structure is obtained, geometry is imported to ANSYS 2020 R2 Workbench. Since importing complex geometries such as locking mechanism in the avionic unit may require very small mesh elements, this locking mechanism is modelled with point mass as shown in Figure 4.2. Brackets are assigned aluminum 7075-T6 and all other parts are assigned aluminum 6061-T6. See Appendix-B for the mechanical properties of aluminum 6061-T6 and aluminum 7075-T6.

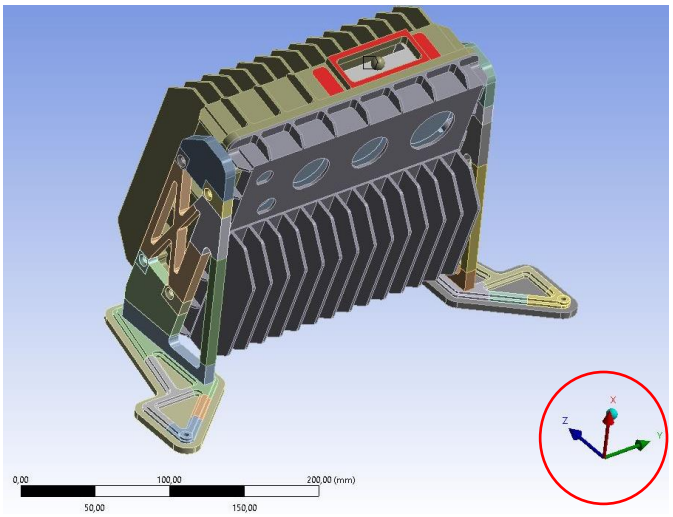

Figure 4.2 ANSYS model of structure and used coordinate system

4.1. Contact Modelling

All screws except the ones inside of the avionic unit are modelled with deformable structural steel beam element as shown in Figure 4.3. Beams are applied to the washer and countersunk areas as well so that it represents the screws more realistic. For the ones inside the avionic unit, bonded contacts are used to connect the electronic cards and frames from their contacting interfaces.

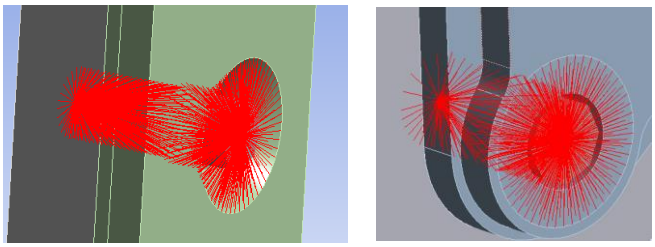

Figure 4.3 Screw modelling with beam elements

After applying beam elements to the system, the next step is to define the contacts between parts. Here, changing contact types and contact areas between the wall, brackets and avionic unit changes the natural frequencies as well. That is why after performing the experimental modal analysis of the structure (see Chapter 5.1), natural frequencies in real conditions are obtained and according to that, contact types and radius of contact areas between parts changed parametrically to have similar natural frequencies from the finite element model. After many iterations, a true representation of the real structure is obtained in finite element model and contact types and contact areas are decided as shown in Figure 4.4 and Figure 4.5.

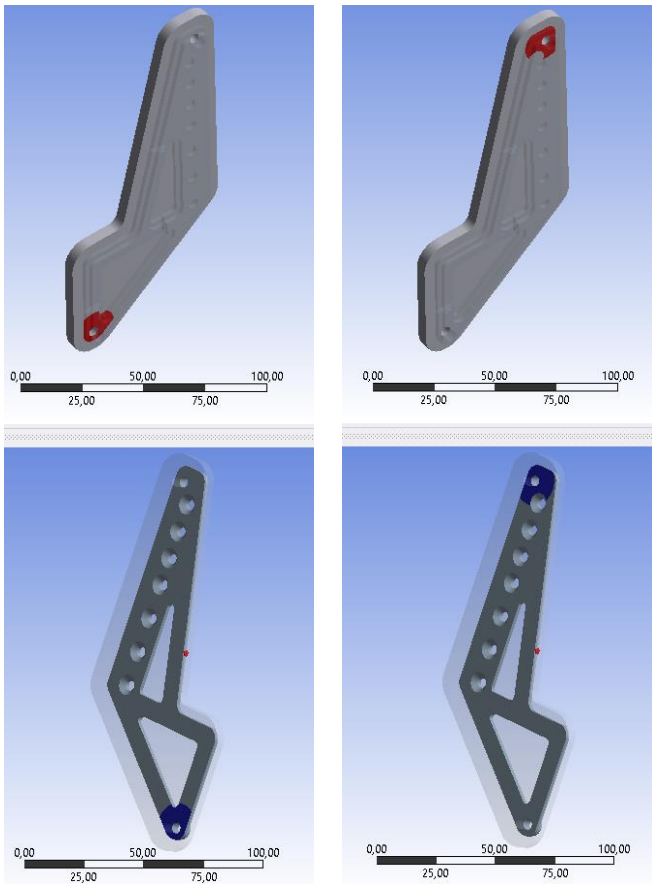

Figure 4.4 Wall - 1st brackets no separation contact

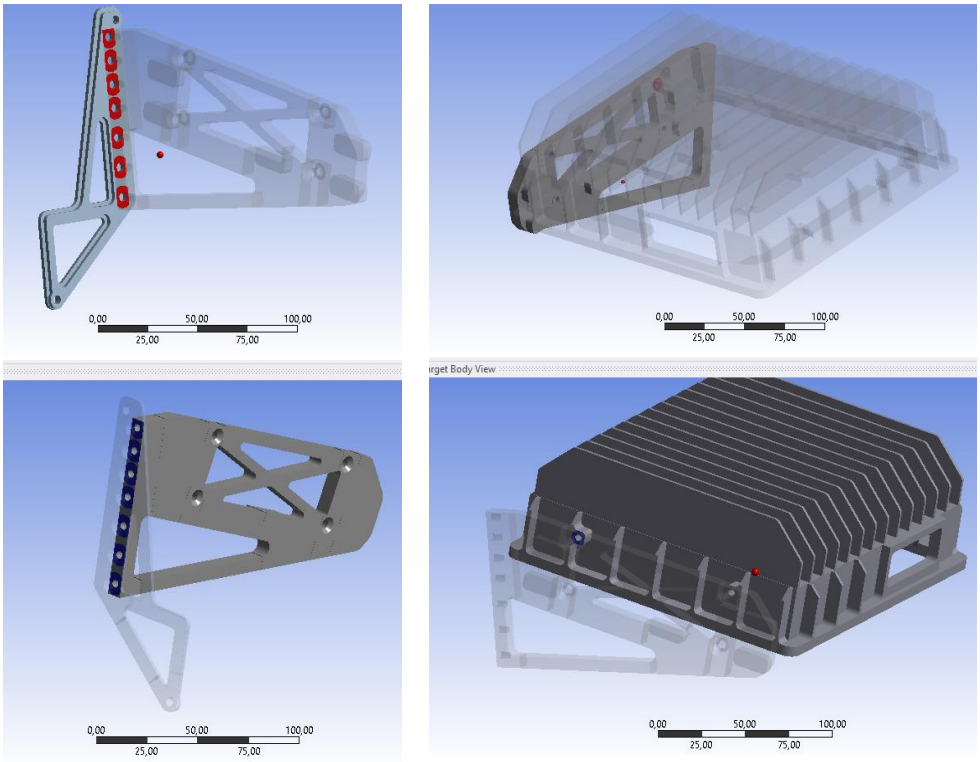

Figure 4.5 1st - 2nd brackets no separation contact and 2nd bracket - avionic unit bonded contact

4.2. Mesh Generation

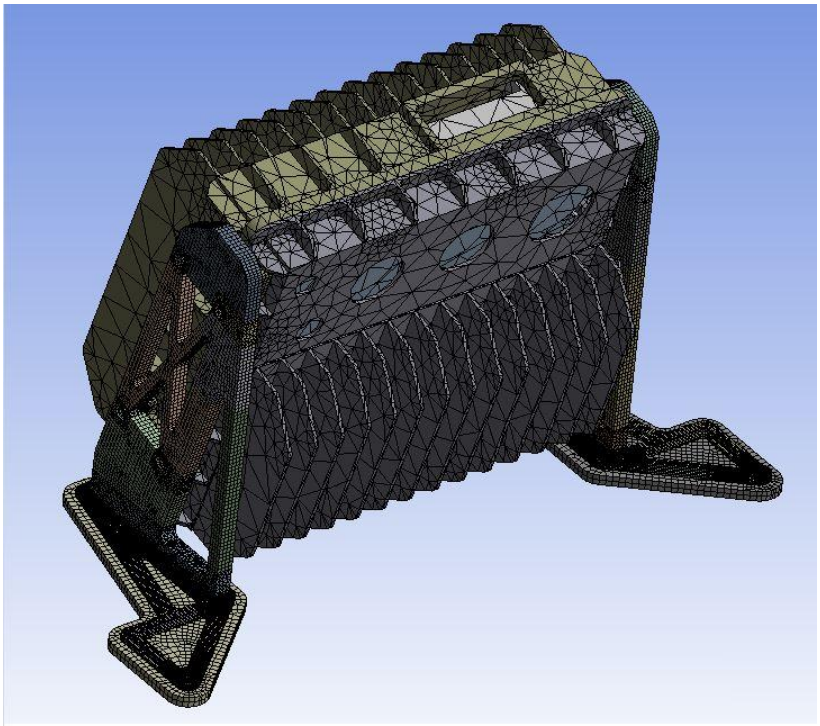

Figure 4.6 Meshing whole structure

Avionic unit meshed very coarsely since meshing size or meshing quality of avionic unit has a negligible effect on modes of the structure or the response of the structure. However, since the main interests are the brackets, a special effort has been made to meshing the brackets.

Brackets are split into many subparts and these parts are connected to each other with shared topology in ANSYS Space Claim and each individual subpart is meshed separately. Parts, which are appropriate for hexahedral meshing are meshed with 20 nodes hexahedral elements, while parts that include many holes and irregular shapes are meshed with 10 nodes tetrahedron elements. The reason for doing this operation is since the geometries have many holes, notches, fillets, split faces and irregular geometries, ANSYS Mechanical try to mesh the entire geometry with one type of element and it is most probably tetrahedrons. This is not something desired because even some geometries must be meshed with tetrahedrons, meshing all bodies with tetrahedrons may result with an excessive number of elements. In addition, hexahedral meshes are more reliable compared to tetrahedrons. Splitting bodies and meshing separately gives the user much more freedom to mesh the desired type.

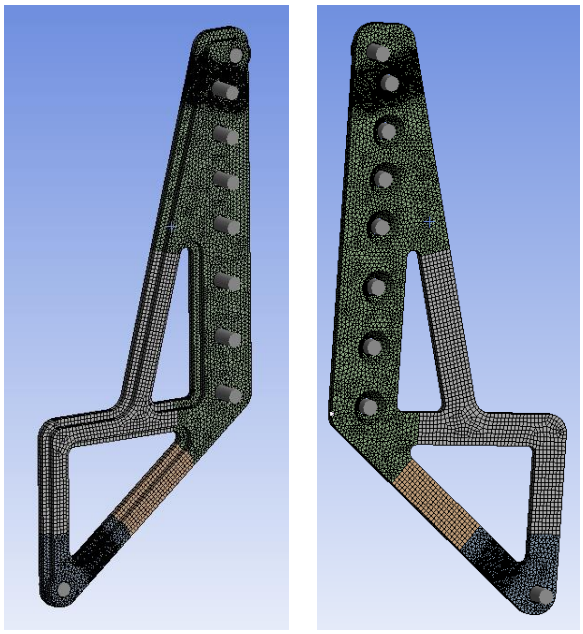

Figure 4.7 1st bracket 1 mm general sizing with 0.5 mm local sizing in critical areas

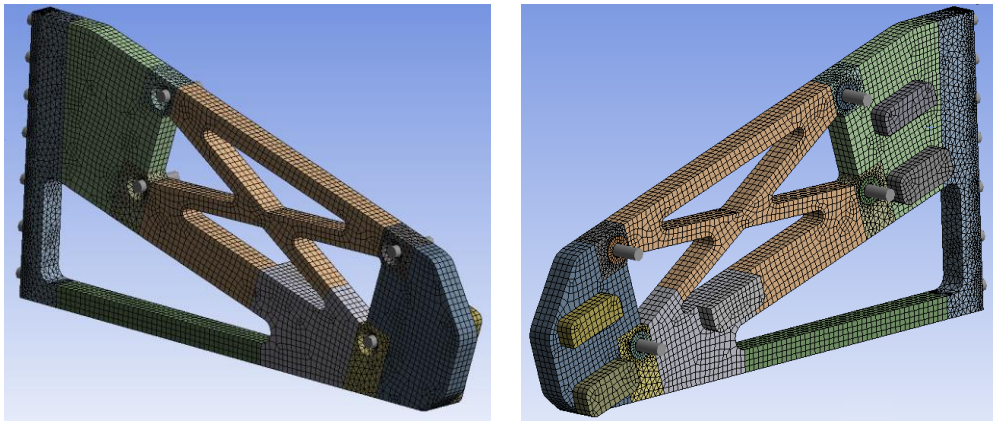

Figure 4.8 2nd bracket 2 mm general sizing

In Table 4.1 below, comparison of used split body method and standard tetrahedron meshing of ANSYS for brackets are given. It is obvious that the splitting geometries and meshing separately increase the mesh quality and decrease the number of elements and nodes.

Table 4.1 Comparison of mesh statistics for different meshing methods

METHOD	PART	ELEMENT QUALITY	NUMBER OF ELEMENTS	NUMBER OF NODES
All Tetrahedrons	1st bracket	83.80%	155953	235272
	2nd bracket	82.77%	123763	189683
Split mesh	1st bracket	84.00%	74350	128417
	2nd bracket	83.91%	56735	121584

4.3. Mesh Convergence Analysis and Singularity Point Handling

Fatigue analysis is very sensitive to stress. Even small changes in stress may have a massive effect on the life of the structure. If the stress history is created in the finite element environment, it is very important to have a finite element model that has very similar responses to the real structure. Nevertheless, even the FEA model is verified with experiments, some other uncertainties may occur in the FEA results and one of them is singularity points.

In the finite element model when the mesh is refined continuously, results will approach a limiting value and further refinements of mesh does not change the results anymore. This is called a mesh independence solution. But sometimes it does not happen and results will not approach a limiting value. Even the mesh is increased continuously, the stress results get higher. This is called the singularity point and the theoretical stress is infinite at these locations. Singularity points have to be handled very carefully. Using the singularity point results in analysis or calculations will definitely cause to find incorrect results.

There could be many reasons for the formation of stress singularities. Sharp edges, applying loads or constraints on a single point or edge, in a contact region where there is a geometric discontinuity or split faces may be the reason.

In this study, mesh convergence and singularity point handling analysis are performed in the z-direction, the weakest direction of the structure. First of all, random vibration analysis is performed with 5-500 Hz interval, with an amplitude of 0.001 $\frac{g^2}{hz}$ white noise input with a 0.02 damping ratio. In the model, a singularity point has appeared on both 1st brackets at the connection of split faces and the countersunk outer diameter as shown in Figure 4.9. Split faces cannot be deleted or changed to remove the singularity since split faces geometries are found with many iterations to be able to coincide the modes of the structure and the responses obtained from experiments. However, it is very important to obtain reliable stress results to be able to get the trustful fatigue life of the structure.

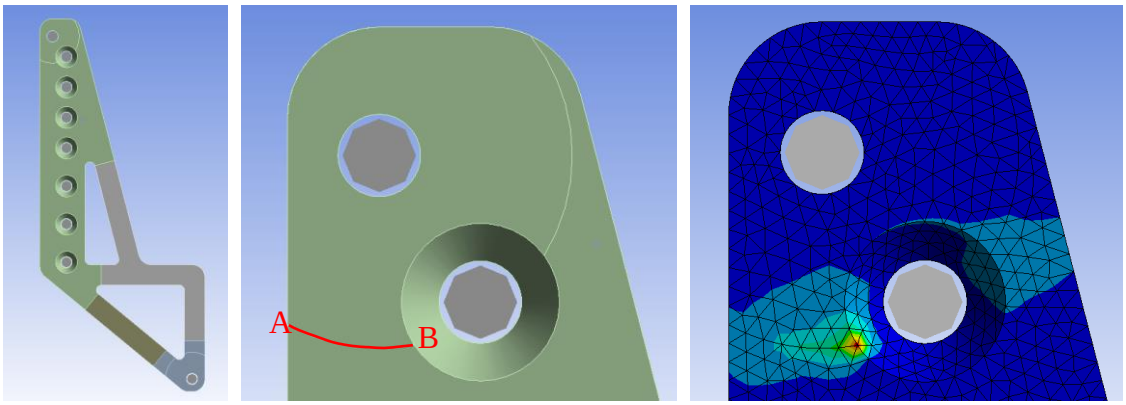

Figure 4.9 Singularity position in the 1st bracket

To be able to understand the singularity points behavior, first of all, the mesh is refined on the AB line and the stress results of this line are investigated. In Figure 4.10, it is obvious that even the mesh is increased, any point on the AB line does not converge to any value except the results very close to point A. It is concluded that stress result on the AB line is not reliable.

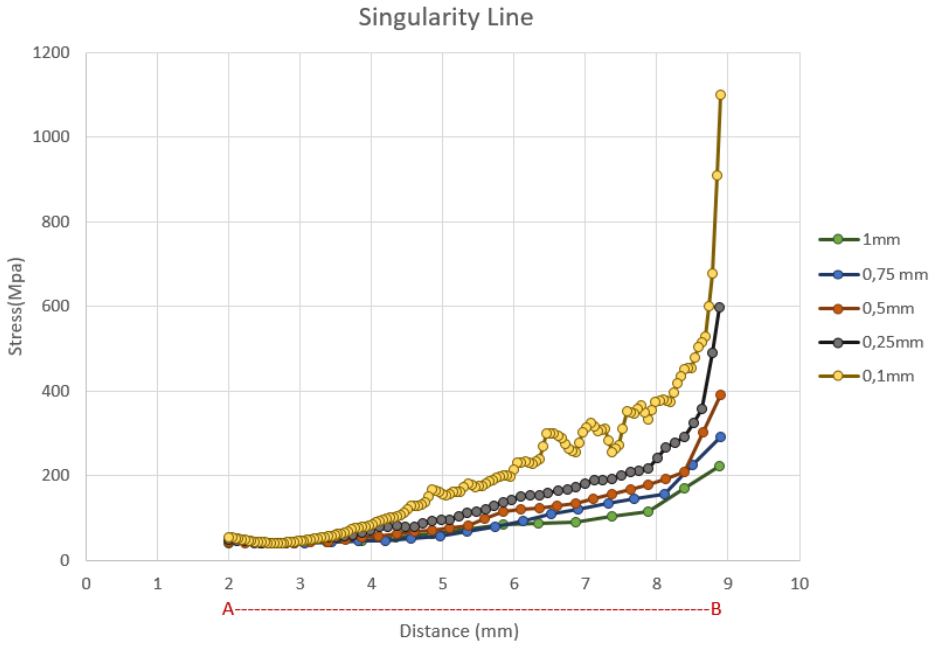

Figure 4.10 Stresses on the singularity line AB with an increasing mesh size

Since the stress levels around the singularity point are not representing the real values, the critical location of the structure is decided according to maximum stresses except the singularity area and the mesh convergence is performed at these locations. High stress regions except the singularity areas are given in Figure 4.11.

Figure 4.11 High stress regions of the structure except for singularity areas

According to the high stress regions, mesh convergence analysis is performed. In Figure 4.12, Figure 4.13, Figure 4.14 and Figure 4.15, the effect of increasing local mesh size on the stresses can be seen.

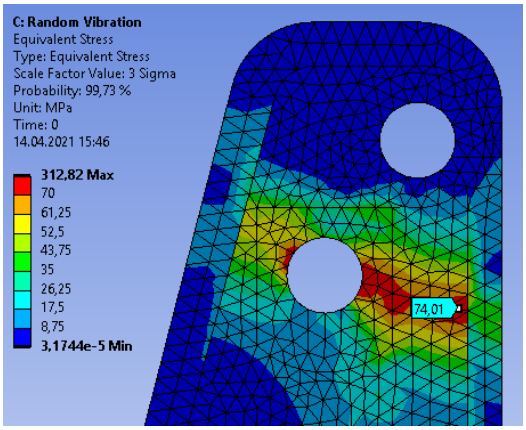

1 mm mesh

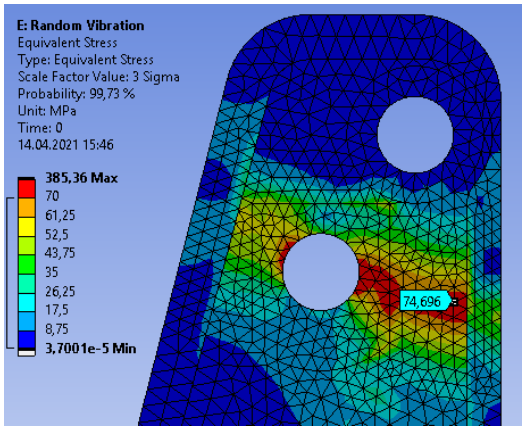

0.75 mm mesh

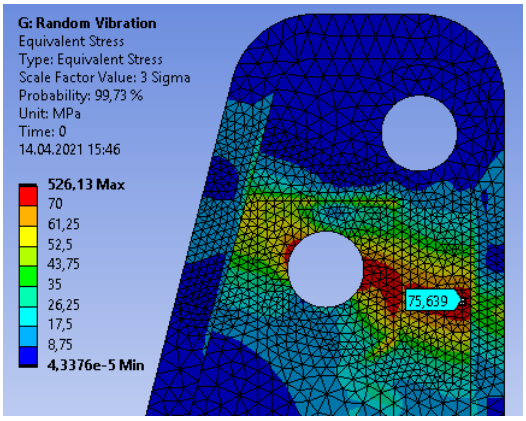

0.5 mm mesh

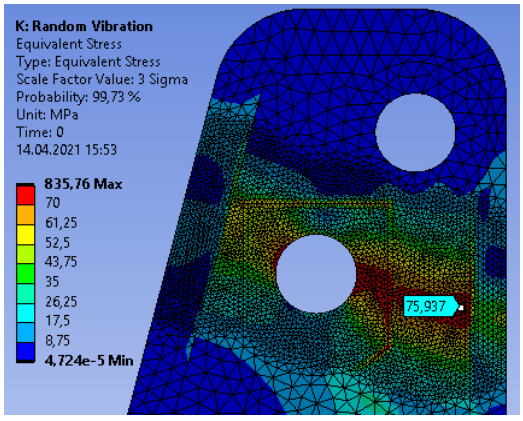

0.25 mm mesh

Figure 4.12 Mesh convergence analysis of the critical location-left bracket upper part

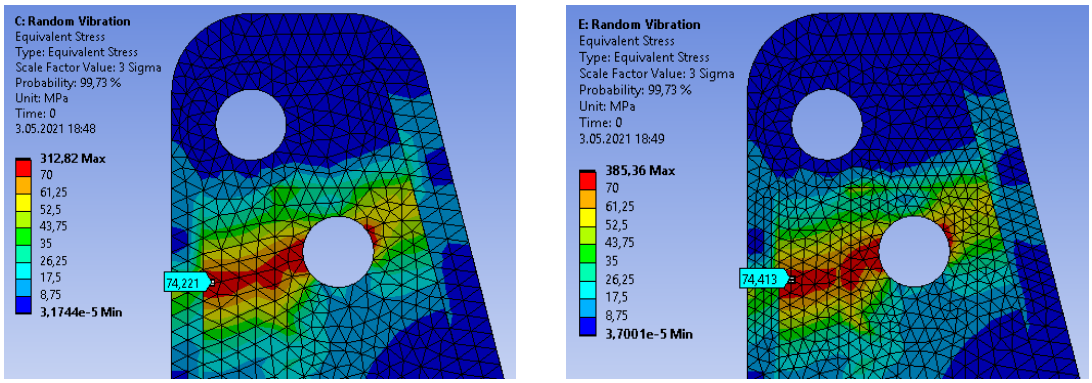

1 mm mesh 0.75 mm mesh

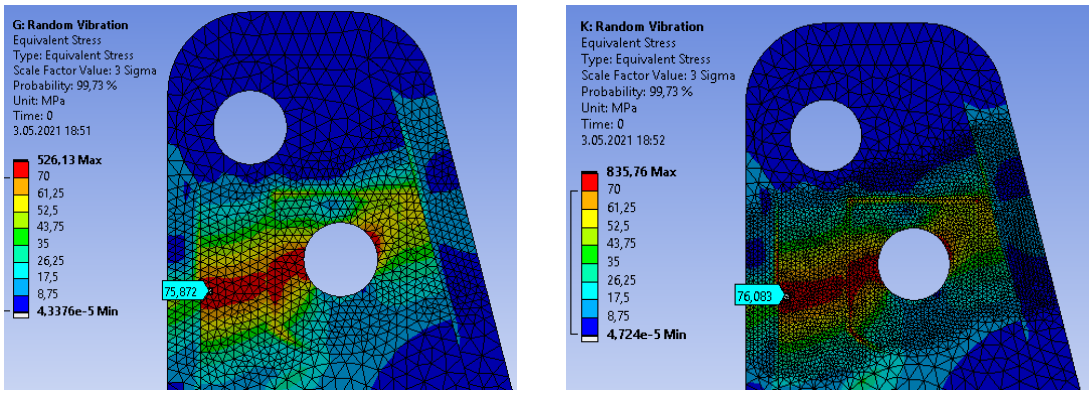

0.5 mm mesh 0.25 mm mesh

Figure 4.13 Mesh convergence analysis of the critical location-right bracket upper part

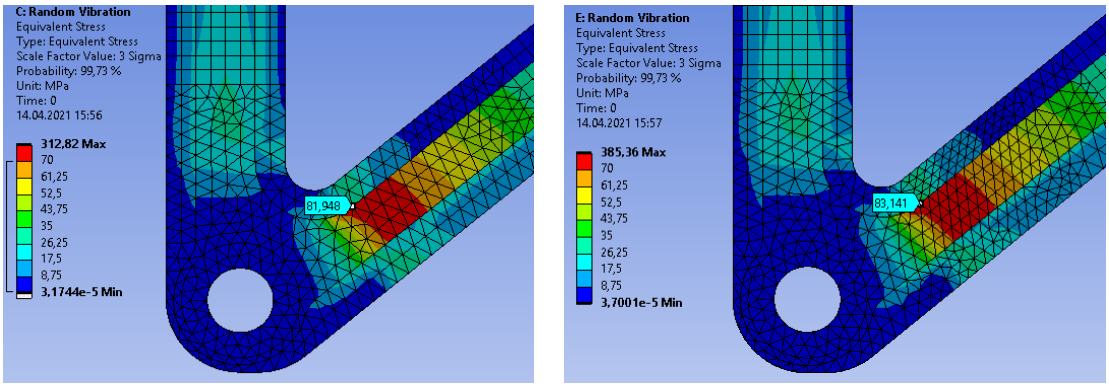

1 mm mesh 0.75 mm mesh

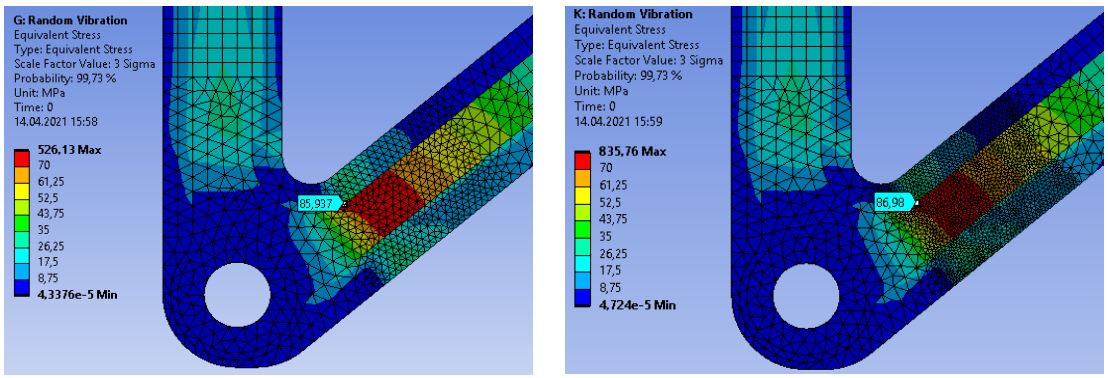

0.5 mm mesh 0.25 mm mesh

Figure 4.14 Mesh convergence analysis of the critical location-left bracket lower part

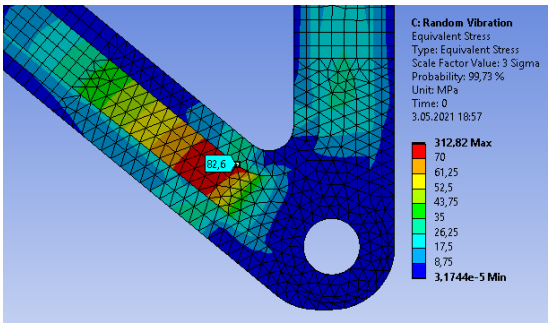

1 mm mesh

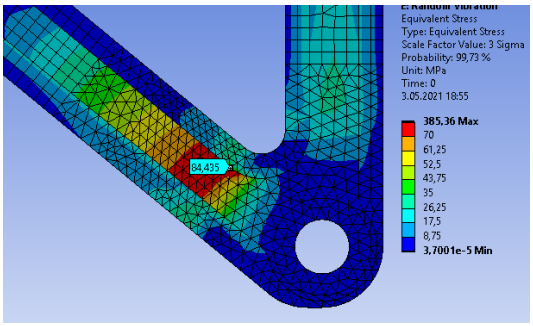

0.75 mm mesh

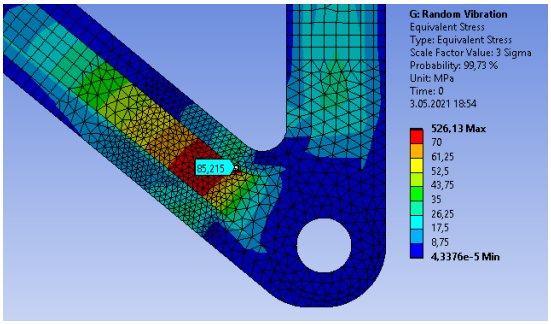

0.5 mm mesh

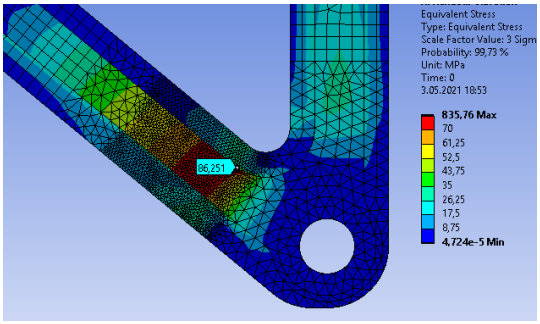

0.25 mm mesh

Figure 4.15 Mesh convergence analysis of the critical location-right bracket lower part

From the mesh dependence analysis, it is seen that the most damage potential locations are the radius edges at the lower part of the brackets on both left and right side given in the Figure 4.14 and Figure 4.15. According to Table 4.2, 0.5 mm local mesh is chosen for further analysis and for that mesh size, the most critical node id's are found to be 19067 on the left and 791796 on the right.

Table 4.2 Local mesh refinements and stress levels

Local Mesh Size (mm)	**Left bracket upper part Stress (Mpa)**	**Right bracket upper part Stress (Mpa)**	**Left bracket lower part Stress (Mpa)**	**Right bracket lower part Stress (Mpa)**
1	74.01	74.221	81.948	82.6
0.75	74.696	74.413	83.141	84.435
0.5	75.639 (node 22369)	75.872 (node 794658)	**85.937 (node 19067)**	**85.215 (node 791796)**
0.25	75.937	76.083	86.98	86.251

5. VERIFICATION OF FINITE ELEMENT MODEL

Fatigue calculations will be carried on according to the stresses created in the finite element model and that is why it is very important to have a reliable and verified finite element model of the structure. To do that several analysis will be carried on in FEA and experimental environment. Comparing parameters are given below,

- Natural frequencies obtained from experiments and ANSYS Modal Analysis
- Acceleration transmissibilities obtained from experiments and ANSYS Harmonic Analysis
- Acceleration PSD's obtained from experiments and ANSYS Random Analysis

Comparing only natural frequencies are not enough to conclude that the model is verified with experiments. Because even if the natural frequencies of the structure coincide with the experimental results, damping information is also required in order for the finite element model to represent the real conditions. So that peaks of the frequency response functions are also needed to coincide in order to say the model is verified. That is why the acceleration transmissibilities and acceleration PSDs are compared with experimental results to conclude the model is verified and can be used for further analysis.

5.1. Experimental Modal Analysis

After the CAD model is designed, brackets and avionic unit including dummy electronic cards are manufactured and all system assembled and prepared for experimental modal analysis. The aim is to find the modal parameters such as the natural frequencies and damping ratios and obtaining the acceleration transmissibility and acceleration PSDs. Two accelerometers located on the brackets shown in Figure 5.2. Tools that are used to perform experimental modal analysis and their specifications are given in Figure 5.1 and Table 5.1.

Figure 5.1 Tools of experiment setup

Table 5.1 Instruments of Experiment Setup

Accelerometer	Brüel & Kjaer Type 4507B and Type 4524B
Signal Processor	Bruel & Kjaer Pulse 3560
Software	Pulse Labshop 16.1
Shaker	LDS V8-440

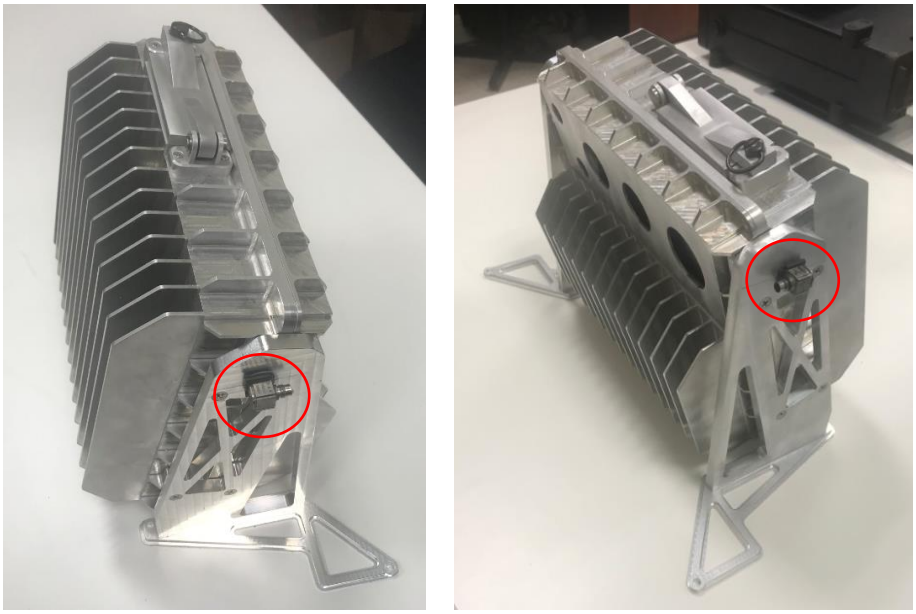

left accelerometer right accelerometer

Figure 5.2 Accelerometer locations on the brackets

Two tests are performed in the shaker as shown in Figure 5.3. The amplitude of 0.001 $\frac{g^2}{hz}$ white noise up to 2000 Hz is applied to the shaker and the frequency resolution for the responses are set to 0.3125 Hz.

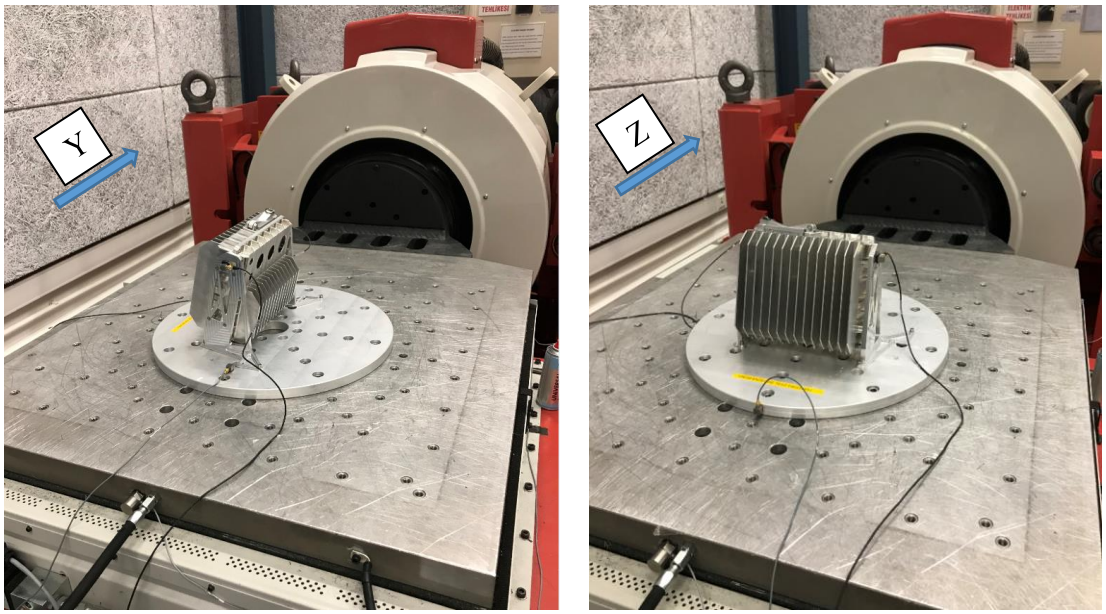

Figure 5.3 Two test directions in experiments

Obtained acceleration transmissibilities and acceleration PSDs are given in Figure 5.4 and Figure 5.5.

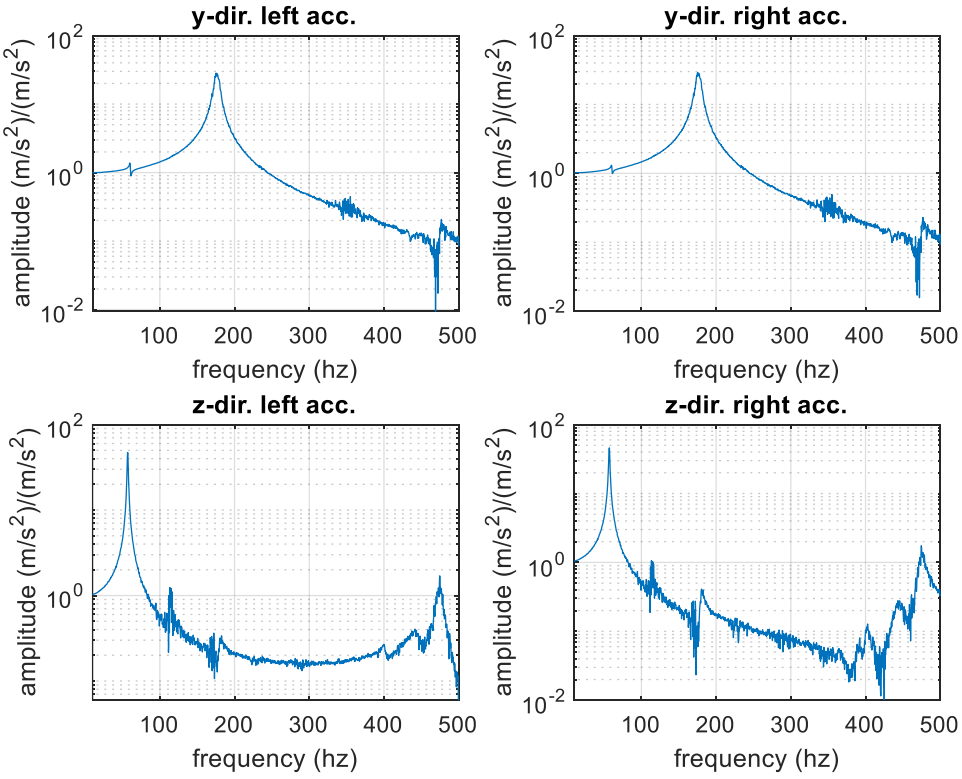

Figure 5.4 Transmissibilities in y and z directions in left and right accelerometers

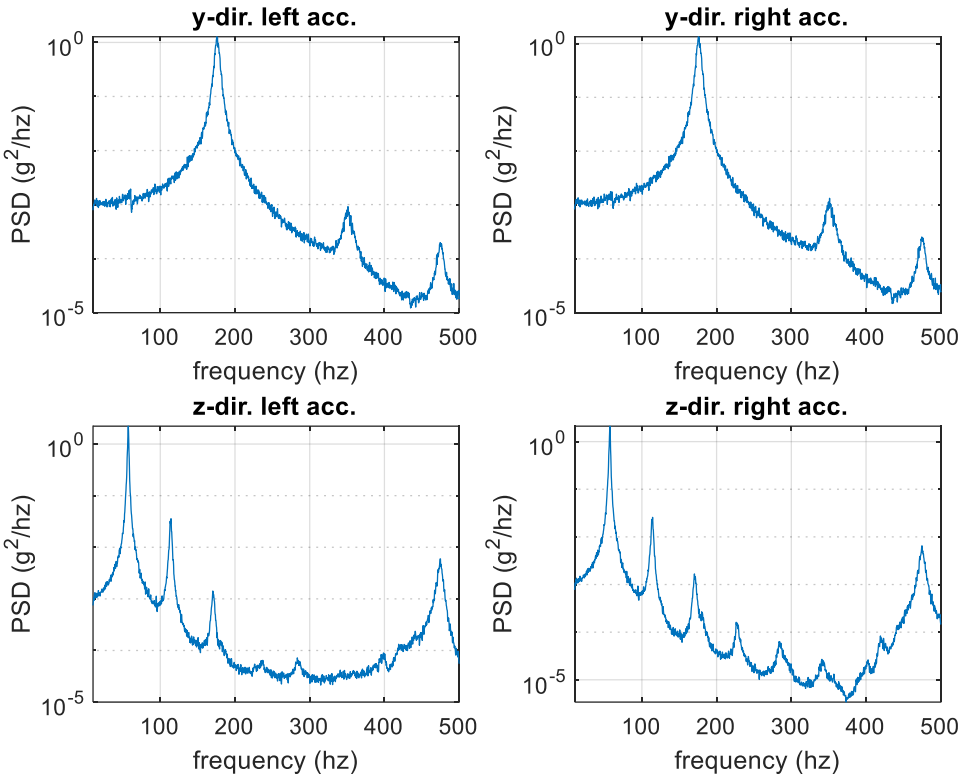

Figure 5.5 Acceleration PSDs in y and z directions in left and right accelerometers

From the transmissibility figures, damping ratios found from the half power bandwidth method (See Appendix A) and the natural frequencies obtained from experiments are given in Table 5.2.

Table 5.2 First three natural frequencies and corresponding damping ratios

Mode number	**Natural Frequency (Hz)**	**Damping Ratio**
1	56.88	0.012
2	175.31	0.018
3	474.69	0.007

In the acceleration transmissibility and acceleration PSD figures, it is obvious that there is a sort of distortion or a kind of harmonic excitation that creates small amplitudes of peaks at the multiples of natural frequencies. Although these peaks are not drawn attention in linear scale plots, they stand out in logarithmic scale plots like Figure 5.4 and Figure 5.5.

After many tests have been performed, it is founded that when the dummy cards and the avionic unit are held with hands from the connector gap during tests, this effect disappears. Most probably, some parts are interacting with hitting each other during excitation and holding this structure diminishes this effect. Comparison of hand-held and non-hand-held cases are given in Figure 5.6.

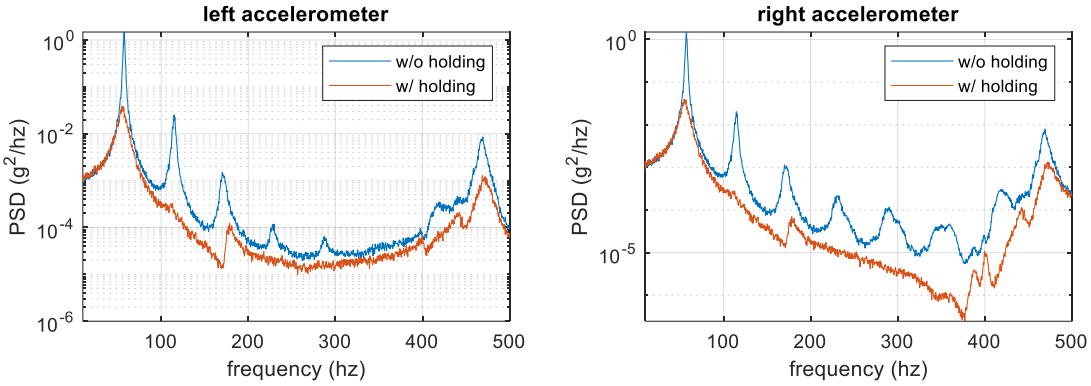

Figure 5.6 Acceleration PSDs w/ hand holding and w/o hand holding cases

Possible hitting locations, where the dummy cards, avionic unit's frame and brackets are relatively close to each other are investigated in the CAD program. Some predicted hitting location in the aluminum structure is trimmed in the manufacturing laboratory. However, it is important to mention that trimming could not be operated in all close regions because it is not possible to trim these regions at this stage. In order to do such an operation, brackets and dummy cards should be designed from the beginning with this perspective.

After trimming the parts, another test in the shaker structure is performed to see whether the operation is worked out or not. However, the trimming operation did not work and the peaks at the multiples of natural frequencies still arisen. In Figure 5.7, acceleration PSDs of trimmed parts are given.

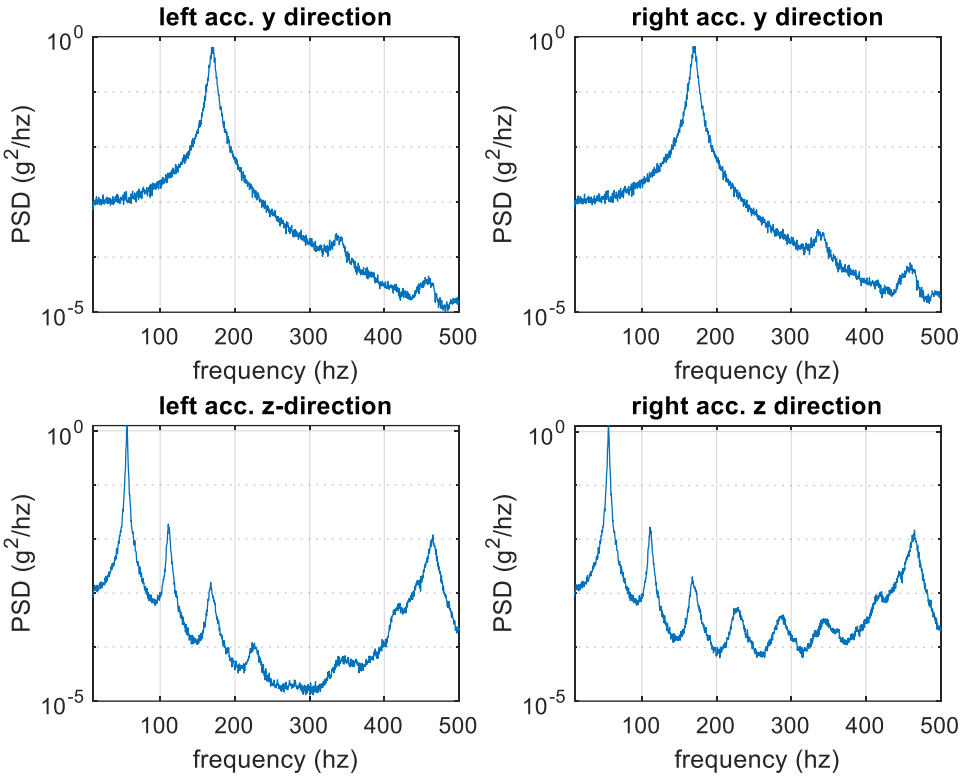

Figure 5.7 Acceleration PSDs for trimmed structure

After it is certain that the study will continue with these unwanted peaks, another test is performed to see whether these peaks are effective at the region where the failure is expected. To do that, another two accelerometers are attached to the brackets shown in Figure 5.8. Eventually, acceleration response PSDs in Figure 5.9 are showed that the hitting effect has no influence at the first bracket's critical location area.

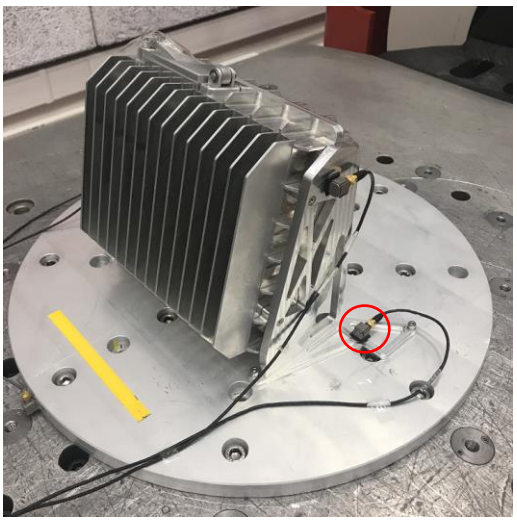

Figure 5.8 Lower left accelerometer's location

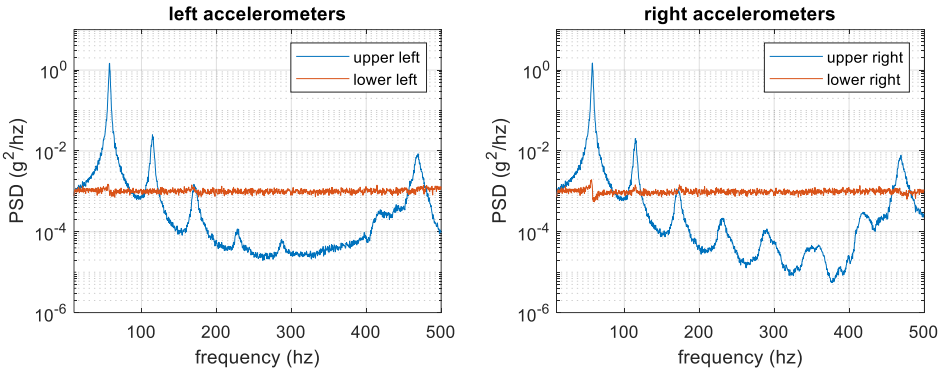

Figure 5.9 Comparisons of upper and lower accelerometers in the z direction

Up to this point, all tests were performed with an amplitude of 0.001 g^2/Hz white noise but eventually this system will be tested in real accelerated flight conditions and definitely the structure will be encountered high amplitudes. Therefore, it is important to know if the system behaves non-linear in high amplitude excitations or not. To do that, it is intended to increase the white noise input gradually and check the behavior of the structure. However, since the structure has that hitting effect explained above, instantaneous acceleration levels at the experiment exceeded the measuring range of accelerometers and no data could be collected above the amplitude of 0.0075 g^2/Hz white noise input. Obtained transmissibility plots at the first natural frequency location are given in Figure 5.10.

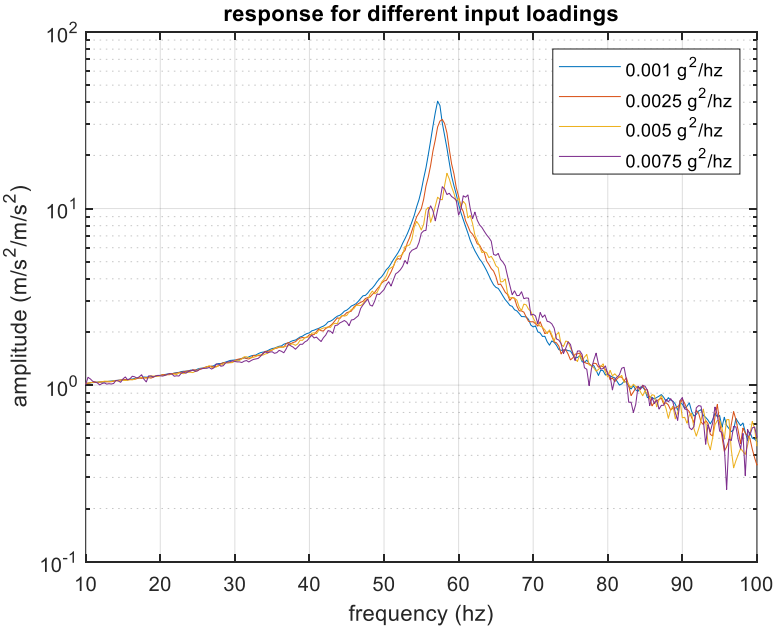

Figure 5.10 Checking non-linearity for different input loadings

From Figure 5.10, with increasing input loading it can be seen that the natural frequency of the system is not changing much with high amplitudes but the damping ratios are changing significantly. It is concluded that there is a damping type of non-linearity in the system. Damping non-linearity is not something desired because as it will be explained in the further chapters, fatigue life is strongly dependent on the damping of the system. Handling damping ratio non-linearity will be covered in further sections.

Table 5.3 Damping ratios for different loadings in first natural frequency

Loading amplitude $\left(\frac{g^2}{hz}\right)$	**Damping ratio**
0.001	0.012
0.0025	0.017
0.005	0.019
0.0075	0.024

5.2. Finite Element Based Verification Analysis

5.2.1. Modal Analysis

After the structure has meshed and contacts are defined, modal analysis is performed. Since the modal analysis will provide input for further analysis such as harmonic and random analysis, the number of modes to be calculated is important. Because the number of modes to be calculated changes the value of the ratio of effective mass to total mass which gives information about the significance of modes in the dynamic behavior of the structure and it is suggested to be not less than 80% in all directions. Sometimes even the number of modes is increased, this fraction may not change much and in that case, it is suggested to take 1.5 times the interested maximum frequency.

Since the interest is up to 2000 Hz, 90 modes of the structure are found up to 3089.7 Hz and the corresponding effective mass to total mass ratios are given in Table 5.4.

Table 5.4 The ratio of effective mass to the total mass in each direction

X direction: 86%	rotX direction: 79%
Y direction: 88%	rotY direction: 93%
Z direction: 87%	rotZ direction: 87%

Table 5.5 Natural frequencies of the structure up to 90 modes

Mode	Frequency (Hz)	Mode	Frequency (Hz)	Mode	Frequency (Hz)
1	57.311	31	1528.8	61	2240.1
2	174.98	32	1534.7	62	2263.7
3	465.98	33	1539.1	63	2280.9
4	662.67	34	1553.8	64	2294.2
5	733.36	35	1568.4	65	2337.8
6	839.62	36	1623.2	66	2341.8
7	975.14	37	1666.4	67	2342.5
8	1275.8	38	1786.5	68	2346.5
9	1293.2	39	1796.4	69	2360
10	1353.1	40	1821.6	70	2379.4
11	1381.7	41	1827.1	71	2430.5
12	1389.2	42	1833.9	72	2455.7
13	1403.9	43	1855.9	73	2482.4
14	1413	44	1866.4	74	2495.5
15	1414.2	45	1915.4	75	2545.5
16	1420.8	46	1928.1	76	2566.8
17	1430.5	47	1957	77	2580.2
18	1432.1	48	1990.2	78	2759.8
19	1442.4	49	1996.2	79	2798.6
20	1457.9	50	2005.2	80	2837.4
21	1473.9	51	2032.3	81	2863.9
22	1475.6	52	2056.1	82	2916.1
23	1479.7	53	2097.6	83	2937.1
24	1484.8	54	2129.8	84	2955.9
25	1487.4	55	2163.9	85	2965.8
26	1489.7	56	2175.5	86	2985.1
27	1490.8	57	2190.9	87	3001.8
28	1500.5	58	2195.7	88	3009.4
29	1510.3	59	2209.2	89	3019.8
30	1519.3	60	2238	90	3089.7

Among these natural frequencies given in Table 5.5, the first three of them are mainly related to the brackets. The mode shapes of them are given in Figure 5.11.

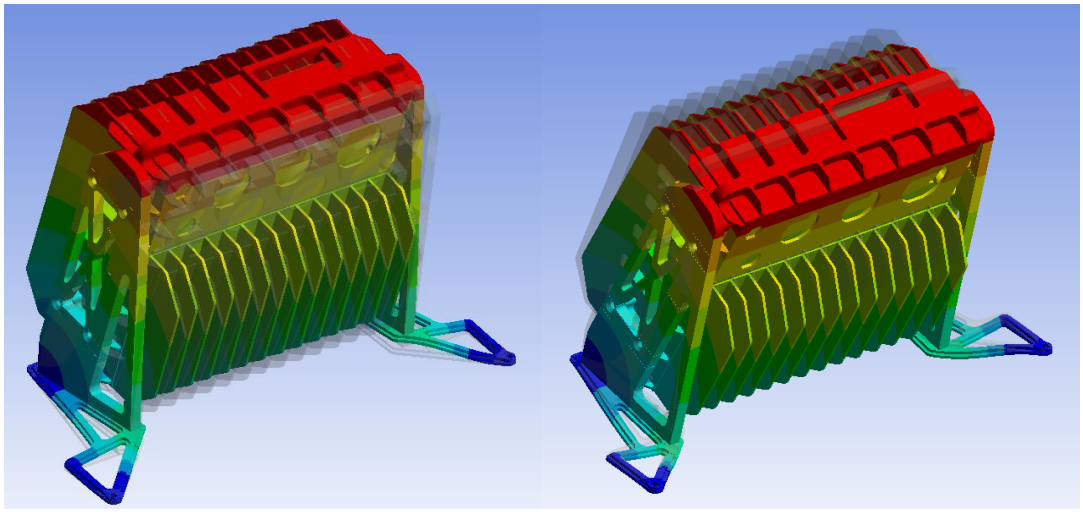

1st mode 57.3 Hz

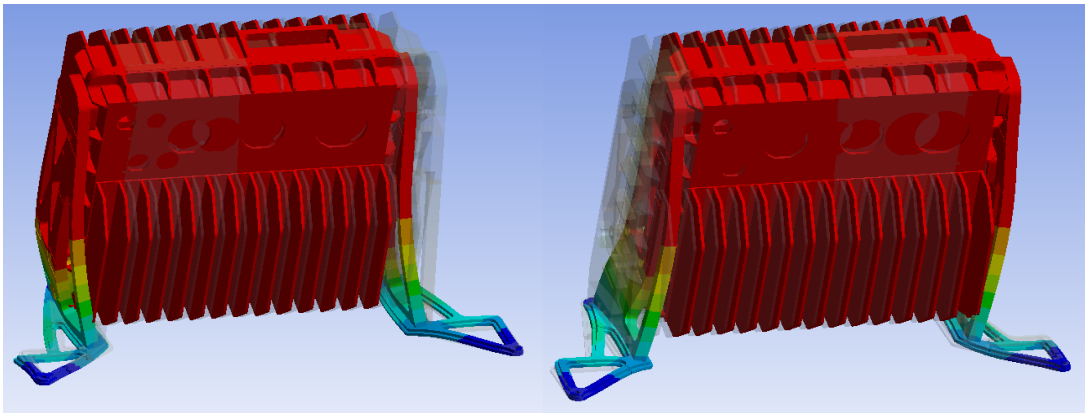

2nd mode 174.98 Hz

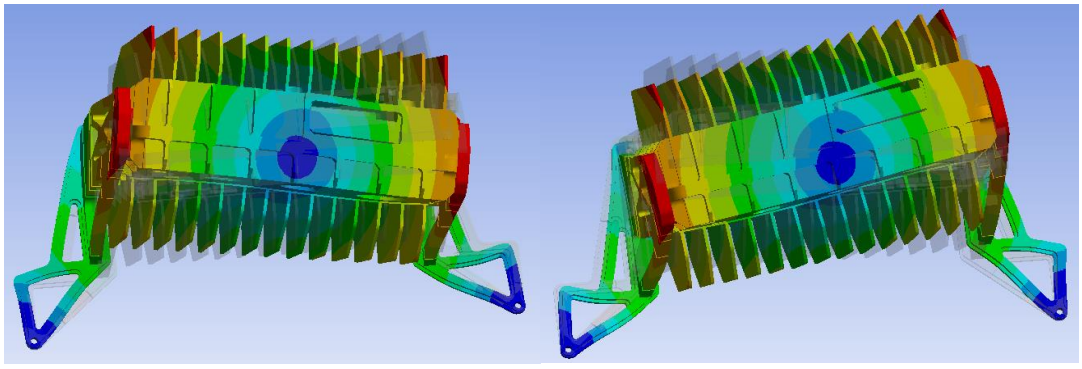

3rd mode 465.98 Hz

Figure 5.11 First three mode shapes of brackets

5.2.2. Harmonic Response Analysis

In order to obtain the acceleration transmissibilities at the location of the accelerometers shown in Figure 5.2, a Harmonic Response Analysis with unit g acceleration base excitation is applied to the system in the y and z-directions separately.

The frequency range is set up to 2000 Hz and user defined frequency steps are applied in tabular form. Normally ANSYS offers three way to apply the frequency steps.

The first method is dividing the frequency range into equally spaced points. This method most probably will be insufficient in terms of capturing the peaks unless the frequency steps are chosen too small. But if the frequency steps are chosen small enough, this will cause a very long analysis time and large file sizes.

The second and most recommended method is the Cluster method. When the cluster method is used, the solution is calculated on each natural frequency location with more resolution to accurately capture the peaks. But in that case, since there are 49 modes in total up to 2000 Hz, clustering all 49 modes may cause very large file sizes. In fact, it is not necessary to have more resolution on peaks after a certain number of modes because the amplitude of response gets smaller and smaller. That is why user defined frequency steps are used.

For the first three resonance location, which are the most important frequencies for the brackets, frequency resolution set to be equal with the case where the cluster number is set to be 20. The other frequency intervals are set to be reasonable values to capture the peaks for the other resonance locations so that both the peaks can be captured accurately, file sizes and analysis time are decreased.

Another important parameter is defining the damping ratio of the system. In analysis settings, the damping ratio can only be entered as a single value and this value is applied to the whole frequency range. But in the real case, each natural frequency location has its own damping characteristics. To do that in ANSYS, an APDL command called MDAMP is used to define the damping ratios as a function of mode. The first three modes entered

according to the measured experimental results given in Table 5.2. All modes except the first three ones entered as 0.02.

After defining the frequency steps and damping ratios, transmissibilities are obtained at the location of the accelerometers. Results are shown in Figure 5.12.

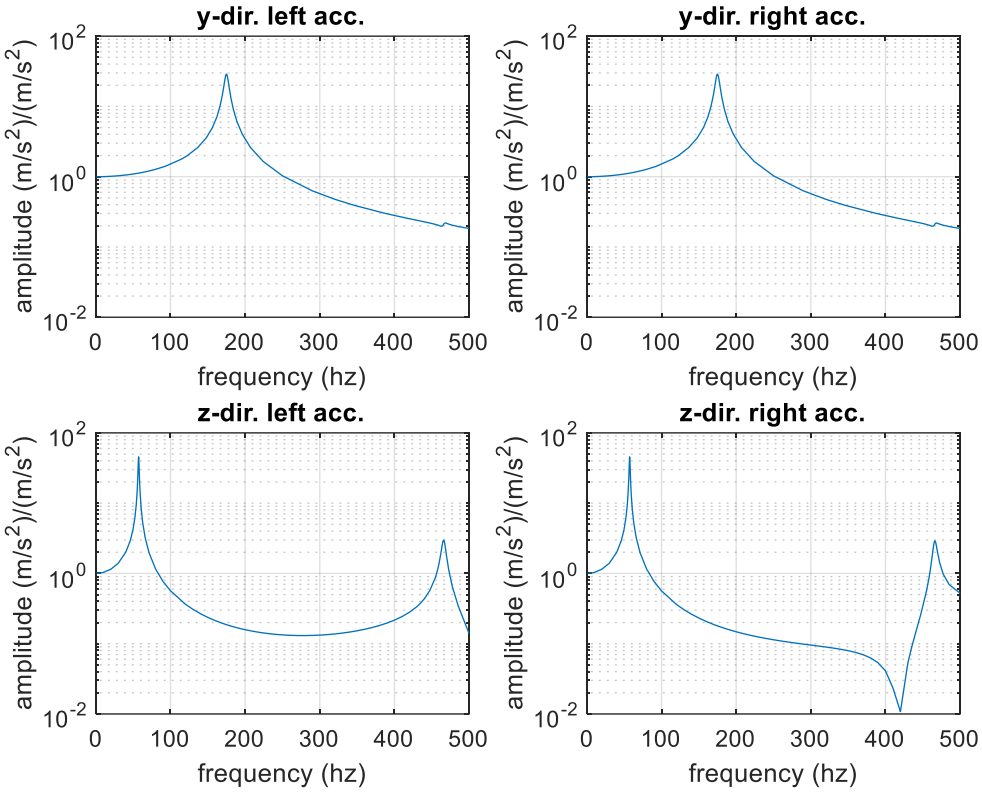

Figure 5.12 Transmissibilities in y and z directions in left and right accelerometers in ANSYS

5.2.3. Random Vibration Analysis

Another comparison parameter is the acceleration PSDs at the accelerometer location. Therefore, an amplitude of 0.001 g^2/Hz white noise base excitation input is applied to the system in y-direction and z-direction separately in Ansys Random Vibration. As it is stated before, frequency dependent damping ratios are applied with the MDAMP command with the values shown in Table 5.2. Obtained acceleration PSDs at the accelerometer locations are shown in Figure 5.13.

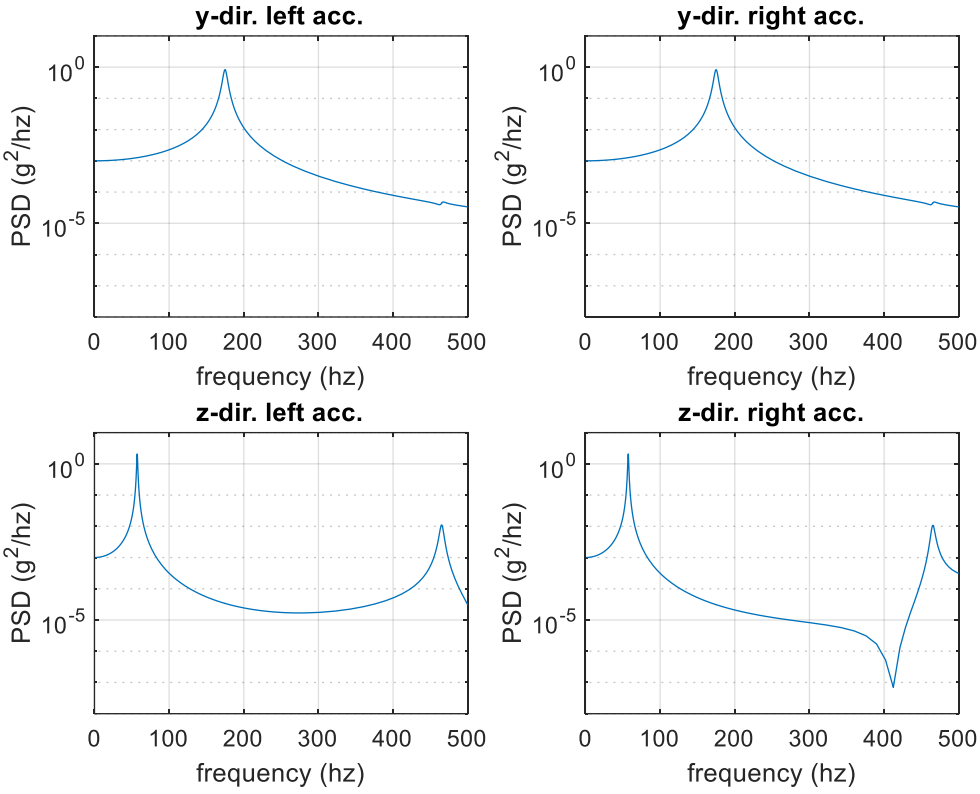

Figure 5.13 Acceleration PSDs in y and z directions in left and right accelerometers in ANSYS

5.3. Comparison of Verification Analysis Results

Natural frequencies obtained from experiments and finite element modal analysis are given in Table 5.6. In the comparison table, it can be concluded that the first three natural frequencies obtained from experiments and finite element analysis are very close to each other.

Table 5.6 Natural frequencies comparison

Mode number	Nat. Freq (Hz) Experiments	Nat. Freq (Hz) Analysis
1	56.88	57.31
2	175.31	174.98
3	474.69	465.98

After concluding that the modes are close enough to each other, acceleration transmissibilities and acceleration PSDs are compared in Figure 5.14 and Figure 5.15.

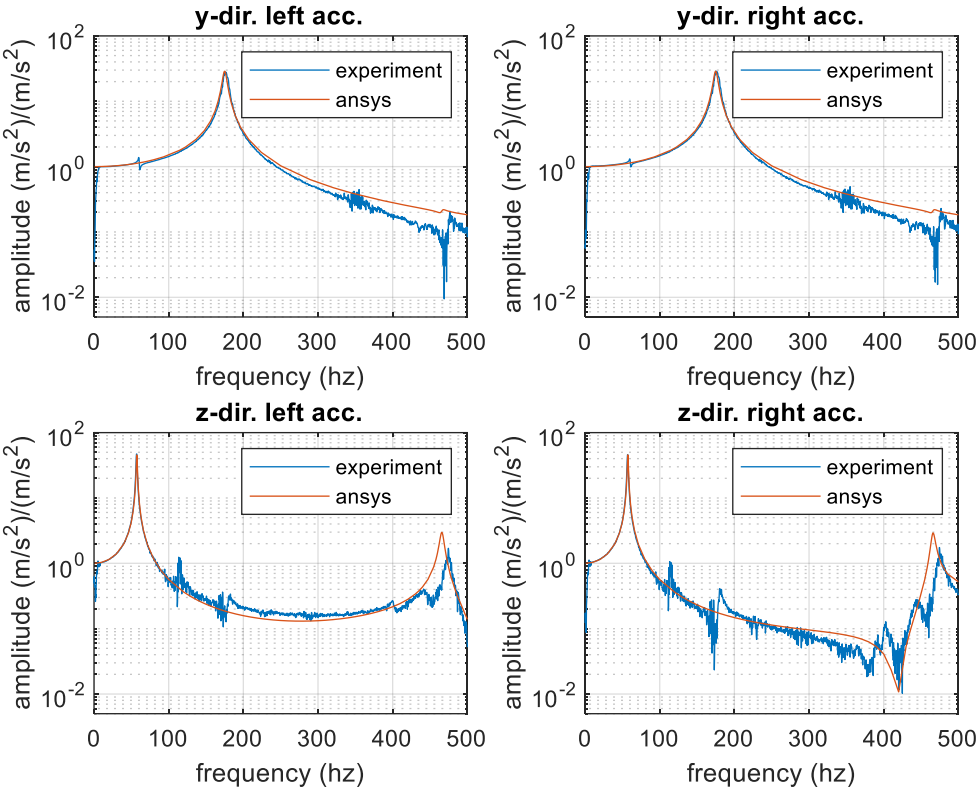

Figure 5.14 Acceleration transmissibility comparison of experiment and FEM analysis

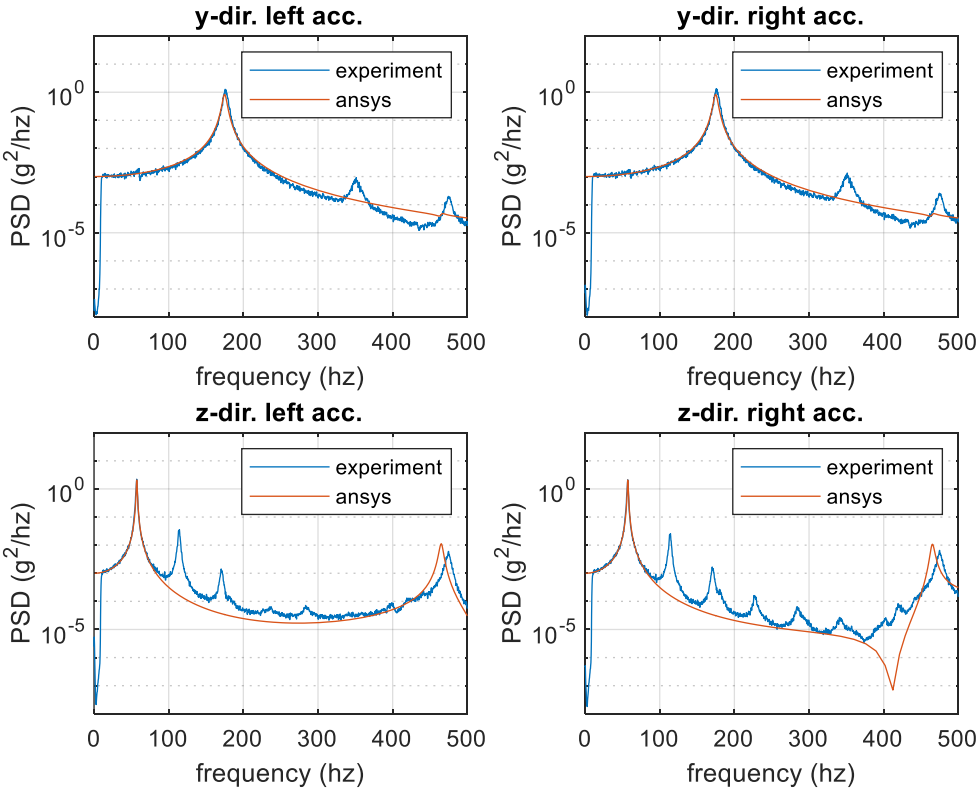

Figure 5.15 Acceleration PSD comparison of experiment and fem analysis

As it is stated in Chapter 5.1, undesired peaks are occurred in the experiments but it is concluded that these peaks are not effective in the possible failure locations of the brackets. That is why, while comparing the verification analysis results, these peaks are ignored.

In Figure 5.14, when the y-direction left and right accelerometers results are examined, the second natural frequency and its damping are accurately captured from the analysis program. At the same graph, the first natural frequency can be identified in the experiments with a small peak but it does not appear in the analysis. This is because even the loading is applied in the y-direction, the shaker excites the system in very small amplitudes in other directions as well. However, in the analysis program excitation is in the pure y-direction and so that the peak at the first natural frequency is not seen.

When the z-direction left and right accelerometers results are examined in Figure 5.14, it can be seen that the first natural frequency and its damping are accurately captured in the analysis results. As mentioned before, although the loading is in z-direction in the experiment, there are also small amplitude excitations in other directions. Therefore, the second natural frequency has made a small peak around 175 Hz in the experimental data. However, this peak interferes with the peaks caused by the impacts of internal parts. As expected, at the second natural frequency there is no such effect on the analysis result. At the third natural frequency location, there is a shift around 9 Hz due to the difference in experiment and analysis results. However, in general, the third natural frequency location captured accurate enough in the analysis program.

From the experimental and finite element verification analysis, it is concluded that the analysis model is a true representation of the real structure. Even the system has many uncertainties and/or non-linearity, the analysis model can be considered correct for such geometry.

6. FLIGHT DATA ACQUSITION AND MISSION SYNTHESIS

To be able to represent the real flight conditions an operational flight test is performed. At all flight phases, which are actually the maneuvers that the aircraft performs during an ordinary mission, acceleration levels are obtained with accelerometers attached to the platform. For confidential issues, flight phases durations are not given, calculated loading PSDs are scaled and plotted without values.

Table 6.1 Operational Flight Test Phases and Durations

PHASE NO	**FLIGHT PHASE**	**DURATION (hours)**	**DURATION WHOLE LIFE (hours)**
1	Idle Ground	t_1	$T_1 = T_{tot} * \left(\frac{t_1}{t_{tot}}\right)$
2	Ground RPM Raise	t_2	$T_2 = T_{tot} * \left(\frac{t_2}{t_{tot}}\right)$
3	Ground System Speed	t_3	$T_3 = T_{tot} * \left(\frac{t_3}{t_{tot}}\right)$
4	Take off and Climbing	t_4	$T_4 = T_{tot} * \left(\frac{t_4}{t_{tot}}\right)$
5	Low Altitude Hover	t_5	$T_5 = T_{tot} * \left(\frac{t_5}{t_{tot}}\right)$
6	Forward Flight and Climbing	t_6	$T_6 = T_{tot} * \left(\frac{t_6}{t_{tot}}\right)$
7	Level Flight	t_7	$T_7 = T_{tot} * \left(\frac{t_7}{t_{tot}}\right)$
8	Hover	t_8	$T_8 = T_{tot} * \left(\frac{t_8}{t_{tot}}\right)$
9	Forward Flight and Descend	t_9	$T_9 = T_{tot} * \left(\frac{t_9}{t_{tot}}\right)$
10	Deceleration and Descend	t_{10}	$T_{10} = T_{tot} * \left(\frac{t_{10}}{t_{tot}}\right)$
11	Landing	t_{11}	$T_{11} = T_{tot} * \left(\frac{t_{11}}{t_{tot}}\right)$
	Total Flight Duration	$t_{tot} = \sum_{i=1}^{11} t_i$	$T_{tot} = 2500$

Table 6.1 summarizes the operational flight test phases. In each phase, acceleration versus time data is obtained in around 4 to 5 minutes of duration in order to get sufficient averages in the FFT procedure.

Acceleration versus time data of each phase is first converted into individual acceleration PSD data by using pwelch function in Matlab, which uses Welch's power spectral density estimates. The frequency resolution of PSD data is set to 0.244 Hz. Since the sampling frequency of time data is 8000 Hz, PSD is obtained up to 4000 Hz due to the Nyquist theorem. But all analyzes are carried out up to 2000 Hz since the data does not include high amplitudes beyond 2000 Hz and it is recommended to analyze up to 2000 Hz in aircraft structures according to MIL-STD-810G.

Normally in a single ordinary operational flight of the air vehicle, each phase should last for a certain duration. It is given with t_i where i corresponding to each phase and the duration of the phases corresponds to whole operational life is given with T_i. According to MIL-STD-810G, 2500 hours of flight duration is sufficient to simulate the total time the air vehicle will fly during its lifetime. That is why T_{tot} is assumed to be 2500 hours.

Therefore, the operational flight data obtained from the platform of each phase can be combined to obtain a single PSD data with the help of the theory explained in Chapter 3.4 and the equation given below,

$$T_{tot}{G_{tot}}^{m/2} = {T_1{G_1}^{m/2} + T_2{G_2}^{m/2} + \cdots + T_N{G_N}^{m/2}} \tag{6.1}$$

Where $T_{1,2,N}$ is the time durations of each phase given in Table 6.1, $G_{1,2,N}$ is the PSD value of each phase and m is the exponent explained in Chapter 3.4. For the obtained flight data with $m = 7.5$ assumption, acceleration PSDs of each axis for 2500 hours are given in Figure 6.1.

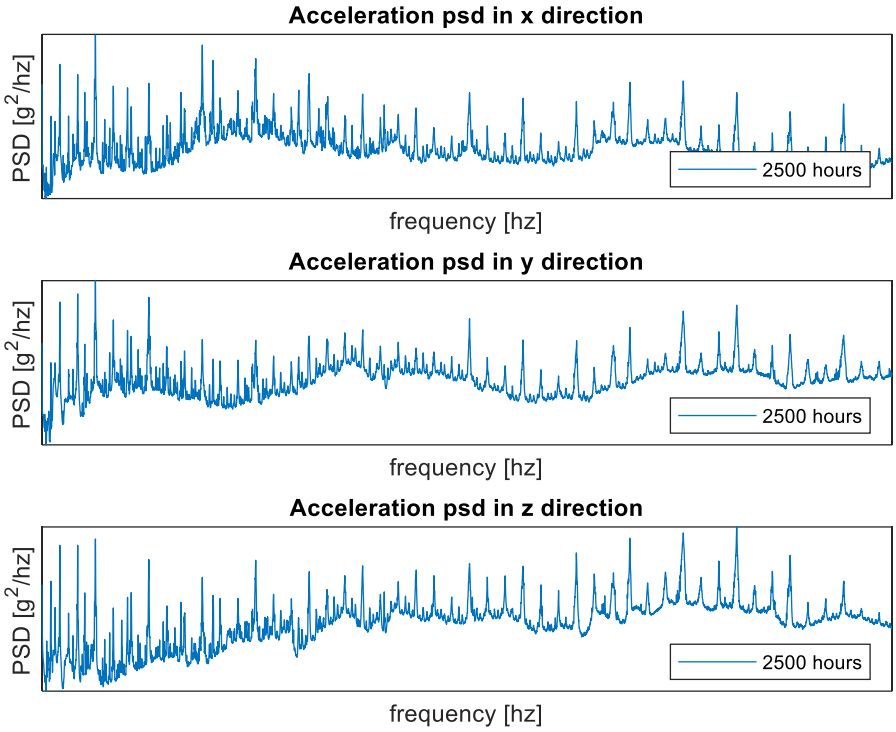

Figure 6.1 Acceleration PSDs of each axis for 2500 hours

Normally in multiaxial loading conditions, the multiaxial theory has to be applied. But for this study, since the experimental shaker infrastructure does not provide multiaxial loading simultaneously, all analysis will be performed with single axis acceleration PSD input to be able to verify the analysis with experiments. To do a reasonable assumption, an enveloping method is used. Maximum value at each frequency of each direction is used to obtain a single axis acceleration PSD. From the previous analysis of the structure in different directions, it is concluded that the weakest direction is the z-direction and the enveloped data will be performed in z-direction in future analysis.

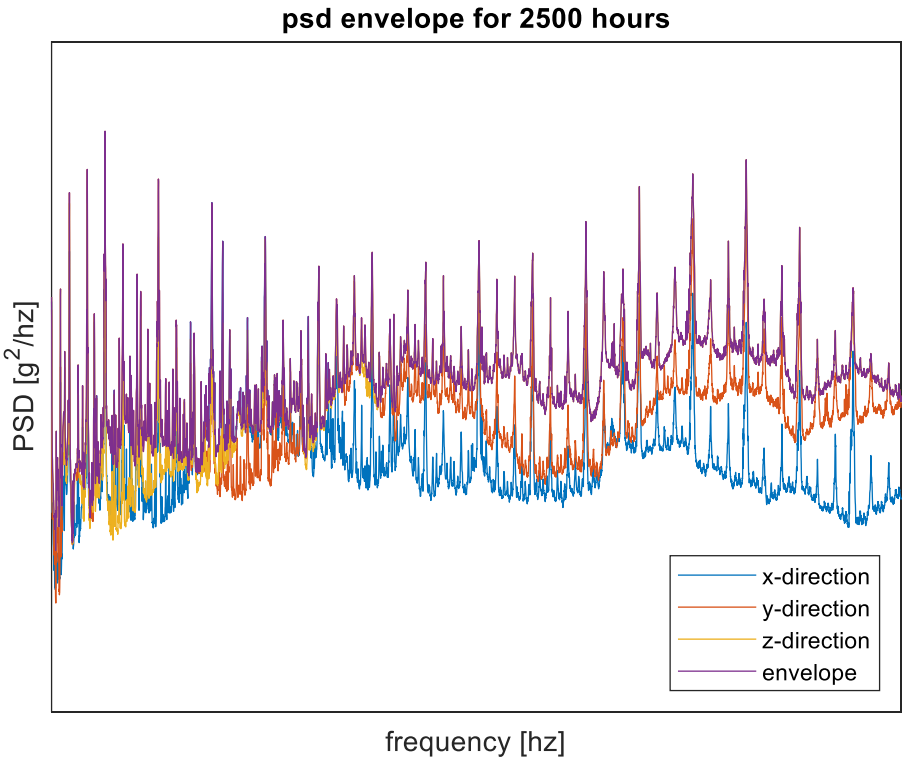

Figure 6.2 PSD envelope for 2500 hours

2500 hours of duration represent the whole lifetime of the platform and it can be used to analyze the structures life in the FEM environment. However, it is not possible to perform an experimental fatigue analysis with 2500 hours of data. For this reason, 2500 hours of data accelerated to 4 hours with keeping equal damage values to be created at the end of the duration. To do that same equation is used as follows,

$$T_4 {G_4}^{m/2} = T_{2500} {G_{2500}}^{m/2} \tag{6.2}$$

Here, G_4 is the desired 4 hours PSD, G_{2500} is the enveloped 2500 hours PSD, T_{2500} is 2500 hours, T_4 is 4 hours and m is the scaling factor. The value of m is taken as 11.3 instead of 7.5, which is the recommended value in the standard. Here, m constant decided according to the Dirlik method's damage value of the critical nodes at the end of the total duration of 2500 hours and 4 hours. Further information on m constant and its effect on accelerating life testing is given in the Chapter 8.1.

Obtained 2500 hours and 4 hours PSDs are given in the Figure 6.3 and gRMS values of each data are given in the Table 6.2.

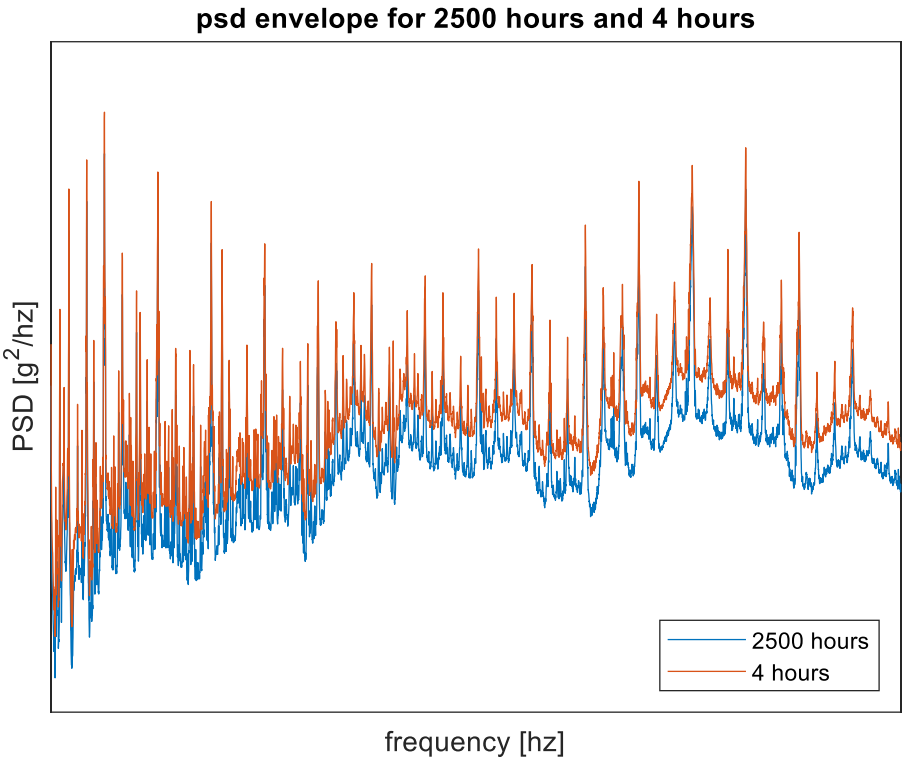

Figure 6.3 PSD enveloped data comparison for 2500 hours and 4 hours

Table 6.2 gRMS values comparison of each direction and enveloped data

Loading	gRMS value
x-direction (2500 hours)	1.2343
y-direction (2500 hours)	2.5866
z-direction (2500 hours)	3.4606
Envelope (2500 hours)	3.9636
Envelope (4 hours)	7.0072

7. FATIGUE LIFE OF BRACKETS AND ACCELERATED LIFE TESTING

In the previous chapters, the finite element model of the structure is verified and the real flight data is converted into acceleration PSD functions, which will be used for input loading to the system. Hereby, all information is acquired to continue the fatigue calculations.

In this chapter, the fatigue life of the structure is obtained from developed Matlab code and from commercial fatigue software Ncode Design Life. Results of both analyses are compared to verify the developed code for further analysis. Lastly, by using the accelerated life testing theory, flight data is accelerated and experimental fatigue tests are performed.

As shown in Figure 7.1, fatigue life calculation methodologies of developed numerical code and commercial software are quite similar to each other. After importing the geometry to ANSYS Workbench and creating the finite element model, stress history is obtained from ANSYS. Both analysis types are using ANSYS to get the stress transfer function. After performing Harmonic Response Analysis, Ncode directly imports the ANSYS data to its own database and calculates the transfer function from its own algorithm. For Matlab code, principal stresses are obtained from ANSYS Classic and imported to Matlab to calculate the transfer function. The next steps in Figure 7.1 are identical in terms of theory but Ncode software calculates these steps with its own code, on the other hand, the Matlab code is constructed by the author.

According to the finite element model of the structure, two critical nodes of the part appear which are node number 19067 and node number 791796. In this chapter, all calculations and sub-steps are given in detail for one of the critical nodes, 19067. For the second critical node, only the results will be given.

In this chapter, due to confidential issues, figures related to flight data are given in a scaled form and without values. However, all results have been obtained using real data.

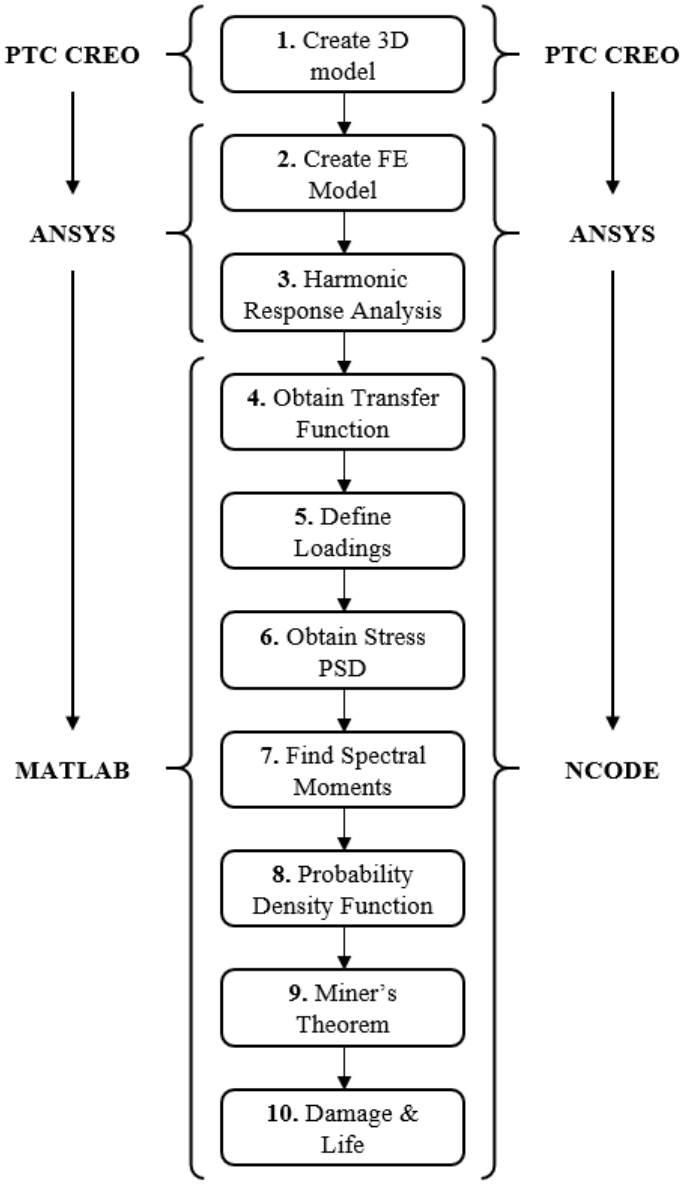

Figure 7.1 Fatigue life calculation methodology for Matlab Code and Ncode

7.1. Life of the Brackets from Matlab Code

The 3D model is imported to ANSYS and material properties, boundary conditions and meshing are defined as it is stated in Chapter 4.

As it is stated before, the transfer function at the most critical location is needed. To achieve this data, a unit g acceleration base excitation input is applied in ANSYS Harmonic Response analysis and principal stresses at the critical location are saved to a file and imported to Matlab.

In order to obtain the transfer function from the principal stresses, the true stress combination method has to be decided. Since there is single axis loading, equivalent stress-strain theories are suitable for such case and one of the most used and accepted methods in the literature, absolute maximum principal stress theory is selected for the stress combination method. The stress transfer function obtained with absolute maximum principal stress theory is given in Figure 7.2.

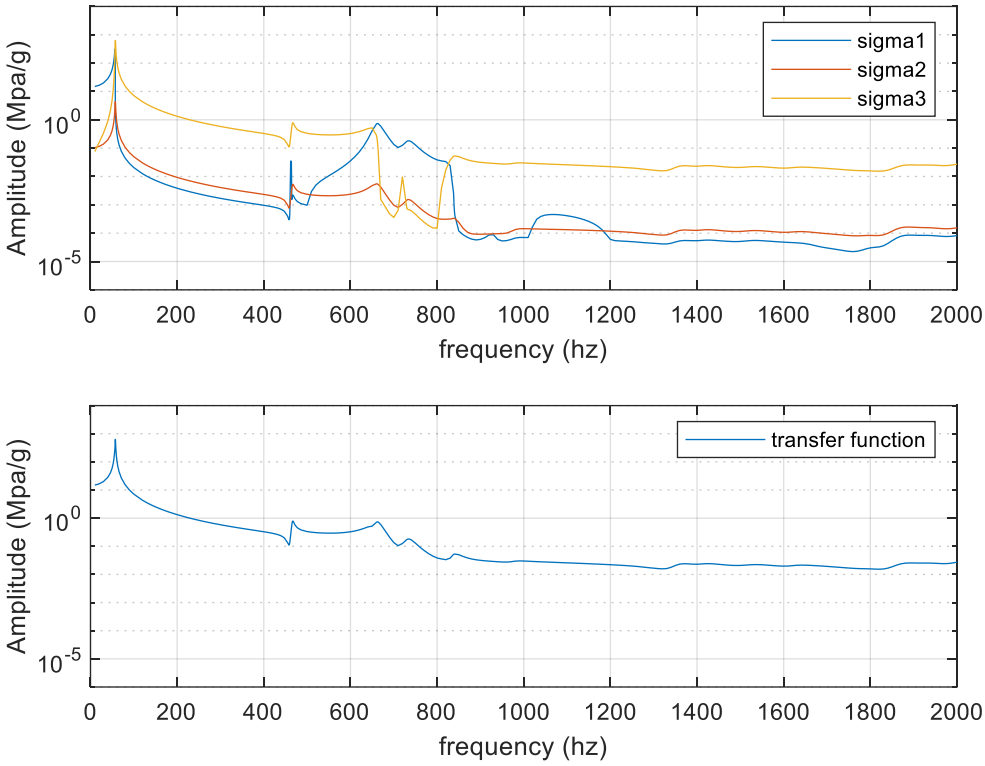

Figure 7.2 Transfer function obtained with absolute maximum principal theory for node id 19067

After obtaining the stress transfer function, according to the methodology given in Figure 7.1, input loading has to be defined. Operational flight data for 2500 hours duration is used for analysis and it is given in Figure 7.3.

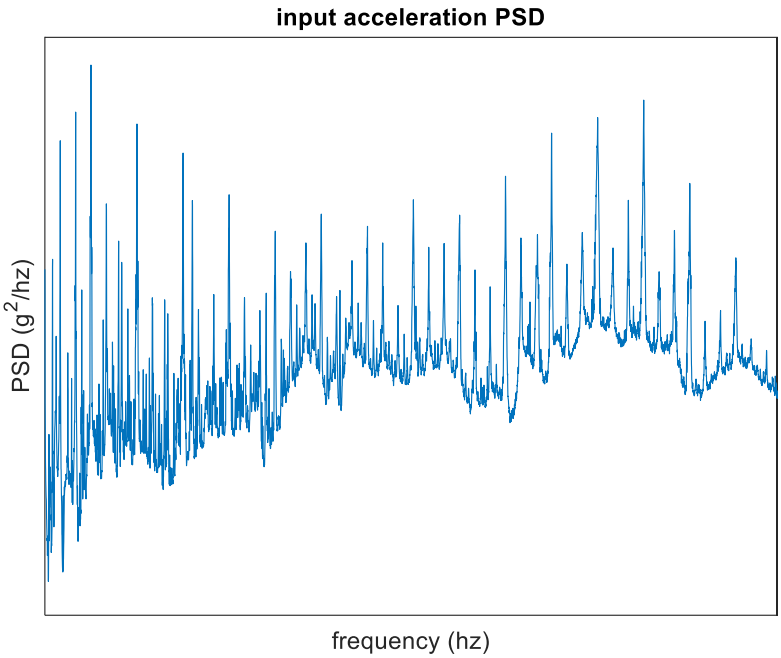

Figure 7.3 Operational flight data for 2500 hours

Now, all the information is acquired to obtain stress PSD at the critical location. According to equation (3.19), response stress PSD shown in Figure 7.4 is calculated by using obtained transfer function and input PSD loading.

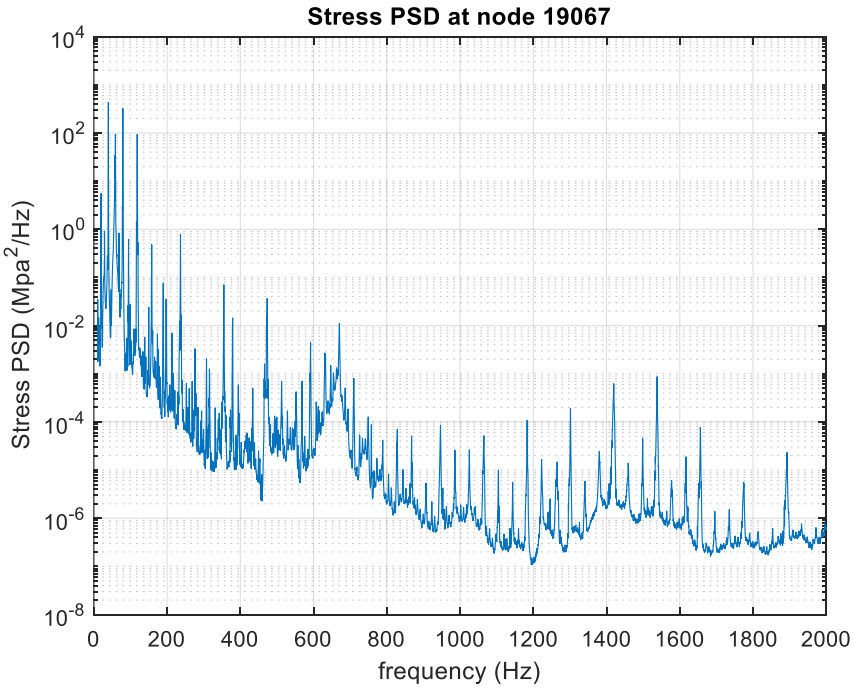

Figure 7.4 Stress PSD at node 19067

After obtaining stress PSD, the next step is to find the spectral moments of stress PSD. By using the equation (3.22), spectral moments are calculated and tabulated in Table 7.1.

Table 7.1 Spectral Moments of Stress PSD at node 19067

	Numerical Code
$\boldsymbol{m_0}$	456.7806
$\boldsymbol{m_1}$	2.9809e+04
$\boldsymbol{m_2}$	2.3254e+06
$\boldsymbol{m_4}$	6.0392e+10

According to the spectral moments of stress PSD, some important parameters of the signal such as RMS value, number of upward zero crossings per second $E[0]$, number of peaks per second $E[P]$ and the irregularity factor γ are given in Table 7.2.

Table 7.2 Stress history parameters obtained from spectral moments

$\boldsymbol{RMS}$	21.37 Mpa
$\boldsymbol{E[0]}$	71.35
$\boldsymbol{E[P]}$	161.15
$\boldsymbol{\gamma}$	0.44

By using calculated spectral moments, the probability density function of rainflow ranges obtained from the stress PSD function is determined according to Dirlik, Lalanne and Narrow Band methods. In Figure 7.5, PDF stress ranges obtained from the Dirlik method is given.

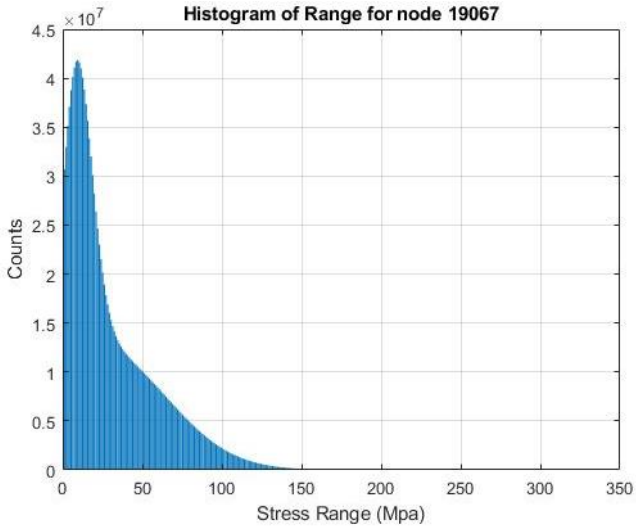

Figure 7.5 PDF obtained from Dirlik method for node 19067

The next step is to use Miner's theorem to obtain the damage at the desired location. To do that the Probability Density Function of rainflow ranges and the S-N curve of Aluminum 7075-T6 are used. At this stage, it is important to remark that while dividing the cycles obtained from PDF of rainflow ranges to cycles obtained from S-N curves to get the damage with Miner's Theorem, stress levels of nominator and denominator must be in the same type. For instance, in Figure 7.5, stress levels are in terms of stress range. However, used S-N curve for this analysis given in Figure 7.6 is in terms of alternating stress. In this study, while performing Miner's theorem, in order not to make any mistake, stress levels of the S-N curve are converted to stress ranges and after that damage is calculated.

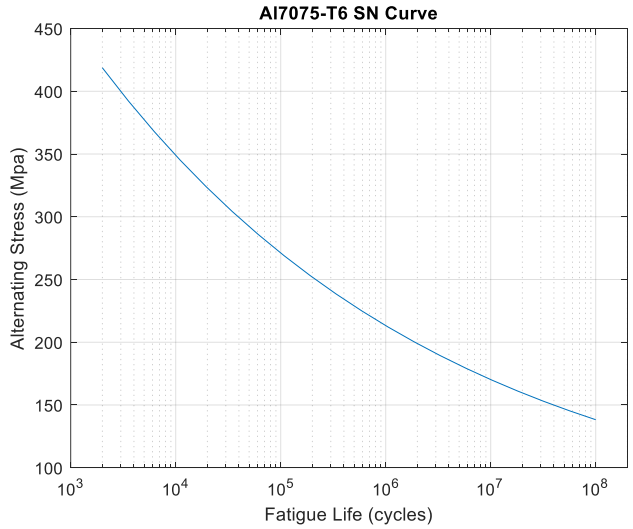

Figure 7.6 S-N Curve of Al 7075-T6

Another important notice, in the Miner's theorem given in equation(3.33), the upper limit of integral must be defined. In this analysis, the upper limit is defined to be the maximum alternating stress of the S-N curve, which is 418 Mpa.

According to the results, the damage histogram is obtained as given in Figure 7.7. From the damage histogram, it is seen that the 200 Mpa alternating stress or in other words 400 Mpa stress range could be chosen for the upper limit of integral since there is not any damage occurs after that value.

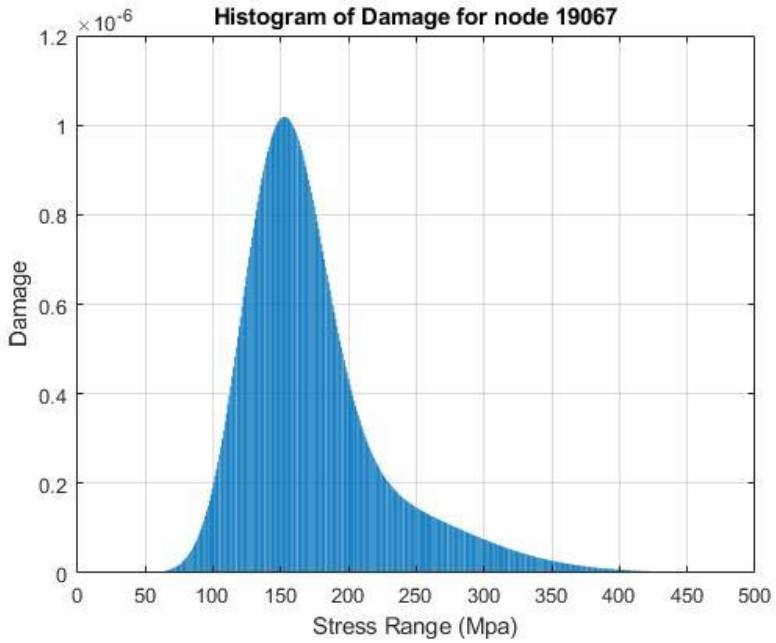

Figure 7.7 Damage Histogram of node 19067

Finally, accumulated damage is found at the end of 2500 hours from Dirlik, Lalanne and Narrow Band methods. Afterwards, the life of the structure is found by dividing the total duration by the obtained damage values. All results for two critical nodes are given in Table 7.3.

Table 7.3 Damage and Life of the structure according to Dirlik, Lalanne and Narrow Band methods

Node id	PSD Cycle Counting Method	Damage	Life (s)
19067	Dirlik	9.0807e-05	9.9112e+10
	Lalanne	7.7519e-05	1.1610e+11
	Narrow Band	1.7271e-04	5.2112e+10
791796	Dirlik	8.2293e-05	1.0937e+11
	Lalanne	7.1800e-05	1.2535e+11
	Narrow Band	1.5419e-04	5.8369e+11

7.2. Life of the Brackets from Ncode Design Life

Fatigue life calculation methodology and theory behind the calculations for Ncode is exactly the same as the numerical code given in the previous chapter. The prerequisite of Ncode software to get the fatigue solution is to choose the materials from Ncode library, which is already defined in the Engineering Data and to connect the Harmonic Response Analysis that contains the stress transfer function information to the Ncode.

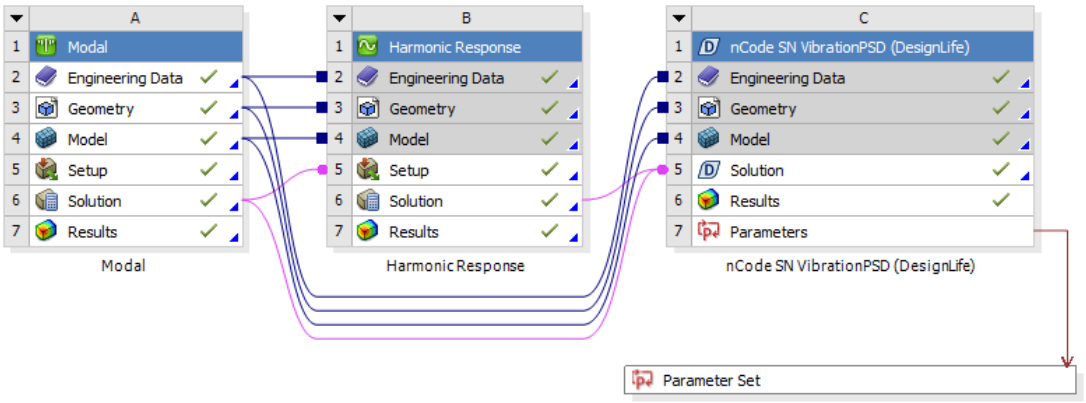

Figure 7.8 ANSYS Workbench – Ncode analysis construction

All other arrangements such as defining input loading and its duration, choosing the stress combination methods, choosing the PSD rainflow cycle counting methods such as Dirlik, Lalanne or Narrow Band etc. are made inside the Ncode solver.

Before starting the analysis, one important arrangement is done to reduce to solution time. Ncode calculates the fatigue life of all nodal points on the entire geometry and it is unnecessary if the critical location is already known. That is why the critical location is selected with named selection command in Ansys Harmonic Analysis so that these named selections became electable in Ncode and solution is obtained only at these selections as shown in Figure 7.9.

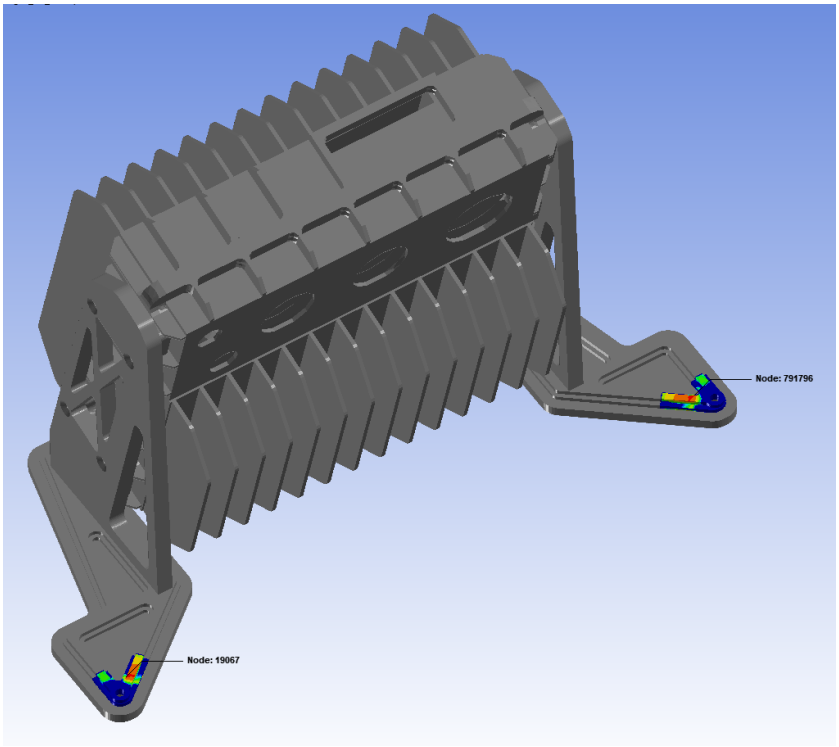

Figure 7.9 Node 19067 and 791796 in Ncode

Next, operational flight data is imported from an excel file to the Vibration Generator glyph and the duration of loading is entered to be 2500 hours. The absolute maximum principal method is chosen for the combination method. Dirlik, Lalanne and Narrow Band counting methods are selected respectively and the model is solved for each case. Stress response PSD obtained from Ncode is given in Figure 7.10 and the spectral moments calculated from that stress PSD is given in Table 7.4.

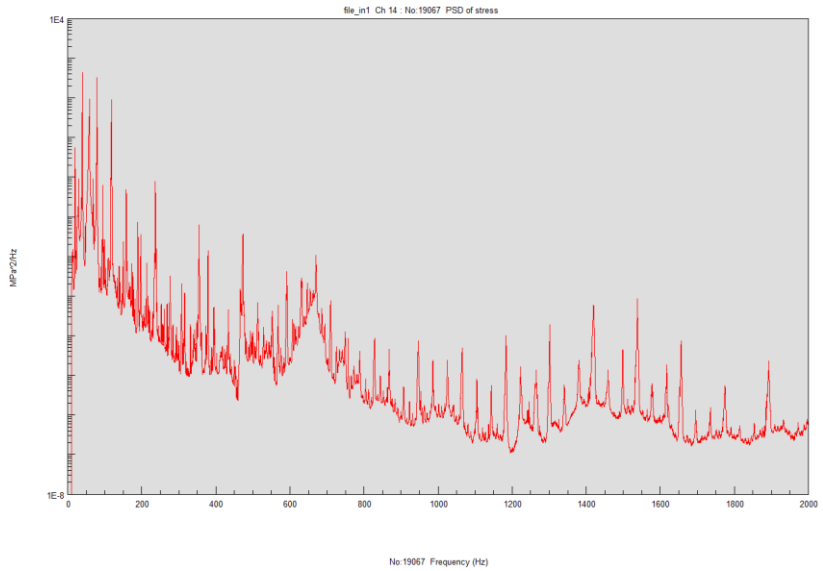

Figure 7.10 Stress PSD obtained from Ncode at node 19067

Table 7.4 Spectral Moments of Stress PSD at node 19067 in Ncode

	NCode
$\boldsymbol{m_0}$	475.4118
$\boldsymbol{m_1}$	3.1001e+04
$\boldsymbol{m_2}$	2.3540e+06
$\boldsymbol{m_4}$	2.0320e+10

RMS value, number of upward zero crossings per second $E[0]$, number of peaks per second $E[P]$ and the irregularity factor γ calculated in Ncode are given in Table 7.5.

Table 7.5 Stress history parameters obtained from Ncode

$\boldsymbol{RMS}$	21.80 Mpa
$\boldsymbol{E[0]}$	70.37
$\boldsymbol{E[P]}$	93.26
$\boldsymbol{\gamma}$	0.75

According to Dirlik's method, the Probability Density function cycle histogram obtained from Ncode is given in Figure 7.11 and the S-N curve of Aluminum 7075-T6 defined from Ncode library is given in Figure 7.12.

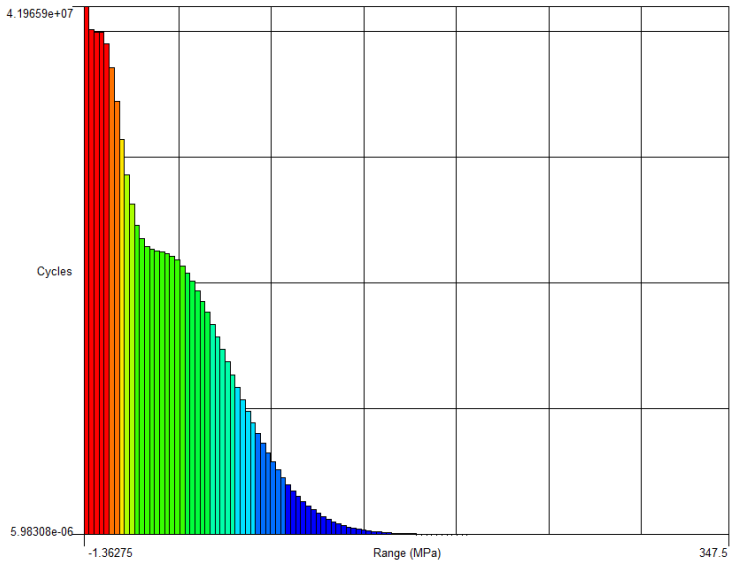

Figure 7.11 PDF obtained from Dirlik method for node 19067 in Ncode

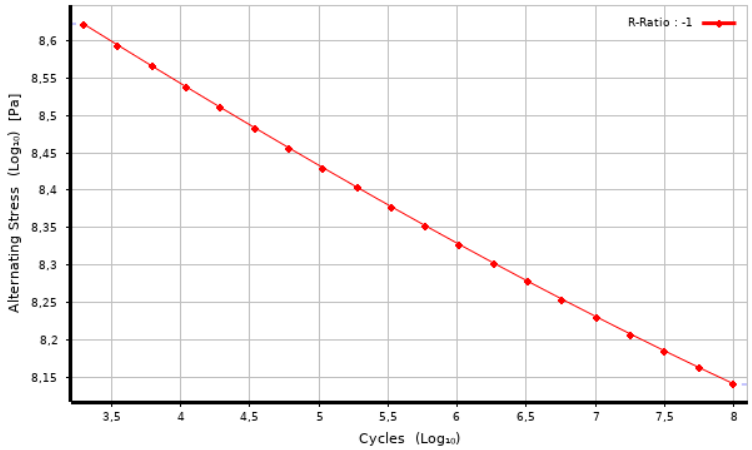

Figure 7.12 S-N Curve of Al7075-T6 from Ncode Material Library

From the results of Ncode, the calculated damage histogram from Dirlik's method is given in Figure 7.13.

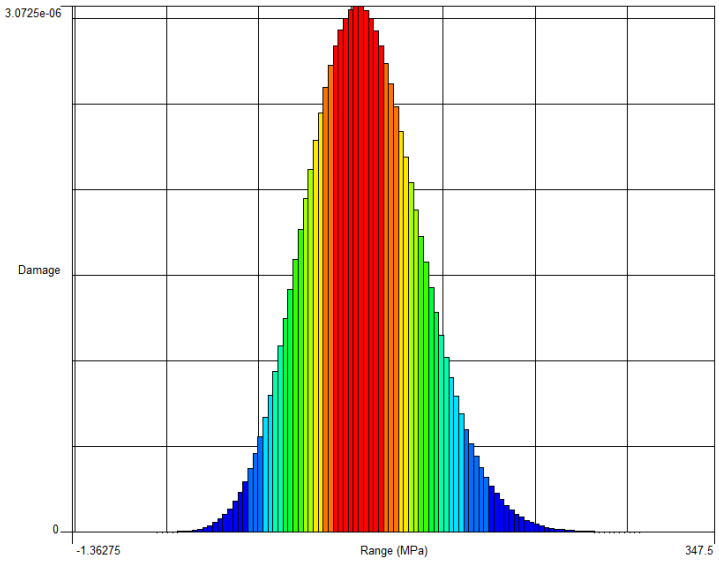

Figure 7.13 Damage Histogram of node 19067 in Ncode

Obtained damage and life values by using Dirlik, Lalanne and Narrow Band methods for two critical locations of the structure according to 2500 hours duration flight data are given in Table 7.6.

Table 7.6 Damage and Life of the structure according to Dirlik, Lalanne and Narrow Band methods obtained from Ncode

Node id	**PSD Cycle Counting Method**	**Damage**	**Life (s)**
19067	Dirlik	8.6592e-05	1.0394e+11
	Lalanne	9.4809e-05	9.4928e+10
	Narrow Band	1.2564e-04	7.1632e+10
791796	Dirlik	8.0839e-05	1.1133e+11
	Lalanne	8.8506e-05	1.0169e+11
	Narrow Band	1.1733e-04	7.6709e+10

7.3. Numerical Code Verification

In this chapter, results obtained from Matlab code and Ncode results including sub-steps are compared to verify the developed numerical code.

In Figure 7.14, calculated stress PSDs from both solvers are given. It is obvious that stress PSDs are almost equal to each other.

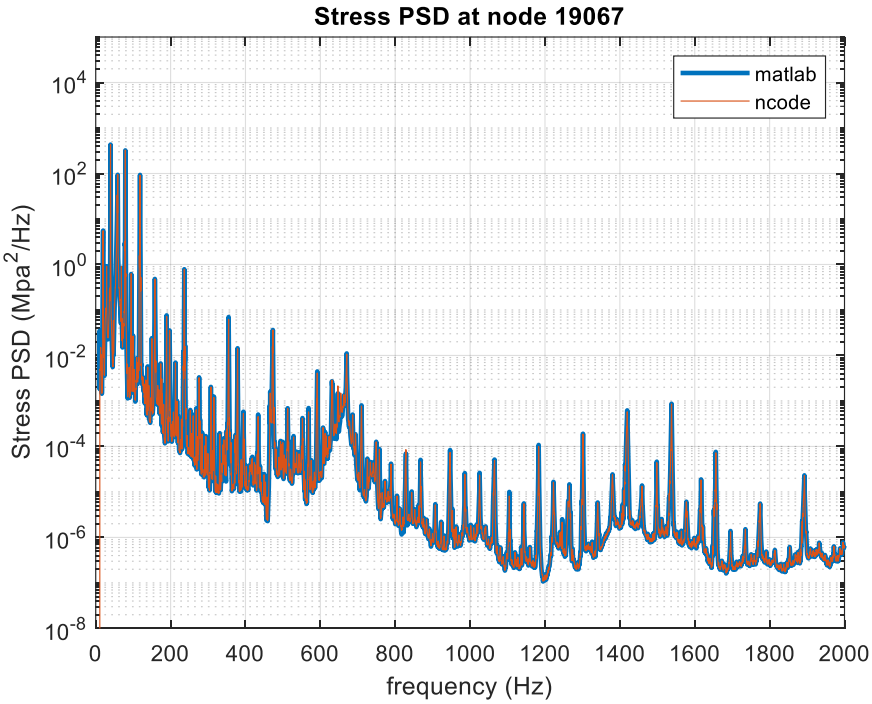

Figure 7.14 Stress PSDs at node 19067 obtained from Matlab code and Ncode

In Table 7.7, calculated spectral moments from both solvers are given. It can be seen that there is a small difference between the spectral moment values. To understand the reason behind these value differences, first of all, stress PSD functions obtained from both solvers are investigated in detail and it is concluded that the interpolation methods of input loading or transfer function may create such small effects on stress PSD functions and this may be one of the reasons of spectral moments differences.

In addition, when the stress PSD function obtained from Ncode is imported to Matlab and spectral moments are calculated from developed code, it is founded that even using exactly the same stress PSD function, spectral moments obtained from both solvers did

not give exactly the same results. So that one of the other reason for the differences in spectral moments is the spectral moment calculation method differences of both solvers.

Table 7.7 Spectral Moments comparison for node 19067

	Numerical Code	**NCode**
$\boldsymbol{m_0}$	456.7806	475.4118
$\boldsymbol{m_1}$	2.9809e+04	3.1001e+04
$\boldsymbol{m_2}$	2.3254e+06	2.3540e+06
$\boldsymbol{m_4}$	6.0392e+10	2.0320e+10

In Table 7.8, parameters of the signal obtained from relevant solvers spectral moments are given. Since there are small differences in spectral moments of both solvers, these factors are found to be different as expected.

Table 7.8 Parameters of signal comparison for node 19067

	Numerical Code	**Ncode**
$\boldsymbol{RMS}$	21.80 Mpa	21.37 Mpa
$\boldsymbol{E[0]}$	70.37	71.35
$\boldsymbol{E[P]}$	93.26	161.15
$\boldsymbol{\gamma}$	0.75	0.44

In Figure 7.15 and Figure 7.16, PDF on rainflow ranges and Damage histograms are compared. Considering these functions are all related to spectral moments, it cannot be expected to obtain exactly the same functions on both solvers. But still, Probability Density Function cycle histogram and damage histograms are quite close to each other.

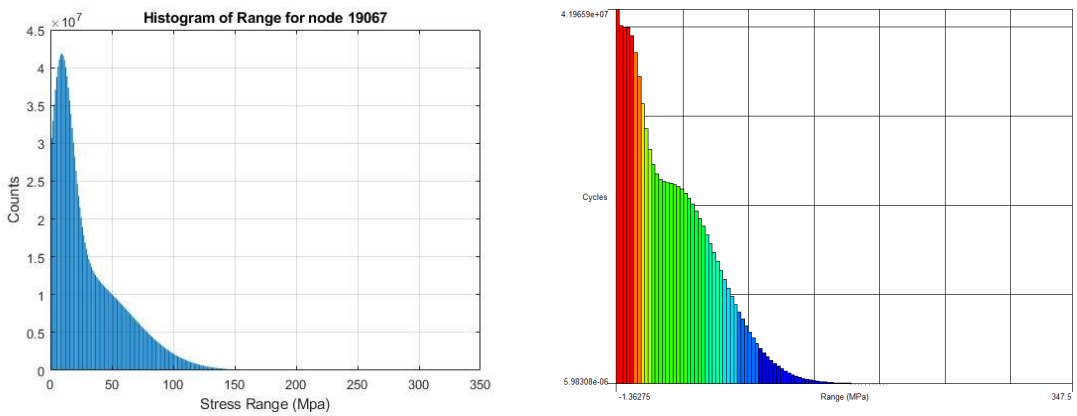

Figure 7.15 PDF obtained from Matlab code and Ncode

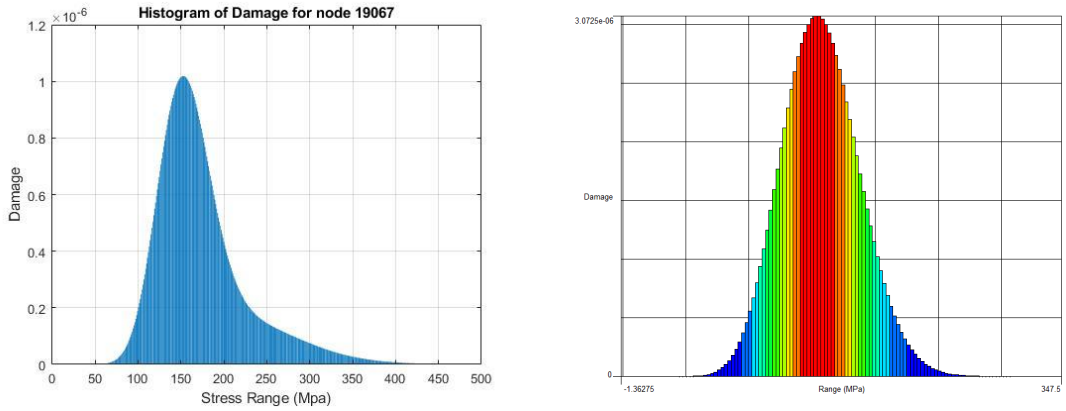

Figure 7.16 Damage Histograms obtained from Matlab code and Ncode

In Table 7.9, life comparisons for critical nodes obtained from Matlab code and Ncode are given. Despite the small differences in spectral moments and the signal parameters obtained from spectral moments, the calculated life values are very close to each other.

Table 7.9 Life comparisons for Matlab code and Ncode at critical nodes

Node id	**PSD Cycle Counting Method**	**Matlab Life(s)**	**Ncode Life (s)**
19067	Dirlik	9.9112e+10	1.0394e+11
	Lalanne	1.1610e+11	9.4928e+10
	Narrow Band	5.2112e+10	7.1632e+10
791796	Dirlik	1.0937e+11	1.1133e+11
	Lalanne	1.2535e+11	1.0169e+11
	Narrow Band	5.8369e+11	7.6709e+10

To be able to clarify the reason for the small differences between the two solvers given in Table 7.9, another analysis is performed in Matlab code. Spectral moments obtained from Ncode are entered into numerical code and results are controlled. As it is given in Table 7.10, when the spectral moments would be the same in both solvers, results are almost equal to each other. It can be concluded that the operations performed after the spectral moments in Matlab code is exactly the same as Ncode.

Table 7.10 Life comparisons when spectral moments are taken from Ncode

Node id	PSD Cycle Counting Method	Matlab Life(s)	Ncode Life (s)
19067	Dirlik	1.0390e+11	1.0394e+11
	Lalanne	9.4928e+10	9.4928e+10
	Narrow Band	7.1632e+10	7.1632e+10
791796	Dirlik	1.0959e+11	1.1133e+11
	Lalanne	1.0116e+11	1.0169e+11
	Narrow Band	7.6797e+10	7.6709e+10

When the results obtained from both solvers are examined, it can be concluded that the developed numerical code gives sufficiently accurate results and it can be used to find the fatigue life of any structure.

When the life values given in Table 7.9 examined, it is found that the life of the structure is approximately 1e+11 seconds or in other words 27.7e+06 hours. It is evaluated that the structure will not be damaged during its whole service life, which was accepted as 2500 hours.

7.4. Accelerating Life Testing of Brackets

In the previous chapters, the fatigue life of structure according to 2500 hours duration flight data is found with numerical code and Ncode. In this chapter, the aim is to find the fatigue life of the structure by using the accelerated life testing concepts and verify the results with experiments. Since the numerical code is verified in the previous chapter, life results will be given according to numerical code.

7.4.1. Accelerated Life Testing for Real Flight Data

As it is suggested in the military standard [51], 2500 hours duration data is accelerated to 4 hours and the profile is obtained as given in Figure 6.3. First of all, it is logical to find the fatigue life of 4 hours data in numerical code so that the expected failure duration is known before the experiments.

In Table 7.11, expected failure durations for 4 hours accelerated data is shown. It is clearly observed that when the 2500 hours flight data accelerated to 4 hours, failure would not be expected until at least 44102 hours according to Dirlik's method.

Table 7.11 The fatigue life of brackets for 4 hours accelerated flight data

Node id	PSD Cycle Counting Method	Life (s)	Life (h)
19067	Dirlik	1.5877e+08	4.4102e+04
	Lalanne	1.7442e+08	4.8449e+04
	Narrow Band	7.8308e+07	2.1752e+04
791796	Dirlik	1.7368e+08	4.8243e+04
	Lalanne	1.8808e+08	5.2244e+04
	Narrow Band	8.7597e+07	2.4333e+04

In such loading, accelerated fatigue testing for 4 hours can be performed just to say the structure will not fail for the whole lifetime, but it is not possible to observe crack due to long expected failure durations. In order to take reasonable failure durations, 2500 hours flight data has to be accelerated to 3.6 seconds so that the failure will be expected in 11 hours, which does not make sense. For this reason, accelerated life testing has not been performed for real flight data.

7.4.2. Scaled Flight Data and Accelerated Life Testing

As it is stated in the previous chapter, observing crack and measuring its initiation duration is not possible for accelerated flight data. Because of that, flight data is first scaled and then accelerated to 4 hours in order to observe the crack in reasonable durations. While accelerating the scaled flight data, the m factor is set according to the Dirlik method's damage value of the critical node at the end of the total duration of 2500 hours and 4 hours.

As it is stated in 5.1 Experimental Modal Analysis, damping of the system does not remain constant with increasing loading amplitude. Besides, it is not possible to obtain the damping of the system experimentally in accelerated profile since the hitting effect

causes instantaneous acceleration peaks, which are out of the measuring range of accelerometers. Consequently, accelerometers are unable to measure any data in such a profile.

That is why the finite element model is reconstructed where each case has different damping ratios as given in Table 7.12. Transfer functions obtained for each model are imported to numerical code so that for each model that has different damping ratios, fatigue life could be achieved.

The main aim is to scale and accelerate the data so that the failure would be expected in approximately 3-4 hours. If the scaling and accelerating the data is performed according to the model that has the measured damping ratios in the FEM verification experiments as given in the first line of Table 7.12, the expected failure duration of the node 19067 is found to be 4.33 hours according to Dirlik's method. However, if the system shows greater damping in that loading for instance 5% damping, failure would be expected in 147.25 hours and it is not possible to test the system for such long durations.

Table 7.12 Accelerated data according to verified model - Dirlik method

Node id	**Input loading**	**Damping ratio**	**RMS stress (Mpa)**	**Damage at 4 hours**	**Life (h)**
19067	21.48 gRMS scaled and accelerated data	ζ_1=0.012 ζ_2=0.018 ζ_3=0.007 ζ_{others}=0.02	94.9860	0.9243	4.33
		ζ_{all}=0.02	79.4186	0.2027	19.73
		ζ_{all}=0.03	70.9318	0.0750	53.33
		ζ_{all}=0.04	66.2748	0.0408	98.03
		ζ_{all}=0.05	63.3662	0.0272	147.25

In order to overcome such a problem, scaling and accelerating the data is performed with respect to the model that has 5% damping ratio and the expected failure duration is found to be 190 minutes according to Dirlik's method for node 19067 as given in Table 7.13. If the system will show less damping in the accelerated life testing experiments, failure will definitely occur within 190 minutes according to the code.

At this stage, one important parameter needs to be checked carefully. Since the accelerating procedures are performed according to the 5% damping model, obtained accelerated profile become much destructive and RMS stress levels must be checked to see whether the stress levels are getting too close to the yield strength.

Table 7.13 Accelerated data according to 5% damping model – Dirlik method

Node id	Input loading	Damping ratio	RMS stress (Mpa)	Damage at 4 hours	Life (m)
19067	30.93 gRMS scaled and accelerated data	ζ_1=0.012 ζ_2=0.018 ζ_3=0.007 ζ_{others}=0.02	145.76	13.237	18
		ζ_{all}=0.02	121.92	5.5460	43
		ζ_{all}=0.03	109.42	2.7985	86
		ζ_{all}=0.04	102.53	1.7587	136
		ζ_{all}=0.05	98.14	1.2616	190
791796	30.93 gRMS scaled and accelerated data	ζ_1=0.012 ζ_2=0.018 ζ_3=0.007 ζ_{others}=0.02	144.85	12.8541	19
		ζ_{all}=0.02	121.17	5.3438	45
		ζ_{all}=0.03	108.76	2.6818	89
		ζ_{all}=0.04	101.92	1.6806	143
		ζ_{all}=0.05	97.56	1.2036	199

According to the data given in Table 7.13, accelerated life testing is performed and eventually, in 48 minutes crack is observed exactly on one of the previously defined critical locations of the structure, node id 791796. Although the node id 19067 is expected to fail first according to the finite element model of the structure, stress levels, damages and life of both critical nodes are very close to each other. Therefore it is not surprising that node 791796 failed first.

Figure 7.17 Observed crack in 48 minutes

As it is known, in the verified finite element model, the damping ratios were obtained from experimental data and they were measured as 0.012, 0.018 and 0.007 for the first three modes respectively and all other remaining modes were accepted to have a 0.02 damping ratio. Based on the verified finite element model, the structure was expected to fail within 18-19 minutes. However, the structure failed in 48 minutes due to the non-linear behavior of damping.

It can be seen from Table 7.13, when the damping ratio is 2%, the expected failure duration according to the developed numerical code is 45 minutes and if the damping ratio is 3%, the expected failure duration is 89 minutes for node id 791796. Most probably, the system's damping behavior under accelerated loading is around 2% - 3%.

In Table 7.14, the calculated damage and life values for both critical nodes using 2% and 3% damping models for different cycle counting methods are given.

Table 7.14 Fatigue life according to different damping ratios and different counting methods

Node id	Input loading	Damping ratio	Rms stress (Mpa)	Counting Method	Damage at 4 hours	Life (m)
19067	30.93 gRMS scaled and accelerated data	ζ_{all}=0.02	121.92	Dirlik	5.5460	43.27
				Lalanne	6.2927	38.14
				N. Band	17.2177	13.94
		ζ_{all}=0.03	109.42	Dirlik	2.7985	85.76
				Lalanne	3.0878	77.72
				N. Band	8.3634	28.69
791796	30.93 gRMS scaled and accelerated data	ζ_{all}=0.02	121.17	Dirlik	5.3438	44.91
				Lalanne	5.9750	40.17
				N. Band	16.0210	14.98
		ζ_{all}=0.03	108.76	Dirlik	2.6818	89.49
				Lalanne	2.9343	81.79
				N. Band	7.8814	30.45

According to the numerical code, the calculated irregularity factor of the stress PSD function is 0.3544. As it is stated before, the irregularity factor gives information on whether the signal is a narrowband or a wideband signal. Since the irregularity factor is not close to 1, the signal is not in narrowband characteristic. That is why while comparing the PSD cycle counting methods, it can be concluded that the narrowband counting method gives definitely conservative life values. When the Dirlik and Lalanne results are compared, both methods give very close results relatively. Nevertheless, the life of the structure obtained from Lalanne's method gives slightly less values than Dirlik's method.

Considering that fatigue life is extremely dependent on a number of factors and many of these factors cannot be fully predicted, it is evaluated that the fatigue life values obtained through the accelerated life testing are close enough to confirm the life values obtained from the developed numerical code.

8. CASE STUDIES

In this chapter, case studies have been performed to examine the behavior of fatigue and the factors affecting fatigue life.

8.1. Case 1: Effect of m Exponent on Accelerated Data's Life Results

In accelerated life testing, the main desire is to obtain a shorter profile in duration that has the same effect on structure as the original long duration data. In this case study, effect of m exponent on accelerated data is investigated.

Two different profiles, where the second one is much severe in terms of creating stresses are accelerated to 4 hours with m = 7.5 as suggested in MIL-STD-810G for random loadings and then the same procedure is performed with the proposed m exponents according to the damage values obtained from numerical code. Obtained damages at the end of 4 hours for both profiles are given in Table 8.1 and Table 8.2.

Table 8.1 Accelerating the low profile data with different m constants

Flight duration	m	**Input gRMS**	**RMS stress (Mpa)**	**Damage**
2500 hours	-	3.96	21.3724	9.08e-05
4 hours	7.5	9.35	50.4241	0.002
4 hours	11.3	7.01	37.7813	9.07e-05

Table 8.2 Accelerating the high profile data with different m constants

Flight duration	m	**Input gRMS**	**RMS stress (Mpa)**	**Damage**
2500 hours	-	10.83	47.89	0.9241
4 hours	7.5	25.55	112.98	3.4235
4 hours	9.4	21.48	97.98	0.9243

In both analyzes, when the accelerated profile is obtained using the value of $m = 7.5$ as recommended in the military standard, it is seen that the damage values created by the 2500-hour data and the 4-hour data are not the same. However, if m values obtained by using the developed numerical code are used, it is seen that the damage values created by the accelerated and non-accelerated data are the same.

It is clear from Table 8.1 and Table 8.2 that the accelerated profile obtained by using the recommended $m = 7.5$ value in the military standard will give more conservative results in terms of fatigue life.

It is obvious that when the severity of the profile is changing, m exponent changes as well. The main reason is the change in stress levels in the cycles. As it is stated in the MIL-STD-810G, the m exponent is strongly influenced by the slope of the S-N curve. In the analysis, the used aluminum material's (Aluminum 7075-T6) S-N curve is not actually a linear plot but multilinear. When the stress of the system changes, while calculating the damage with Miner's theorem, used S-N curve regions are also changes. That is why the m exponent is mainly dependent on the stress levels of the system and correspondingly the S-N curve of the material.

8.2. Case 2: Effect of Shaker's PSD Data Application Range on Fatigue Life

One of the important effects of accelerated fatigue life testing is the shaker's data application range. When the desired profile is imported to the shaker, it creates 3 dB upper and lower alarm limits and 6 dB upper and lower abort limits. While applying the desired profile, the shaker's controller tries to fit the data in these ranges and apply the control signal to the system. In this case study, the effect of these upper and lower limits on the fatigue life of the structure is investigated.

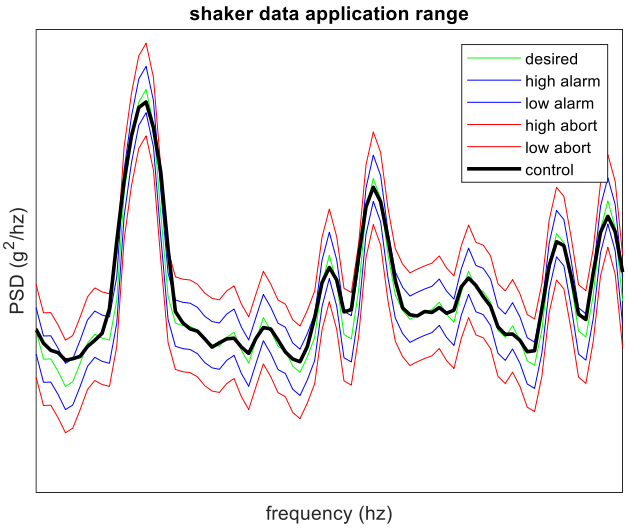

Figure 8.1 Shaker's data application range

Table 8.3 Effects of shaker's data application range in damage and life

Loading	gRMS	RMS Stress (Mpa)	Damage	Life (h)
High abort	63.24	186.53	34.139	0.117
High alarm	44.76	132.05	10.026	0.398
Low alarm	22.44	66.18	0.0412	97.08
Low abort	15.88	46.85	0.0013	3076
Desired	31.69	93.48	0.928	4.310
Control	30.93	98.14	1.261	3.170

According to Figure 8.1, there could be a wide range of amplitude variation in the signal that is very effective on the life of the structure. Even the control signal, which is the closest signal to the desired signal that the shaker can apply, has a different effect on the structure in the meaning of fatigue life.

It is important to notice that even the gRMS value of desired data is larger than the control data, the failure duration of the desired data is 35.9% longer than the control data. Such a case may occur if the fitted control signal has larger bandwidth or higher amplitudes around the natural frequencies or the control signal may have higher amplitudes at some specific frequencies than the desired signal because it is obvious that up to high abort, the data is still acceptable.

8.3. Case 3: Damage Contribution of Different Frequency Intervals

In this case study, input loading is scaled and accelerated so that the failure will exactly be expected at the end of 4 hours flight duration. The focus is to investigate the damage contribution of different frequency intervals.

Table 8.4 shows that in the 0-150 Hz range, 82% of the life of the structure is consumed. Especially in the range of 70-100 Hz and 100-150 Hz, there are high amplitude peaks on the input load. Also in the range of 0-150 Hz, amplitudes are much greater than the rest in the transfer function.

In the input load, there is no significant excitation near the first natural frequency 57.3 Hz, so that the contribution of 50-70 Hz is not really destructive. In addition, around the second and third natural frequencies, (174.9 Hz and 465.9 Hz) contribution on damage is very small in the regions 150-200 Hz and 400-500 Hz respectively.

Table 8.4 Effect of different frequency ranges on damage

Frequency interval (Hz)	**Accumulated damage**
0-50	0.0021
0-70	0.0274
0-100	0.3499
0-150	0.8157
0-200	0.8234
0-300	0.8434
0-400	0.8496
0-500	0.8567
0-1000	0.8749
0-2000	1.0000

The experiments and analyzes for the verification of the finite element model described in Chapter 5 were carried out in the range of 0-500 Hz. In doing so, the main motivation was that the main modes of the brackets analyzed remained within this range. The damage values obtained as a result of this case study also show that the frequency range of 0-500 Hz determined during the verification phase has been a reasonable approach.

8.4. Case 4: Life Difference Between Two Very Close Points

In this case study, the life of two very close nodal points is compared. As it is given in Figure 8.2, node id 19067 which is one of the critical nodes and node id 26121, which is just 0.42 mm close to the node 19067 is chosen for comparison study. Loading is defined to be 2500 hours of operational flight data just as the same loading given in Chapter 6.

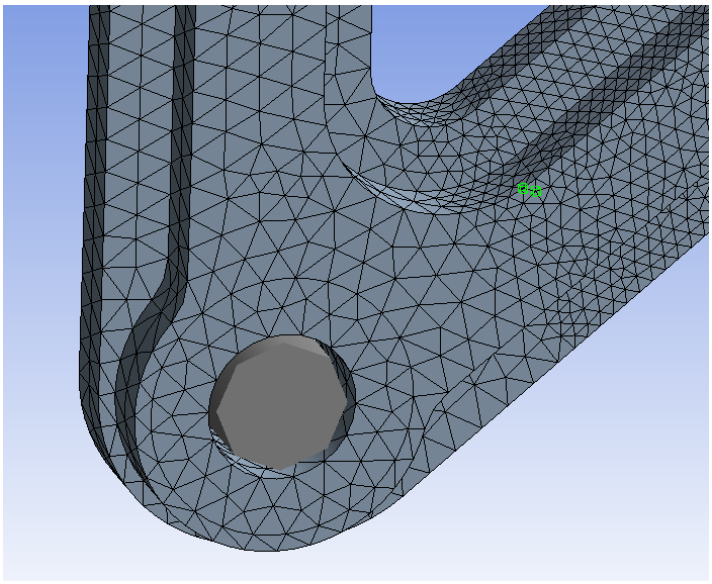

Figure 8.2 Node id 19067 (left side) and node id 26121(right side)

In Table 8.5, life and damage results of two points and in Table 8.6, comparing results with respect to change of life and RMS stress values are given.

Table 8.5 Life and damage results of two very close nodes

Node id	**RMS Stress (Mpa)**	**PSD Cycle Counting Method**	**Damage**	**Life (s)**
19067	21.37	Dirlik	9.0807e-05	9.9112e+10
		Lalanne	7.7519e-05	1.1610e+11
		Narrow Band	1.7271e-04	5.2112e+10
26121	19.46	Dirlik	3.0661e-05	2.9353e+11
		Lalanne	2.6652e-05	3.3769e+11
		Narrow Band	5.9153e-05	1.5215e+11

Table 8.6 The effect of change in RMS stress on life

Change in RMS Stress	**PSD Cycle Counting Method**	**Change in Life**
9.81%	Dirlik	33.76%
	Lalanne	34.38%
	Narrow Band	34.25%

When the analysis results are examined, it is obvious that even with two very close nodal points with 0.42 mm in between, there could be around 30% - 35% life differences. There are two very important outcomes of this case study. Firstly, fatigue analysis is heavily dependent on stress levels. Even 10 percent of stress change may result in 35 percent of life reduction. Secondly, if the analysis method is chosen to be a frequency-based fatigue approach, it should be ensured that the finite element model accurately reflects the real structure, since the stress history in this method is created by the finite element model.

9. RESULTS AND CONCLUSION

The fatigue concept is vital in the design stage of mechanical parts and must be carefully analyzed. In this thesis, vibration-based fatigue analysis of a mechanical system integrated into an unmanned aerial vehicle is examined in the frequency domain. Within this scope, a numerical code that can calculate the fatigue life is developed in Matlab and it is verified with a commercial fatigue software. An operational flight test has been performed to get the real flight loadings and Power Spectral Density functions of flight data are obtained to use in fatigue calculations. Lastly, according to the accelerated life testing concept, flight data is accelerated and the structure is tested in laboratory conditions.

In fatigue calculations, one of the most important parameters is to get the stress history correctly. In the frequency domain method, since the stress information is obtained from the finite element model of the structure, it is very important that the finite element model is a true representation of the real structure. According to one of the case studies conducted in this thesis, a 10 percent stress difference may result in 35 percent life reduction. Therefore, several analyses performed in finite element environment and experiments. By comparing these analyses finite element model is verified.

Since the modes of the analyzed brackets remained within the first 500 Hz, the finite element model has been verified for the first 500 Hz range. Furthermore, in one of the case studies, it was seen that 85 percent of the lifetime of the structure was consumed in the first 500 Hz. So, the verification frequency range approach seems reasonable.

One of the problems encountered during the construction of the finite element model was the appearance of singularity point which could mislead the detection of the failure location and consequently mislead the life of the structure. But after mesh convergence analysis, singularity points are handled correctly and the true critical locations are obtained.

During the verification experiments, another problem faced was the hitting of interior parts each other that creates unwanted peaks on the frequency response functions.

However, after more detailed experiments, it is concluded that the hitting effect has no influence at the critical location of the structure.

One of the biggest problems was the damping ratio non-linearity of the structure. When the amplitude of loading is increased, damping of the system increased as well. This is a big problem because fatigue is strongly dependent on damping. In the verification phase of the numerical code, the measured damping ratios are used. However, at the verifying numerical code with accelerated life tests, models with different damping ratios are constructed and results are tried to be reached in this way.

In order to represent the real flight conditions in the analysis, flight data is obtained with an operational flight test. The flight data is collected according to the maneuvers performed by the aircraft in an ordinary flight scenario and it is converted into PSD functions and synthesized as a single flight data for use in the analysis. An enveloping method is used to obtain a single axis PSD input and it is applied to the weakest direction of the structure.

After obtaining the input loading and the verified finite element model, fatigue calculations are performed in Matlab by using developed code and in Ncode Design Life software. Results are found very close to each other. When the small differences on both solvers are investigated, it is founded that there are two main reasons. Firstly, the difference in the interpolation methods applied to the input loading and the transfer function which are used to obtain the stress PSD function may cause small differences in the stress PSD. Considering the fatigue life is overly dependent on the stress information, even these small difference in stress PSD may have such an effect on life. The second and main reason is the spectral moments' calculation method differences of both solvers. When the stress PSD function obtained from Ncode is imported to Matlab and the spectral moments are calculated from developed code, it is founded that the spectral moments are slightly different than Ncode results. However, if the spectral moments' values of Ncode are entered into the numerical code, the life of the structure found from the numerical code is equal with Ncode results. That means calculations after the spectral moments' stage is exactly equal on both solvers. Although the life results are not exactly the same as Ncode, it can be concluded that numerical code gives sufficiently accurate results and it can be used to find the fatigue life of any structure. According to the verified numerical

code, the life of the structure was found to be 27 million hours. Considering that the whole service life of the structure is assumed to be 2500 hours, it is concluded that there will be no fatigue damage to the structure during its whole flight life.

After the verification of the numerical code, the next step is to find the fatigue life on experimental conditions. Firstly, original flight data is accelerated to 4 hours test duration and life is founded from numerical code according to the model with measured damping. It is founded that the failure would not be expected at least in 44102 hours in such loading. That is why it is decided not to perform an accelerated life testing with this loading profile.

In order to observe the crack and measure its duration in accelerated life testing, obtained flight data is first scaled and then accelerated to 4 hours. As mentioned before, it was observed that the damping of the system is changing under different loading conditions. That is why it is intended to obtain the damping characteristics of the system under scaled and accelerated flight data experimentally so that the finite element model could be constructed according to obtained damping ratios. However, since the instantaneous acceleration levels could reach values that are out of the measurement range of the accelerometers due to the impact effect of interior parts, the measurement could not be taken under high profile data. So, the finite element model is reconstructed with different gradually increasing damping ratios separately and the transfer functions are obtained for each case. Firstly, flight data scaled and accelerated according to the model with measured damping ratios so that the failure would be expected around 4 hours. However, it is founded that if the system shows greater damping such as 5 percent, the expected failure duration is found to be 147 hours. That is why it is decided to scale and accelerate the data according to the model that has 5 percent damping ratio and the expected failure duration is found to be 190 minutes. If the system shows less damping in the tests, failure would definitely occur within 190 minutes. While accelerating the data, RMS stress levels are checked to see if the stress levels are close to Yield Strength.

Eventually accelerated life testing performed and the crack is observed in 48 minutes on one of the previously defined critical nodes of the structure. However, based on the finite element model that is constructed with the measured damping ratios from experiments, the structure was expected to fail within 18-19 minutes. But it is known that the system's damping behavior is non-linear under high amplitude excitations. According to the

numerical code's results from Dirlik's method, failure would be expected in 43 minutes for the 2% damping model and 86 minutes for the 3% damping model. Most probably, the systems damping ratio is in between these values. According to accelerated life testing results, both Dirlik and Lalanne methods give very close results. If the Dirlik and Lalanne methods are compared, it is founded that Lalanne's method gives slightly less life values. Since the data is in wideband characteristics, Narrow Band method gives conservative results.

Besides the importance of getting true stress history and obtaining true damping characteristics of the structure, there are many other factors that are effective on the fatigue life of the structure. One of the important parameters is the presence of mean stress. In the time domain-based calculations, outputs of the cycle counting algorithm consist of stress range, mean stress and number of cycles information. That is why in time domain analysis it is easy to implement the mean stress effect on fatigue life. However, in the frequency domain analysis, outputs of cycle counting algorithms contain only the stress range and number of cycles information. That is why the mean stress effects in frequency-based fatigue analysis were not considered in this study.

There are some other parameters that are very effective on the accelerated life testing concept. One of them is the m factor which is used to obtain the accelerated profile. Since the main desire of accelerated life testing is to create a profile that is shorter in duration but has the same damage potential, damage values of accelerated and non-accelerated profiles expected to be the same at the end of each data durations. That is why in this thesis, rather than take m=7.5 as suggested from MIL-STD-810G, m is calculated according to the numerical code. Another important parameter of accelerated life testing is the data application range of the shaker infrastructure. Even the desired profile is imported to the shaker, it can not exactly apply this profile to the structure. That is why it needs to be considered carefully. Also, this study shows that even a profile with a lower gRMS level can give more damage so it is wrong to compare the fatigue life by comparing the gRMS levels of two profiles.

Considering the uncertainties in the model and the many factors that may affect the fatigue life explained above, the results obtained within the scope of this study considered to be satisfactory.

REFERENCES

[1] W.A.J. Albert, Uber Treibseile am Harz. Archiv fur Mineralogie, Georgnosie, Bergbau und Huttenkunde, 10, **1837**, 215.

[2] Wikipedia, Fatigue (material), https://en.wikipedia.org/wiki/Fatigue_(material), Last accesed on, **08/05/2021.**

[3] W.J.M. Rankine, On the causes of the unexpected breakage of the journals of railway axles, and on the means of preventing such accidents by observing the law of continuity in their construction., **1842**, pp. 105-108.

[4] F. Braithwaite, ON THE FATIGUE AND CONSEQUENT FRACTURE OF METALS, Minutes of the Proceedings of the Institution of Civil Engineers, Thomas Telford-ICE Virtual Library, **1854**, pp. 463-467.

[5] W. Schütz, A history of fatigue, Engineering fracture mechanics, 54, **1996**, 263-300.

[6] J. Goodman, Mechanics Applied To Engineering, Longmans, Green and Co. John, London, **1899**.

[7] J.A. Ewing, J. Humfrey, The Fracture of Metals under Repeated Alternations of Stress, Proceedings of the Royal Society of London Series I, 71, **1902**, 79.

[8] O. Basquin, The exponential law of endurance tests, Proc Am Soc Test Mater, **1910**, pp. 625-630.

[9] W.D. Douglas, Methods employed at the Royal Aircraft Establishment for the experimental determination of the ultimate strength of aeroplane structures, Advis. Comm. Aero. Rep. Memo., 476, **1918**.

[10] H. Gough, The Fatigue of Metals, Scott, Greenwood and Son, London, **1924**.

[11] A. Palmgren, Die lebensdauer von kugellargern, Zeitshrift des Vereines Duetsher Ingenieure, 68, **1924**, 339.

[12] M. Miner, Cumulative fatigue damage, Journal of applied mechanics, 12, **1945**, A159-A164.

[13] L.F. Coffin Jr, A study of the effects of cyclic thermal stresses on a ductile metal, Transactions of the American Society of Mechanical Engineers, New York, 76, **1954**, 931-950.

[14] L. Coffin, The problem of thermal stress fatigue in austenitic steels at elevated temperatures, Symposium on Effect of Cyclic Heating and Stressing on Metals at Elevated Temperatures, ASTM International, **1954**.

[15] G. Irwin, Fracture in “Handbuch der Physik,” vol. V, Springer-Verlag Berlin, Göttingen, Heidelberg, **1958**.

[16] P. Paris, The growth of cracks due to variations in load: Ph. D. Thesis. Lehigh University, **1962**.

[17] M. Matsuishi, T.J.J.S.o.M.E. Endo, Fukuoka, Japan, Fatigue of metals subjected to varying stress, 68, **1968**, 37-40.

[18] W. Elber, The significance of fatigue crack closure, Damage tolerance in aircraft structures, ASTM International, **1971**,

[19] M.W. Brown, K. Miller, A theory for fatigue failure under multiaxial stress-strain conditions, Proceedings of the Institution of Mechanical engineers, 187, **1973**, 745-755.

[20] R. Smith, The versailles railway accident of 1842 and the first research into metal fatigue.(retroactive coverage), Fatigue 90, **1990**, 2033-2041.

[21] Siemens Simcenter, History of Fatigue, https://community.sw.siemens.com/s/article/history-of-fatigue, Last accesed on, **08/05/2021.**

[22] S.O. Rice, Mathematical analysis of random noise. Selected papers on noise and stochastic processes, Dover, New York, **1954**, 133-294.

[23] J.S. Bendat, Probability functions for random responses: prediction of peaks, fatigue damage, and catastrophic failures, **1964**.

[24] J. Tunna, Fatigue life prediction for Gaussian random loads at the design stage, Fatigue & Fracture of Engineering Materials & Structures, 9, **1986**, 169-184.

[25] P.H. Wirsching, M.C. Light, Fatigue under wide band random stresses, Journal of the Structural Division, 106, **1980**, 1593-1607.

[26] G. Chaudhury, W. Dover, Fatigue analysis of offshore platforms subject to sea wave loadings, International Journal of Fatigue, 7, **1985**, 13-19.

[27] D.S. Steinberg, Vibration analysis for electronic equipment, **2000**.

[28] T. Dirlik, Application of computers in fatigue analysis, **1985**.

[29] N.W. Bishop, F. Sherratt, Finite element based fatigue calculations, NAFEMS, **2000**.

[30] N. Bishop, A.J.U.R.L. Woodward, UK: MSC Software, Fatigue Analysis of a Missile Shaker Table Mounting Bracket, **2000**.

[31] M. Aykan, Vibration fatigue analysis of equipments used in aerospace, **2005**.

[32] Y. Eldoğan, Vibration fatigue analysis of structures installed on air platforms, **2012**.

[33] G.İ. DEMİREL, Vibration Fatigue Analysis and Testing of Notched Beams, **2019**.

[34] G. Teixeira, Random Vibration Fatigue - A Study Comparing Time Domain and Frequency Domain Approaches for Automotive Applications, SAE Technical Papers, 1, **2014**.

[35] A. Halfpenny, F. Kihm, Rainflow cycle counting and acoustic fatigue analysis techniques for random loading, 10th RASD, Citeseer, **2010**.

[36] Fatigue Life LLC, Fatigue Life Prediction, https://fatigue-life.com/fatigue-physics/, Last accesed on, **08/05/2021.**

[37] G.E. Dieter, D.J. Bacon, Mechanical metallurgy, McGraw-hill New York, **1986**.

[38] J.E. Shigley, Shigley's mechanical engineering design, Tata McGraw-Hill Education, **2011**.

[39] M.A. Meyers, K.K. Chawla, Mechanical behavior of materials, Cambridge university press, **2008**.

[40] C. Lalanne, Mechanical vibration and shock analysis, fatigue damage, John Wiley & Sons, **2010**.

[41] T.J.C. Irvine, Rainflow cycle counting in fatigue analysis, **2011**.

[42] A. Halfpenny, A frequency domain approach for fatigue life estimation, China Mechanical Engineering (中国机械工程), **1998**, 11.

[43] HBM Ncode, Design Life Theory Guide, NC-DL-TH 9.00.092.

[44] MSC Software, Multiaxial Fatigue Theory, http://web.mscsoftware.com/training_videos/patran/Reverb_help/index.html#page/Fatigue%2520Users%2520Guide/fat_mulitaxial.07.5.html#ww78444, Last accesed on, **08/05/2021.**

[45] Ncode, 10 Common Mistakes in Fatigue Analysis, https://www.ncode.com/videos/10-common-mistakes-in-fatigue-analysis-2020, Last accesed on, **08/05/2021.**

[46] S.R. Singiresu, Mechanical vibrations, Addison Wesley Boston, MA, **1995**.

[47] P. Avitabile, Modal testing: a practitioner's guide, John Wiley & Sons, **2017**.

[48] C. Lalanne, Mechanical vibration & shock, Wiley Online Library, **2002**.

[49] G.R. Henderson, A.G. Piersol, Fatigue damage related descriptor for random vibration test environments, Sound and Vibration, 29, **1995**, 20-25.

[50] J. Jang, J.-W. Park, Simplified Vibration PSD Synthesis Method for MIL-STD-810, Applied Sciences, 10, **2020**, 458.

[51] M.K.J.U.D.o.D.W. Thompson, DC, USA, MIL-STD-810G environmental engineering considerations and laboratory tests, **2008**.

[52] M. HDBK, 5J Metallic Materials and Elements for Aerospace Vehicle Structures, Department of Defense Handbook, 31, **2003**.

APPENDICES

APPENDIX A

Damping Ratio Estimation

In this thesis, damping ratios are measured from the Half-Power Bandwidth method. In this method, damping is related to the frequency differences obtained at half power points and the natural frequency of the system. Half power points can be found by multiplying the peak amplitude with 0.707, which is approximately equal to the -3 dB decrease of the peak amplitude in the logarithmic scale.

$$10 \cdot \log_{10}\left(\frac{1}{2}\right) = 20 \cdot \log_{10}\left(\frac{1}{\sqrt{2}}\right) \approx -3.0103\ dB \tag{A.1}$$

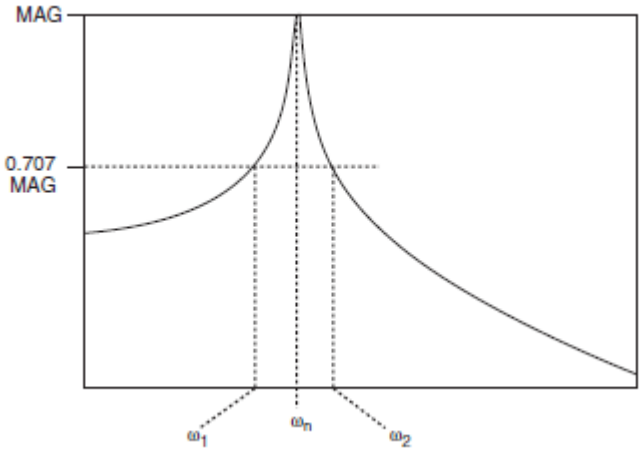

Figure A.1 Half Power Bandwidth method [47]

And the damping ratio of each natural frequency location can be obtained with equation(A.2).

$$\zeta = \frac{\omega_2 - \omega_1}{2 \cdot \omega_n} \tag{A.2}$$

APPENDIX B

Material Properties of Aluminum 6061-T6 and 7075-T6

Table B.1 Material Properties of Aluminum 6061-T6

Density	2.70 g/cc
Elastic Modulus	68.9 Gpa
Poisson Ratio	0.33
Fatigue Strength	96.5 Mpa
Ultimate Tensile Strength	310 Mpa
Yield Strength	276 Mpa

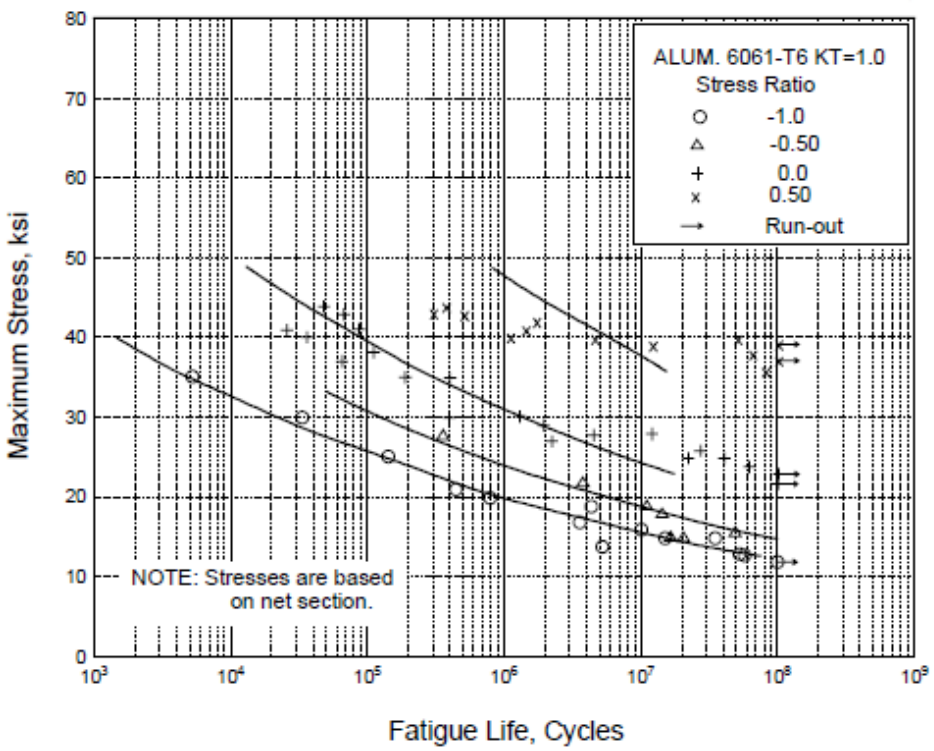

Figure B.1 Best fit S/N curve for unnotched 6061-T6 aluminum alloy [52]

Table B.2 Material Properties of Aluminum 7075-T6

Density	2.81 g/cc
Elastic Modulus	71.7 Gpa
Poisson Ratio	0.33
Fatigue Strength	159 Mpa
Ultimate Tensile Strength	560 Mpa
Yield Strength	480 Mpa

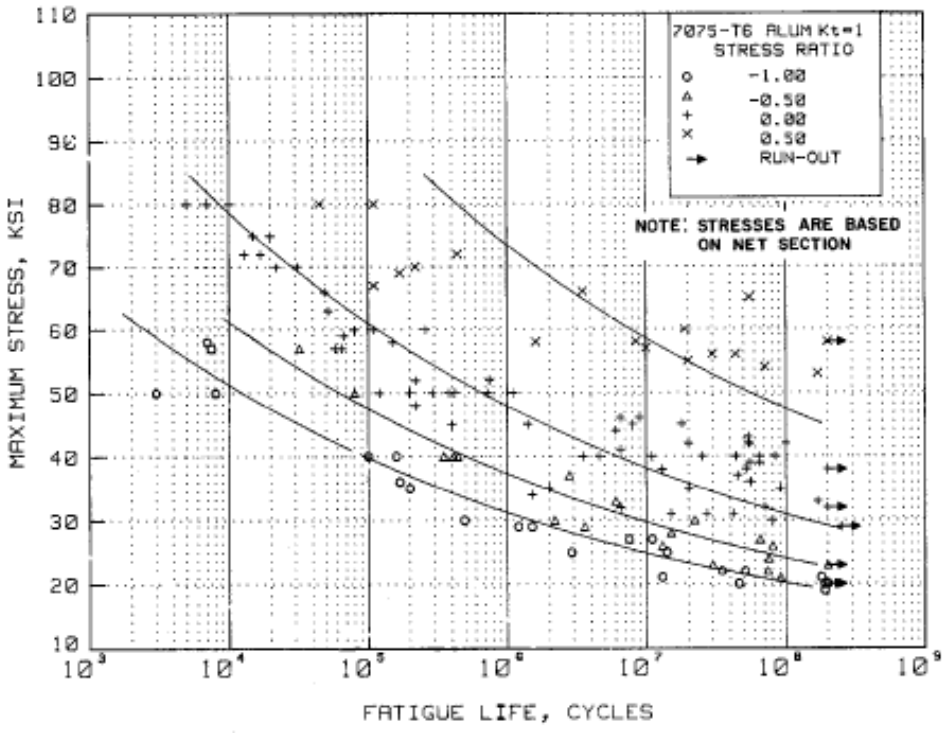

Figure B.2 Best fit S/N curve for unnotched 7075-T6 aluminum alloy [52]

.